

**NANOPARTICLE-MEDIATED FUNCTIONAL AND MOLECULAR
PHOTOACOUSTIC IMAGING FOR ASSESSMENT OF
METASTATIC LYMPH NODES**

A Dissertation
Presented to
The Academic Faculty

by

Diego Sayed Dumani Jarquin

In Partial Fulfillment
of the Requirements for the Degree
Doctor of Philosophy in the
Wallace H. Coulter Department of Biomedical Engineering

Georgia Institute of Technology
Emory University
December 2018

COPYRIGHT © 2018 BY DIEGO S. DUMANI J.

NANOPARTICLE-MEDIATED FUNCTIONAL AND MOLECULAR PHOTOACOUSTIC IMAGING FOR ASSESSMENT OF METASTATIC LYMPH NODES

Approved by:

Dr. Stanislav Emelianov, Advisor
School of Electrical and Computer
Engineering
Georgia Institute of Technology
Department of Biomedical Engineering
*Georgia Institute of Technology & Emory
University School of Medicine*

Dr. Lily Yang
Department of Surgery, and Radiology
and Imaging Sciences
Emory University School of Medicine

Dr. Brooks Lindsey
Department of Biomedical Engineering
*Georgia Institute of Technology & Emory
University School of Medicine*

Dr. Baowei Fei
Department of Bioengineering
University of Texas (UT) at Dallas
Department of Radiology
UT Southwestern Medical Center

Dr. Francisco Robles
Department of Biomedical Engineering
*Georgia Institute of Technology & Emory
University School of Medicine*

Date Approved: November 2, 2018

To my family.

ACKNOWLEDGEMENTS

I owe my PhD to the help of so many people that this page might not be enough to express all my gratitude. First, I would like to thank Stas for being an exceptional advisor. I was privileged of not having to worry about futile details during graduate school and I had the right amount of freedom to think and pursue crazy research ideas, always with a counterbalance to make sure my conclusions were solid. I will never regret moving to Georgia with the lab. I would also like to thank my committee members: Dr. Lindsey, Dr. Robles, Dr. Yang, and Dr. Fei for their help and valuable feedback. I could not forget to thank my undergraduate mentors Dr. Lochi Yu and Dr. Javier Jo, for motivating me many years ago and helping me prepare to be where I am today. I wish to thank every single member of the Ultrasound Imaging and Therapeutics Research lab: I appreciate all the help when I had no idea what I was doing, the office/hallway discussions (whether serious or not), the volleyball, lunches, free swag, and the overall support – I could not have done this without you all. I wish to thank the staff at Georgia Tech: Katrine, BME, PRL, CEED, Student Center, for always helping me with a smile. To all my friends: thanks for encouraging me and for helping me take a break from long work hours. Last, but certainly not least, I want to thank my family: mamá, papá, Pablo, Mariangela, tío Armando y familia, for their immense support throughout these years, whether I was in Costa Rica, Texas, or Atlanta. You are my inspiration. Thank you!

TABLE OF CONTENTS

ACKNOWLEDGEMENTS	iv
LIST OF TABLES	viii
LIST OF FIGURES	ix
LIST OF SYMBOLS AND ABBREVIATIONS	xiv
SUMMARY	xv
CHAPTER 1. Introduction	1
1.1 Hallmarks of cancer	1
1.2 Detection of lymph node metastasis	2
1.2.1 Alternative strategies for sentinel lymph node biopsy	3
1.3 Ultrasound and photoacoustic imaging	3
1.4 Photoacoustic applications in oncology	5
1.4.1 Hemoglobin and imaging of blood oxygenation	6
1.4.2 Targeted contrast agent visualization	7
1.4.3 Protease sensitive contrast agents	9
1.4.4 Kinetic-based methods	9
1.4.5 Circulating tumor cells	10
1.5 Additional functional and morphological changes in metastatic lymph nodes	11
1.6 Summary of research goals	12
CHAPTER 2. Detection of lymph node metastasis by photoacoustic imaging of immune cell uptake and transport dynamics	15
2.1 Role of glycol-chitosan-coated gold nanoparticles	15
2.2 Role of immune cells	16
2.3 Materials and methods	18
2.3.1 Synthesis of gold nanoparticles	18
2.3.2 Ultrasound and photoacoustic imaging	19
2.3.3 Animal model	20
2.3.4 Imaging protocol	20
2.3.5 Histological analysis	20
2.3.6 Image analysis	21
2.3.7 Statistical analysis	21
2.4 Results and discussion	21
2.5 Conclusion	29
CHAPTER 3. Molecular photoacoustic imaging of lymph node metastasis using clearable gold nanoparticles	30
3.1 Materials and Methods	31
3.1.1 Gold nanoparticles	31

3.1.2	Animal model	31
3.1.3	Bioluminescence	31
3.1.4	Ultrasound and photoacoustic imaging	32
3.1.5	Multiwavelength spectroscopic analysis	32
3.2	Results and discussion	33
3.3	Conclusion	38
CHAPTER 4. Enhanced sensitivity with a dual mode nanosensor for molecular imaging		39
4.1	Materials and methods	41
4.1.1	Photoacoustic/Fluorescence imaging setup	41
4.1.2	Phantom imaging	42
4.1.3	In vivo imaging	42
4.2	Results and discussion	43
4.3	Conclusions	47
CHAPTER 5. A gold-silica janus nanosensor to enhance diagnostic and therapeutic potential		48
5.1	Janus nanoparticle design	49
5.2	Materials and methods	50
5.2.1	Nanoparticle characterizations	51
5.2.2	Synthesis of citrate-stabilized AuNPs	51
5.2.3	Synthesis of GSJNP and GSCSNP	52
5.2.4	Photoacoustic imaging with PTFE tube phantoms	52
5.2.5	Preparation of GSJNP-Loaded Cells	53
5.2.6	Photoacoustic imaging with tissue-mimicking gelatin phantom	53
5.2.7	Characterization of cytotoxicity of GSJNP	54
5.2.8	Ultrasound and photoacoustic imaging in vivo	55
5.2.9	Multiwavelength spectroscopic analysis	55
5.3	Results and discussion	56
5.4	Conclusions	66
CHAPTER 6. Prussian Blue nanocubes – towards full-body multifunctionality		68
6.1	Materials and Methods	70
6.1.1	Synthesis of SPION precursors	70
6.1.2	Synthesis of PBNCS	71
6.1.3	Transmission electron microscopy	72
6.1.4	SQUID Magnetometry	73
6.1.5	MRI relaxometry	73
6.1.6	Photostability	74
6.1.7	Cell labeling	75
6.1.8	Cell phantom preparation and US/PA imaging	76
6.1.9	Ultrasound and photoacoustic imaging	76
6.1.10	Magnetic resonance imaging	76
6.1.11	In vivo animal procedures	77
6.1.12	Magnetic Delivery and US/PA imaging	77
6.2	Size control	78

6.3	Magnetic and optical properties	81
6.4	Magnetic resonance imaging	83
6.5	Photoacoustic imaging	85
6.6	In vivo imaging	89
6.7	Additional applications in oncology: Image-guided magnetic trapping	93
6.8	Discussion	94
6.9	Conclusions	96
CHAPTER 7.	Conclusions and future work	97
7.1	Summary	97
7.2	Future studies with developed contrast agents	99
7.3	A theranostic paradigm: towards image-guided therapy and outcome monitoring	101
7.4	Conclusion	103
REFERENCES		104

LIST OF TABLES

Table 1 – Longitudinal and transverse molar relaxivity of PBNCs.....	85
--	----

LIST OF FIGURES

Figure 1 – Photoacoustic imaging of lymph node metastasis based on oxygen saturation. (A) Schematic drawing depicts the location of the primary tumor, cervical lymph nodes, and imaging volume. (B) Representative two-dimensional US image shows the cervical lymph nodes (arrows). (C) Coregistered PA image. (D) Ten single-wavelength PA images were acquired in each imaging plane. (E) A linear least-squares spectral unmixing algorithm was used to calculate the spectroscopic PA image depicting the oxygen saturation. Scale bars are 2 mm. Reproduced from⁴³ 7

Figure 2 – PA visualization of lymph node metastasis using targeted AuNPs. Raw PA images of NP accumulation at 680 nm and 860 nm (A and B, respectively). PA spectral changes over time (C-E). Colors correspond to AuNPs (yellow) or blood (red, blue) as marked on A and B. Absorption spectrum of AuNPs changes after aggregation. An overall increase in signal from gold nanoparticles (yellow) shows the accumulation kinetics (F). Adapted from²⁴ 8

Figure 3 – Immunofunctional imaging paradigm. (a) The mouse is injected peritumorally with GC-AuNP contrast agent. (b) The contrast agent becomes NIR-absorbing upon uptake by immune cells and is transported to the sentinel lymph node via afferent lymphatic vessels. (c) The GC-AuNP-loaded cell accumulation in the lymph node provides information about presence of metastasis. 18

Figure 4 – Ultrasound/Photoacoustic images of a non-metastatic sentinel lymph node (a) before and (b) 24 hours after injection of GC-AuNP. (c) After 24 hours, the photoacoustic signal spectrum shows a 10-fold increase in absorption at 700 nm..... 22

Figure 5 – Two-dimensional US/PA immunofunctional imaging. (a, d) B-mode ultrasound was used to localize the lymph nodes. (b, e) Overlaid photoacoustic imaging shows GC-AuNP-loaded cells in the lymph node and afferent lymphatic vessel. (c, f) Ultrasound-masked photoacoustic images show the effect of metastasis in nanoparticle-loaded-cell accumulation. 23

Figure 6 – 3D-rendered US/PA images of the sentinel lymph node 24 hours after injection in (a) naïve mouse, (b) tumor bearing mouse without metastasis, (c) tumor bearing mouse with metastasis. (d) The bar graph shows an over 2-fold decrease in the percent lymph node volume occupied by nanoparticle-loaded cells. Data are shown as means \pm SD (n = 4). **p = 0.002 ; ***p = 0.001 24

Figure 7 – Ultrasound/Photoacoustic images of a healthy sentinel lymph node in a naïve mouse (a) before and (b) 24 hours after injection of PEG-AuNPs. (c) After 24 hours, there are no significant changes in the the photoacoustic signal spectrum..... 25

Figure 8 – Histological analysis shows (a) GC-AuNPs using dark-field microscopy and (b) cancer cells using GFP fluorescence. (c, d) The merged images show that GC-AuNPs and cancer cells do not spatially coincide. Scale bars are (c) 150 μm , and (d) 300 μm	26
Figure 9 – Bioluminescence image of lymph node metastasis prior (left) and after (right) tongue tumor removal.	34
Figure 10 – Ultrasound-based skin segmentation images. A mask (left) was created by detecting the edge of the skin and assuming a 400 μm thickness. Only the blue area is preserved. The mask is overlaid (right) with the b-mode ultrasound to show the rejected skin area.	35
Figure 11 – Ultrasound and spectroscopic photoacoustic image of a murine neck axial cross section showing the cervical lymph nodes (whited dashed contours). The colormaps show oxygenated hemoglobin (blue), deoxygenated hemoglobin (red), and aggregated gold nanoparticles (yellow). Metastasis is indicated by localized aggregation of gold nanoparticles (white arrow).	36
Figure 12 – (a) Schematic of PAttrace shows an ICG J-aggregate encapsulated by a phospholipid and cholesterol shell. (b) Absorption spectra of intact and digested PAttrace. Before interaction, a sharp peak at 890 nm is obtained. After interaction with cells or environment, free ICG absorption spectrum is recovered.	41
Figure 13 – (a) Schematic of PAFT phantom design. On the left is the phantom, on the right is a horizontal slice view. (b) Fluorescence image showing tubes 1, 2, and 3, using 780 nm excitation. Tubes 4, 5, and support rods are not visible. (c) Horizontal slice view of PA at 890 nm. (d) Horizontal slice view of PA at 780 nm. The tubes' positions are matched in (a), (c), and (d) horizontal slices	44
Figure 14 – Schematic of mouse restrainer and its position in PAFT system.	44
Figure 15 – Photoacoustic (PA) 2D projection and fluorescence images of a mouse (dorsal view) using 780 nm laser excitation	45
Figure 16 – US/PA images 24 hours after injection. The dashed white lines indicate the location of (a) the lymph node and (b) subcutaneous injection site. (c) The graph shows the spectral shift due to digestion of the liposomes.	46
Figure 17 – TEM images of gold-silica janus nanoparticles and gold-silica core-shell nanoparticles	56
Figure 18 – TEM image of GSJNPs and EDS characterization corresponding to the two spots at (a) gold nanoparticle and (b) silica shell on holey carbon film coated copper grids.	57
Figure 19 – (a) UV-Vis absorption spectra of citrated AuNP (black line), GSCSNP (blue line), GSJNP (red line) in DI water (solid lines) and in DMEM with 10% FBS (dotted lines). (b) Hydrodynamic sizes of citrated AuNP, GSCSNP, GSJNP in DI water, and	

GSJNP in DMEM with 10% FBS. (c) TEM micrograph of GSJNP in DMEM with 10% FBS.	58
Figure 20 – DLS size distribution curves of citrate-stabilized AuNP, GSJNP, and GSCSNP in DMEM with 10% FBS.	58
Figure 21 – Stability of GSJNP aggregates in DMEM characterized using (a) UV-Vis and (b) DLS.	60
Figure 22 – Photoacoustic signal measurement using PTFE tubes for GSJNP and GSCSNP in DMEM with 10% FBS. (a) Combined PA images with ultrasound images (left) and averaged PA intensity at 700 nm of excitation (right). (b) Multiwavelength PA signal measurements of GSJNP (red line) and GSCSNP (gray line).	61
Figure 23 – Ultrasound and photoacoustic images (scale bar = 2 mm) of gelatin inclusions containing (a) macrophages and (b) human breast cancer cells incubated with GSJNPs. 63	
Figure 24 – Stability of PA signal for GSJNP in macrophages under laser irradiation....	63
Figure 25 – Multiwavelength PA signal measurements of gelatin inclusions containing (a) macrophages and (b) human breast cancer cells incubated with GSJNPs.....	64
Figure 26 – Cytotoxicity analysis of GSJNPs with HEK 293T cells by MTT assay (y axis: relative % viability calculated by comparing cells treated with GSJNPs with untreated cells, x axis: final OD of GSJNPs at 532 nm).	64
Figure 27 – Combined ultrasound and photoacoustic in vivo images ($\lambda = 700$ nm, scale bar = 2 mm) of mice injected with GSJNP or GSCSNP (left and right column, respectively) at (a) mammary fat pad subcutaneous injection site (yellow arrow) and (b) draining inguinal lymph node (white dashed line). (c) Multiwavelength PA imaging enables spectral unmixing of oxygenated hemoglobin (HbO ₂), deoxygenated hemoglobin (Hb), and nanoparticles (AuNP). (d) Multiwavelength PA spectra in the lymph node of each mouse, injected with GSJNP (red line) and GSCSNP (black line).	66
Figure 28 – TEM images of size-controlled PBNCs. (a) 20-nm PBNCs synthesized from 3 nm SPION precursors. (b) 40-nm PBNCs synthesized from 5-nm SPION precursors. (c) 150-nm PBNCs synthesized from 10-nm SPION precursors. (d-f) Images at increased magnification for 20-nm, 40-nm, and 150-nm PBNCs, respectively. (g) Scatter plot showing relationship between SPION precursors and resulting PBNC size.	79
Figure 29 – Analysis of particle size distribution. (a-c) Size distribution of SPIONs with expected diameters of approximately 3 nm, 5 nm, and 10 nm, respectively. (d-f) Size distribution of resulting PBNCs with expected width of approximately 20 nm, 40 nm, and 150 nm, respectively.	79
Figure 30 – Analysis of particle size coefficient of variation. A wider size distribution of SPION precursors causes higher deviation in the resulting PBNCs.	80

Figure 31 – Energy-dispersive X-ray spectroscopy of a PBNCs shows homogenous distribution of elements across the nanocube.	81
Figure 32 – Magnetic and optical properties of PBNCs. (a) Magnetic moment curves show a 5-fold increase in magnetization for PBNCs compared to Fe ₃ O ₄ based on nanoparticle mass. (b) UV-Vis spectrometry shows PBNCs’ NIR absorbance peak at 680 nm.....	83
Figure 33 – Relaxometry studies to measure (a) T ₁ relaxation and (b) T ₂ relaxation of PBNCs at 0.25 mg/ml. Relaxivity plots with respect to different iron concentrations were used to calculate (c) longitudinal and (d) transverse relaxations.	84
Figure 34 – PA signal during laser irradiation at 26 mJ/cm ² shows stable signal generation of PBNCs. Progressive degradation after repeated laser pulses was seen for PEG-AuNR and SiO ₂ -AuNR	86
Figure 35 – Photothermal stability and photoacoustic imaging of PBNCs. (a) Photoacoustic signal from PBNCs, PEGylated gold nanorods (PEG-AuNR) and silica-coated gold nanorods (SiO ₂ -AuNR) at different fluences. PBNCs remained stable and conserve linearity with fluence when exposed to 900 laser pulses beyond 25 mJ·cm ⁻² . AuNR showed degradation beyond 5 mJ·cm ⁻² (b) The absorbance spectrum of PBNCs remained stable after 900 laser pulses up to 20 mJ·cm ⁻² . (c) Gold nanorods’ spectra showed degradation for all energies between 4 and 20 mJ·cm ⁻² . (d) Ultrasound (US, gray scale) and photoacoustic (PA, color map) imaging of 20-nm PBNCs in (i) DIUF, (ii) cell culture media, (iii) PBNC-labeled cancer cells, and (iv) PBNC-labeled mesenchymal stem cells. (e) Photoacoustic spectrum of cancer cells labeled with 20-nm PBNCs.....	88
Figure 36 – (a) Photoacoustic images of axial cross section of a mouse abdomen at 700 nm following subcutaneous injection of PBNC in Matrigel (blue contour) and PBS in Matrigel (orange contour). (b) Corresponding normalized absorption spectra on each injection bolus.	89
Figure 37 – In vivo MRI imaging of axial cross section of a mouse abdomen injected with 50% matrigel mixed with PBS (Blank) or Prussian blue nanocubes (PBNC) as indicated by the white arrows. A Flash sequence was used with TR = 500 ms and TE of (a) 3.3 ms, (b) 10 ms, and (c) 15 ms.	90
Figure 38 – Photoacoustic images of axial cross section at 700 nm, 24 hours after subcutaneous injections of 200-nm PBNCs. (a) Metastatic sentinel lymph node does not show significant accumulation of PBNCs while (b) the lymph node on the opposite healthy side shows high PBNC signal. (c) Normalized spectra confirm the predominant photoabsorbers are blood for the metastatic lymph node, and PBNC for the healthy lymph node.....	91
Figure 39 –MRI of coronal cross section of a tumor-bearing mouse 24 hours after subcutaneous injections of 200-nm PBNCs. The metastatic lymph node (orange contour) shows a brighter intensity than the healthy inguinal node (blue contour). A Flash sequence was used with TR = 400 ms, TE 3.9 ms, and flip angle of 30°.	92

Figure 40 – Image-guided magnetic trapping of cells labeled with 20-nm PBNCs. (a) PBNC-labeled cells can be manipulated using an external magnet, as opposed to the AuNP-labeled cells (control). (b) Insert: ultrasound (gray scale) and photoacoustic (color scale) image of capillary tube with PBNC-labeled cells trapped at the bar magnet, indicated by the dashed line. The integrated PA signal along the tube length shows a 5-fold PA signal increase at the gradient magnet position. 94

Figure 41 – Comparison of silica nanoparticles vs ICG-loaded silica nanoparticles. 100

LIST OF SYMBOLS AND ABBREVIATIONS

SLN	Sentinel lymph node
US/PA	Ultrasound and photoacoustic imaging
PA	Photoacoustic imaging
NIR	Near-infrared
NPs	Nanoparticles
AuNPs	Gold nanoparticles
GC-AuNPs	Glycol-chitosan-coated gold nanoparticles
PEG-AuNPs	PEGylated gold nanoparticles
ICG	Indocyanine green
EGFR	Epidermal growth factor receptor
EPR	Enhanced permeability and retention
CTC	Circulating tumor cell
HbO ₂	Oxygenated hemoglobin
Hb	Deoxygenated hemoglobin
PAFT	Photoacoustic and fluorescence tomography
OD	Optical density
GSJNPs	Gold-silica Janus nanoparticles
GSCSNPs	Gold-silica core-shell nanoparticles
TEM	Transmission electron microscopy
EDXS	Energy-dispersive X-ray spectroscopy
PBNCs	Prussian blue nanocubes
SPIONs	Superparamagnetic iron oxide nanoparticles

SUMMARY

Despite advances in prevention, detection, and treatment of cancer, this disease remains the second leading cause of death in the United States. The majority of cancer related deaths are due to metastasis rather than primary tumors and, although mortality rates have decreased over the last two decades, efforts to achieve comprehensive diagnoses and effective treatments still encounter obstacles due to lack of non-invasive technologies that accurately assess cancer. The goal of this project is to design a non-invasive approach for the assessment of sentinel lymph node metastasis using ultrasound and photoacoustic imaging, augmented with contrast agents. The focus is two-fold: first, contrast-enhanced ultrasound and photoacoustic imaging are evaluated as a tool to track functional and molecular changes of metastatic lymph nodes in relevant in vivo cancer models. Specifically, imaging of immune cell uptake and transport of lymphotropic nanoparticles to the sentinel lymph node, and imaging of clearable nanoparticles targeted to the epidermal growth factor receptor provide diagnostic information regarding metastatic nodal involvement. Second, alternative contrast agents are designed with the goal of solving challenges of the proposed techniques and augmenting therapeutic capabilities. Overall, the study is expected to help identify cancer based on functional and molecular changes, therefore augmenting and potentially replacing sentinel lymph node biopsy.

CHAPTER 1. INTRODUCTION

Despite advances in prevention, detection, and treatment of cancer, this disease remains the second leading cause of death in the United States and is expected to take over 600,000 American lives this year. In women, breast cancer is the most common type and second deadliest after lung cancer. In the U.S., 1 in 8 women will develop invasive breast cancer in their lifetime. Over 250,000 new cases and more than 40,000 deaths are expected in 2018¹. In men, prostate cancer is the most common, and second deadliest after lung cancer. The majority of cancer related deaths are due to metastasis rather than primary tumors. Although mortality rates have decreased over the last two decades, efforts to achieve comprehensive diagnoses and effective treatments encounter obstacles due to lack of technology or excessive morbidity.

1.1 Hallmarks of cancer

Humans can develop diverse kinds of cancerous tumors with varying molecular and morphological characteristics. Despite the complexity inherent to each type of tumor, there are common hallmarks that have been described by Hanahan and Weinberg². Namely, the hallmarks of cancer are the following:

- Sustaining Proliferative Signaling
- Evading growth suppressors
- Resisting cell death
- Enabling replicative immortality
- Inducing angiogenesis

- Activating invasion and metastasis

The present work will concentrate on the last of these hallmarks: activated invasion and metastasis. Metastasis is the culmination of cancer and occurs when primary tumor cells successfully invade other locations of the body after hematogenous and/or lymphatic spread. Given that the majority of cancer deaths are caused by metastatic spread, it is critical to detect these lesions as soon as possible to design an appropriate treatment strategy. By improving early detection and treatment of metastasis, cancer survival rates can increase. Additionally, doing so with minimal morbidity would improve quality of life of cancer patients.

Because many tumors initially spread through the lymphatic way, the present work will focus on tools to aid in early detection of lymph node metastasis.

1.2 Detection of lymph node metastasis

Many tumors spread initially via lymphatic vessels, invading lymph nodes near the primary tumor. The current clinical practice to assess lymph node metastasis is to biopsy and examine tumor-neighboring lymph nodes for presence of metastasis, particularly the first one to which the tumor drains, known as the sentinel lymph node (SLN). If no cancer cells are found in the sentinel lymph node, it is likely that the remaining lymph nodes are also uninvaded³. Thus, sentinel lymph nodes are key in cancer staging, prognosis, and treatment design. During a SLN biopsy procedure, locating the sentinel node is a challenge in itself and requires the use of typically radioactive contrast agents⁴⁻⁷. Upon localization of the radiotracer, the SLN is removed for examination by a pathologist. Unfortunately,

this procedure involves morbidity due to removal of the node and pathologists are prone to miss small micrometastases, with false-negative rates as high as 60%⁸⁻⁹.

1.2.1 Alternative strategies for sentinel lymph node biopsy

Non-invasive imaging techniques can synergize with contrast agents to overcome some of the hurdles inherent to SLN biopsy by providing enhanced diagnostic information and treatment guidance with decreased morbidity. Several studies have investigated the use of conventional imaging modalities, such as MRI, CT, PET, and ultrasound for assessment of metastatic lymph nodes¹⁰⁻¹³. However, there are challenges that prevent those approaches from being realistic alternatives to SLN biopsy. For instance, MRI, CT, and PET are time consuming and costly techniques that are not compatible with the current clinical paradigm. Moreover, they do not offer improvements in specificity and sensitivity that would justify the elevated costs. While conventional ultrasound has not provided enough sensitivity or specificity either, it is of interest because of its high versatility and low cost.

1.3 Ultrasound and photoacoustic imaging

Ultrasound and photoacoustic (US/PA) imaging have emerged as promising tools to visualize tumor characteristics in a non-invasive, cost-effective way. These synergistic imaging modalities allow anatomical, functional, and molecular visualization of pathology. Ultrasound is widely used in clinic to study tissue morphology but suffers from poor contrast for other applications. US/PA synergy lies on using ultrasound's anatomical information to guide photoacoustic's functional and molecular imaging with enhanced contrast¹⁴⁻¹⁷.

Several studies have shown applications for lymphatic imaging and SLN mapping using contrast agents¹⁸⁻²³. Given the potential for functional and molecular evaluation of the lymph node, US/PA have been explored as alternatives to SLN biopsy for metastasis diagnosis, in order to reduce invasiveness and cost, while maintaining clinical accuracy²⁴⁻²⁶. However, these attempts still face challenges such as cost, low sensitivity and specificity, and potential effects of the contrast agents.

There are a variety of exogenous PA contrast agents, including optical dyes, carbon nanotubes, plasmonic nanoparticles and hybrid nanoconstructs²⁷⁻²⁸. Agents with near-infrared (NIR) absorption, between 700 and 1100 nm, are preferred because these wavelengths allow deeper light penetration in tissue²⁹. One of the most commonly used agents are plasmonic gold nanoparticles (AuNPs) due to their high absorption cross-section, biocompatibility, and ease of surface modification³⁰⁻³¹.

Despite their biocompatibility, one of the main challenges of AuNPs is the concern about long-term effects of non-cleared gold. Some of the most versatile AuNPs are bigger than 5 nm, which prevents them from undergoing renal clearance. However, efforts have been made to design smaller nanoparticles and degradable clusters, providing versatile optical absorption while enabling later renal clearance³²⁻³³. Other nanoparticles such as copper sulfide offer advantages such as biocompatibility and NIR absorption with small particle size, at the expense of lower molar absorptivity compared to gold by about two orders of magnitude³⁴⁻³⁵.

Apart from solid nanoparticles, novel hybrid agents also offer biocompatibility and faster clearance. Indocyanine green (ICG), an FDA-approved dye, can be encapsulated in

liposomes to provide higher PA signals and longer circulation times than free dye molecules³⁶.

To distinguish endogenous chromophores (e.g., blood) and exogenous contrast agents, multiwavelength PA data is usually required. Indeed, using distinct spectral features of endogenous absorbers (oxygenated and deoxygenated blood) and exogenous contrast agents, the presence of absorbers and their relative concentrations can be calculated by using various analytical or iterative signal processing methods³⁷⁻³⁸. When many absorbers are present, the mathematical fit seems to yield better results with lower mean square errors. However, presence of multiple absorbers, particularly agents that are not spectrally distinct, may actually decrease the estimation accuracy of the spectral matching algorithms, while increasing the computational cost³⁷⁻³⁹. Because of this, contrast agents with high molar absorptivity and distinct spectral features are ideal because they can allow for single-wavelength imaging or simplify multiwavelength approaches.

1.4 Photoacoustic applications in oncology¹

Tumor environments undergo a series of physiological and metabolic changes that alter local pH, oxygenation, and vascularization⁴⁰. In addition, certain cell receptors are over-expressed and can be targeted with different agents and ligands. All of these processes can be identified with different PA imaging techniques and used for diagnosis and staging.

¹ This section is partially adapted from a textbook chapter ‘Overview of Photoacoustic Imaging’ (Dana, Dumani, Cook, and Emelianov 2016). Diego Dumani is the primary author of this section.

1.4.1 Hemoglobin and imaging of blood oxygenation

Cancer cells that undergo rapid proliferation rely on vasculature to meet high oxygen and nutrient demands. This often results in abnormal vascular formation due in part to unbalanced pro- and anti-angiogenic factors⁴¹. In addition, a correlation with tumor progression and oxygen saturation has been observed, showing that hypoxia increases with tumor growth⁴².

PA imaging of hemoglobin can visualize areas of increased angiogenesis, while estimating oxygen saturation can help to identify hypoxic regions that may indicate presence of cancer. This method has been used to diagnose tumors⁴² and metastatic lesions in lymph nodes (Figure 1)⁴³, and to assess therapies by correlating changes in oxygenation as the indicator of treatment efficacy⁴⁴.

At least two different wavelengths are needed for this technique, but more can be used for increased reliability at the expense of longer imaging times and increased system complexity. Studies referenced above have used up to ten different wavelengths in the 680 nm – 860 nm range. More sophisticated algorithms can be used to optimize the wavelength selection if needed⁴⁵.

The absence of exogenous agents makes this method readily translatable. However, potential difficulties may arise with small metastatic regions that have not reached a level of hypoxia to be considered malignant, or on the contrary, when areas of a tumor in later stages become necrotic and oxygen saturation estimations do not accurately represent tissue pathology.

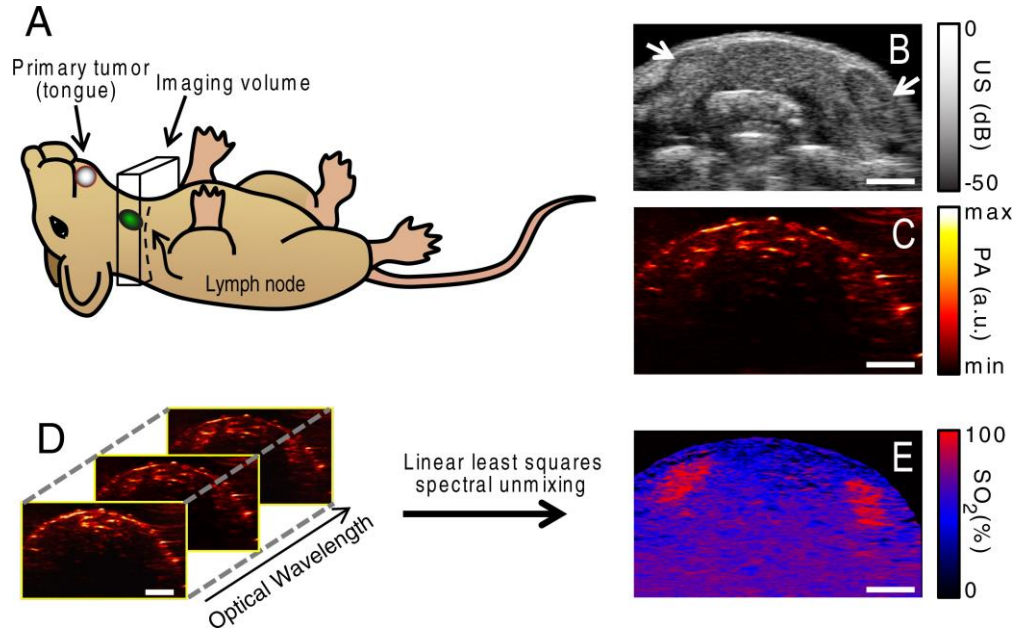


Figure 1 – Photoacoustic imaging of lymph node metastasis based on oxygen saturation. (A) Schematic drawing depicts the location of the primary tumor, cervical lymph nodes, and imaging volume. (B) Representative two-dimensional US image shows the cervical lymph nodes (arrows). (C) Coregistered PA image. (D) Ten single-wavelength PA images were acquired in each imaging plane. (E) A linear least-squares spectral unmixing algorithm was used to calculate the spectroscopic PA image depicting the oxygen saturation. Scale bars are 2 mm. Reproduced from⁴³.

1.4.2 Targeted contrast agent visualization

The demand for increasing constant nutrient supply in a rapidly-growing tumor causes the over-expression of various cell receptors that can be targeted for contrast agent and drug delivery⁴⁶. Commonly targeted cell receptors include: $\alpha_v\beta_3$ -integrin, folate receptor, vascular endothelial growth factor (VEGF) receptor, and the family of epidermal growth factor receptors (EGFR and HER2)⁴⁷.

Contrast agents are targeted to these cancer biomarkers using different surface modifications and functionalizations. Polymer coatings and proteins can be attached to contrast agents to bind to cancer-specific receptors and enhance tumor accumulation. These

coatings aim to avoid non-specific binding on normal cells and tissues⁴⁸. Nanoparticles (NPs) have been conjugated to $\alpha_v\beta_3$ -integrin antagonists to image tumor related angiogenesis⁴⁹. Anti-HER2 and anti-EGFR antibodies have also been used to deliver targeted contrast agents to the cancer cells⁵⁰. Targeted plasmonic NPs, such as gold nanospheres, can undergo receptor-mediated endocytosis, showing a spectral shift due to particle aggregation (Figure 2)^{24, 51}.

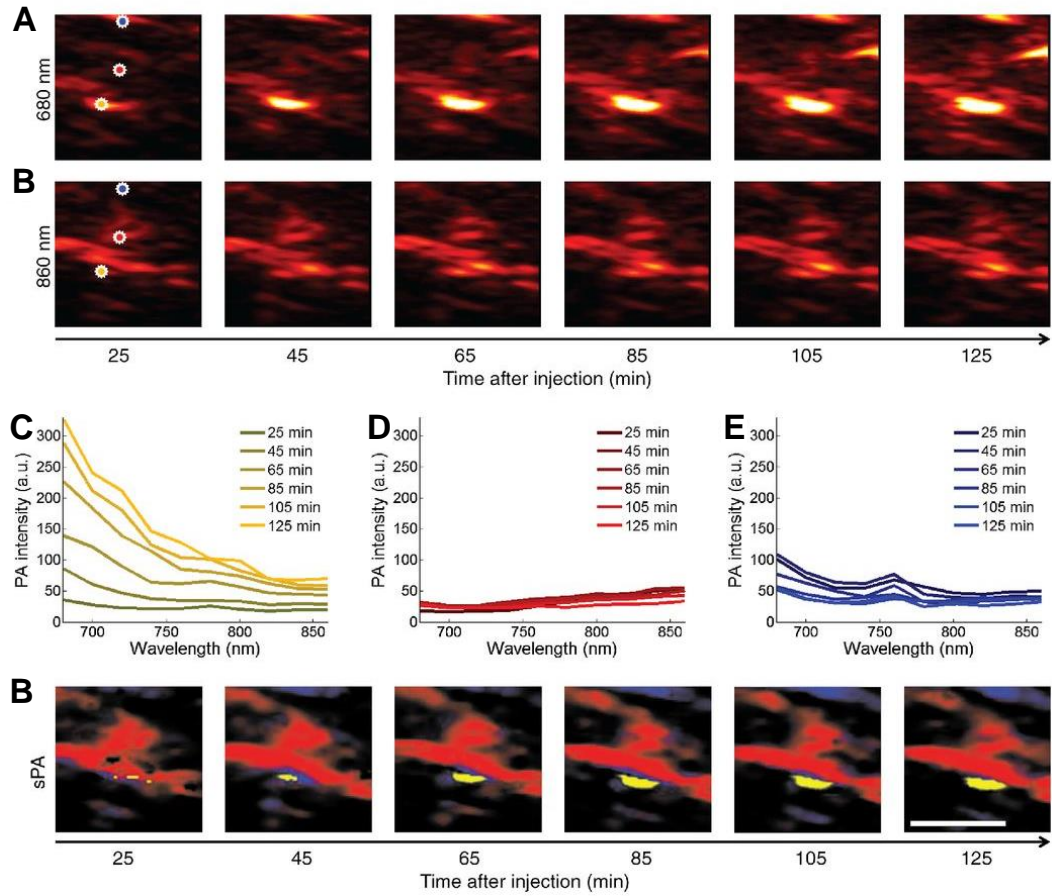


Figure 2 – PA visualization of lymph node metastasis using targeted AuNPs. Raw PA images of NP accumulation at 680 nm and 860 nm (A and B, respectively). PA spectral changes over time (C-E). Colors correspond to AuNPs (yellow) or blood (red, blue) as marked on A and B. Absorption spectrum of AuNPs changes after aggregation. An overall increase in signal from gold nanoparticles (yellow) shows the accumulation kinetics (F). Adapted from²⁴.

Challenges of this technique include finding specific ligands and antigens, as well as robust conjugation techniques to increase affinity and avoid non-specific binding. NPs can degrade in physiological media; thus these surface modifications should also be able to preserve the particles in vivo. Moreover, circulation times must be optimized to minimize uptake by the reticuloendothelial system⁵².

1.4.3 Protease sensitive contrast agents

PA imaging can be used to identify cancerous lesions through the use of activatable probes. The method involves the injection of a probe absorbing at two different wavelengths (λ_1 and λ_2), with one absorbing region targeted to cancer-related matrix metalloproteinases (MMPs) using an activatable cell-penetrating peptide (ACPP). When the probe is cleaved by MMPs, only the sensitive ACPP accumulates in the cell, resulting in single-wavelength absorption at λ_1 . An image subtraction method can then be used to visualize the cleaved (activated) probe⁵³, and has been applied to image follicular thyroid carcinoma in mice in vivo⁵⁴.

1.4.4 Kinetic-based methods

Vasculature in healthy tissue is characterized by organized, dichotomous branching. In contrast, tumor vasculature exhibits increased, but erratic vessel formation, with larger inter-endothelial junctions in vessel walls forming a porous endothelium with gaps ranging from 100 nm to 2 μ m. Consequently, leaky vasculature naturally found in solid tumors allows agents to easily extravasate^{41, 47, 55} and increases retention of these materials⁵⁶. The sum of these factors is known as Enhanced Permeability and Retention (EPR) effect and has been shown to facilitate passive accumulation of nano-sized agents⁵⁷.

Photoacoustic imaging has been used to track passively-delivered dyes and NPs to identify tumors and to monitor treatment^{30, 36, 58}. Kinetics can be useful for precise localization by identifying differences in wash-in and wash-out times^{36, 59-60}. This approach is especially convenient as it does not necessitate tumor-specific targeting moieties, although active targeting has been shown to enhance endocytosis after accumulation in the tumor by the EPR effect⁶¹.

Unfortunately, the EPR effect is heterogeneous within tumors and varies with location and time⁴¹. Short circulation times may not allow agents to successfully accumulate, requiring surface modifications to avoid premature clearance. As some tumors do not exhibit a strong EPR effect, accumulation can be further enhanced using active targeting techniques⁶¹⁻⁶². For lymph node metastasis applications, more studies are needed in order to determine effects EPR. In fact, an opposite effect may exist, as will be discussed in further sections of this document.

1.4.5 Circulating tumor cells

In addition to local invasion and lymphatic spread, the vascular system is a major conduit for cancer metastasis. The presence of circulating tumor cells (CTCs) in blood vessels can indicate the potential for metastatic disease⁶³. PA imaging has been investigated for in vivo tracking of CTCs, enabling larger blood volumes to be sampled. PA flow cytometry approaches allow detection with sensitivities of approximately 1 CTC/mL on abdominal vessels of a melanoma mouse model⁶⁴.

To reduce scanning time and allow detection of other types of cancer while keeping the same sensitivity, magnetic NPs targeted to tumor-specific receptors can be injected and

captured near vessel walls with an external magnet. This accumulation provides increased PA signal that indicates presence of CTCs⁶⁵. Additionally, magnetomotive PA techniques can be used for improved sensitivity, but are yet to be tested in vivo⁶⁶.

PA-based detection of CTCs is promising because it provides a non-invasive, real-time option with high sensitivity and penetration. However, humans possess a blood volume that is three orders of magnitude larger than in a mouse, requiring greater scan times and/or enhanced sensitivity.

1.5 Additional functional and morphological changes in metastatic lymph nodes

In order to design diagnostic techniques that can improve, or eventually replace SLN biopsy, it is important to understand the changes that lymph nodes undergo before, during, and after metastasis. Subsequently, these signs may be assessed and combined to attain highly sensitive and specific diagnoses.

As mentioned in section 1.4, US/PA imaging has been successful in identifying changes in oxygen saturation and overexpression of tumor cell receptors. However, additional morphological and functional changes could also be studied.

Prior to invasion, tumors release various growth factors to induce lymphangiogenesis. Increased intratumoral and peritumoral lymphatic density can be correlated to lymph node metastasis in certain types of cancer⁶⁷. Additionally, these factors also have effects in the draining sentinel lymph node(s). It is important to note that these changes start to appear prior to metastatic invasion, to prepare the environment for metastasis. The emergence of more lymphatic vessels is also accompanied by an increase

in lymph flow, which also plays a role in facilitating migration of metastatic cells. Once tumor cells start to appear in the sentinel lymph node, they will continue to release growth factors that prepare other lymph nodes and organs for further invasion.

In addition to an increase in lymphangiogenesis and lymph flow, pre-metastatic lymph nodes experience a remodeling of high endothelial venules and expansion of immune cell and stromal cell populations. Interestingly, there is also an immunosuppressive cytokine environment caused by cancer. SLNs become more immunocompromised with an increase in the primary tumor size⁶⁸.

Healthy lymphatics constantly deliver antigen presenting cells carrying peripherally-captured antigens, in addition to soluble antigens for uptake by node-resident dendritic cells and macrophages⁶⁹. When cancer appears, there are complex changes that modulate and alter dendritic cell maturation behavior, as a mechanism to stop immune responses against metastatic cells⁶⁸.

Overall, pre-metastatic and metastatic lymph nodes experience changes in immune cell populations, remodeling of areas occupied by these cells, and downregulation of immune function⁷⁰. Although these morphological, phenotypical and functional changes are extremely complex, their evaluation could be useful in the assessment of sentinel lymph nodes and staging of cancer patients.

1.6 Summary of research goals

The goal of my research is to design a non-invasive approach for the assessment of sentinel lymph nodes using ultrasound and photoacoustic imaging, augmented with

contrast agents. Specifically, contrast-enhanced ultrasound and photoacoustic imaging are evaluated as tools to track functional and molecular changes of metastatic lymph nodes in relevant in vivo cancer models. To solve challenges of the proposed techniques and augment theranostic capabilities, alternative contrast agents are designed and tested in vivo.

Chapter 2 focuses on detecting changes in immune cell uptake and transport of lymphotropic nanoparticles to the sentinel lymph node. Three dimensional US/PA imaging is used to quantify the volume occupied by nanoparticle signal, therefore providing information of functional and morphological disruptions correlated to metastasis.

Chapter 3 intends to further expand the characterization, introducing a molecular US/PA imaging approach. This approach uses EGFR-targeted gold nanoparticles but overcomes the concern of long-term biocompatibility by using 5-nm clearable nanoparticles.

Chapter 4 presents a contrast agent based on FDA-approved indocyanine green dye. This agent can be tracked before and after interaction with tumor environments, and improves imaging sensitivity in molecular imaging applications, particularly useful for detection of small metastatic foci. Additionally, it may be more readily translatable to clinic than other metallic nanoparticle agents.

Chapter 5 explores a hybrid contrast agent that allows dual surface modification. Such agent can be targeted to cancer cells and loaded with dyes to enhance imaging sensitivity. Additionally, it has the potential to be used as a vehicle for image-guided drug delivery upon diagnosis.

Chapter 6 focuses on a multifunctional nanoparticle that can operate as a PA/MRI contrast agent. Its optical and magnetic properties allow multimodality and could potentially be used in theranostic applications. Preliminary studies show diagnostic value for both sentinel lymph node imaging and circulating tumor cell screening.

Finally, Chapter 7 discusses the future outlook based upon the presented work, including challenges that should be addressed in subsequent studies. The next steps regarding technique improvement and contrast agent utilization, particularly in therapeutic applications, are presented.

CHAPTER 2. DETECTION OF LYMPH NODE METASTASIS BY PHOTOACOUSTIC IMAGING OF IMMUNE CELL UPTAKE AND TRANSPORT DYNAMICS

The functional and morphological changes that lymph nodes undergo during metastatic invasion, introduced in section 1.5, suggest that interactions of immune cells with foreign objects, namely nanoparticles, could be affected when metastasis is present.

To evaluate these changes, an *immunofunctional imaging* method was developed for identifying sentinel lymph node metastasis, using combined ultrasound and photoacoustic imaging augmented with glycol-chitosan-coated gold nanoparticles (GC-AuNPs). The hypothesis (Figure 3) establishes that GC-AuNPs are uptaken by immune cells upon peritumoral injection. After lymphatic transport by the immune cells, the presence of metastasis affects the spatio-temporal distribution of GC-AuNP-loaded immune cells in the SLN. This effect can be monitored via US/PA imaging and quantified to obtain a diagnostic result.

2.1 Role of glycol-chitosan-coated gold nanoparticles

Gold nanoparticles (AuNPs) are one of the most commonly used photoacoustic contrast agents due to their high molar absorptivity and capability for diverse surface modifications. The use of AuNPs entails many benefits for the *immunofunctional imaging* approach. Spherical AuNPs have a negligible near-infrared (NIR) optical absorption and are thus invisible in NIR US/PA when colloidally dispersed. However, cellular uptake-

induced aggregation results in an enhancement of the NIR absorption, allowing to visualize endocytosed nanoparticles⁷¹.

Glycol-chitosan enhances hydrophilicity, stability and biocompatibility of AuNPs⁷². GC-AuNPs have effectively been used for in vivo contrast-enhanced photoacoustic mapping of cervical lymph nodes in healthy mice, generating high-contrast images due to uptake by immune cells⁷³. Further in vitro studies showed that, within 24 hours, GC-AuNPs are preferentially uptaken by immune cells rather than cancer cells⁷³. The nanoparticle's neutral to weak-positive surface charge facilitates protein adsorption and subsequent immune cell uptake. These results enabled further validation of our method in vivo.

2.2 Role of immune cells

The optimal delivery of agents to the lymph nodes has been subject of numerous studies. This delivery can occur via passive flow and subsequent uptake by lymph node resident immune cells, or via cell trafficking after uptake at the injection site. In general, delivery efficiency can be affected by nanoparticle size, shape, and surface properties, such as charge, hydrophobicity and chemical composition⁷⁴.

To enhance this delivery, both chitosan and glycol-chitosan have been studied as vaccine adjuvants because they regulate immune response, thus promoting immune cell activation⁷⁵⁻⁷⁸. Furthermore, cationic particles are known to promote trafficking and retention in the lymph node⁷⁹⁻⁸¹. These properties of glycol-chitosan can be advantageous for lymphatic imaging.

In the present study, skin resident dendritic cells are suspected to have a role in transporting GC-AuNPs to the sentinel lymph node. Additionally, lymph node resident immune cells may also recognize and uptake passively-drained GC-AuNPs, further increasing the local photoacoustic signal. Overall, the nanoparticle-loaded cells in the lymph nodes may consist of a combination of peripheral migratory immune cells and resident immune cells.

Previous studies have used iron oxide nanoparticles (IONPs) and MRI as a method to find metastatic lymph nodes. Upon intravenous injection, healthy lymph nodes showed an increased, homogeneous presence of IONPs, after being uptaken and transported by immune cells¹⁰⁻¹¹. On the other hand, metastatic lymph nodes showed decreased, heterogeneous accumulation. However, this method carries several challenges. The intravenous administration requires a much higher dose to achieve enough agent delivery and imaging sensitivity. Additionally, this route offers no distinction between sentinel and non-sentinel nodes. This, together with negative contrast of IONPs deems this method not time-effective nor easily compatible with the current diagnostic paradigm.

Another study suggested using similar IONPs for ex vivo photoacoustic detection of metastasis⁸². However, IONPs are poor NIR absorbers thus preventing high imaging sensitivity. As such, in vivo attempts failed to detect differences between metastatic and non-metastatic groups⁸³.

In this chapter, the goal is to assess changes in immune cell uptake and distribution, due to metastasis, by using a contrast agent that is highly lymphotropic, promotes immune

cell interaction, and generates high-contrast photoacoustic images, providing highly sensitive diagnostic value.

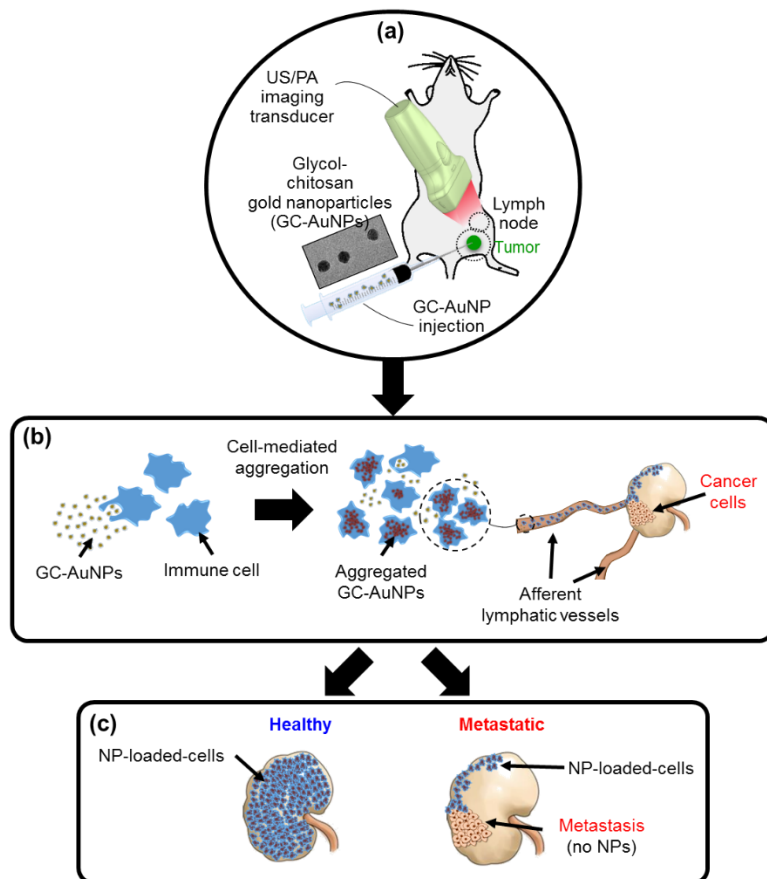


Figure 3 – Immunofunctional imaging paradigm. (a) The mouse is injected peritumorally with GC-AuNP contrast agent. (b) The contrast agent becomes NIR-absorbing upon uptake by immune cells and is transported to the sentinel lymph node via afferent lymphatic vessels. (c) The GC-AuNP-loaded cell accumulation in the lymph node provides information about presence of metastasis.

2.3 Materials and methods

2.3.1 Synthesis of gold nanoparticles

GC-AuNPs were synthesized through chloroauric acid reduction as described elsewhere⁸⁴. Briefly, 300 ml of glycol chitosan solution (1 mg/ml, Sigma-Aldrich Corp.,

St. Louis, MO) was boiled to 70°C and mixed with HAuCl₄·3H₂O solution (1 mM, 100 ml) under stirring for 24 hours until the solution turned to red. Glycol-chitosan acted as a reducing and stabilizing agent. The resulting nanoparticle size was 20 nm, with an optical absorption peak of 520 nm. Nanoparticles were washed and concentrated via centrifugation and diluted to a concentration of 0.1 mg/ml of gold.

As a control, PEG-AuNPs were synthesized by citrate reduction. Briefly, 6 ml of hydrogen trichloroaurate (III) solution (25 mM) was diluted with 279 ml of distilled water and heated to boil under stirring. Then, 15 ml of trisodium citrate solution (1 wt%) was added to produce gold nanoparticles with a diameter of approximately 20 nm. After cooling down, 5 ml of nanoparticle colloid was mixed with 5 ml of mPEG-SH solution (Laysan Bio, Inc., MW=5000, 2 mg/ml) under stirring for 24 hours. Before injection, PEG-AuNPs were washed via centrifugation and concentrated to 0.1 mg Au/ml.

2.3.2 Ultrasound and photoacoustic imaging

US/PA imaging was performed using a Vevo LAZR system (Visualsonics Inc.). Laser irradiation was delivered through a fiber optic bundle, integrated with a 40 MHz ultrasound transducer (LZ-550). The laser was tuned from 680 to 970 nm, with a 4-6 ns pulse duration and 20 Hz repetition rate. Laser fluence was kept under the American National Standard Institute (ANSI) safety limits. For 3D scans, the transducer was attached to a translational motor. The motor moved perpendicularly to the imaging plane while acquiring US/PA imaging slices. Images were post processed and analyzed using Amira (Thermo Fisher Scientific) and MATLAB (MathWorks).

2.3.3 *Animal model*

All animal procedures were approved by the Institutional Animal Care and Use Committee (IACUC) at the Georgia Institute of Technology. Five-week old female nude mice (Nu/Nu, Charles River) were inoculated in the right caudal mammary fat pad with 2×10^6 human breast adenocarcinoma cells in 50% matrigel (MDA-MB231-Red-FLuc-GFP, PerkinElmer) for the metastatic group. For the non-metastatic control group, mice were inoculated similarly with non-metastatic human ductal carcinoma cells (BT474, ATCC). Tumors were allowed to grow up to a 10 mm diameter prior to imaging studies. Naïve mice of the same strain and age were used as an additional control group.

2.3.4 *Imaging protocol*

Mice were injected with 100 μ l of GC-AuNP colloid peritumorally. US/PA imaging was performed before and immediately after injection, and 1 h, 24 h, and 48 h subsequently. Conventional B-mode ultrasound was used to identify the inguinal lymph node anatomy. Accumulation of GC-AuNP in the SLN after cellular uptake by immune cells was visualized using multiwavelength PA imaging. At the end of the imaging studies, tissue was harvested for histological analysis.

2.3.5 *Histological analysis*

The inguinal lymph nodes were resected after imaging studies and kept in 10% buffered formalin. Samples were then embedded in paraffin and sliced for H&E staining. Histology slides were visualized on a Leica DMI3000B microscope. Cancer cells were

identified by presence of GFP fluorescence, and GC-AuNP were identified using dark-field microscopy.

2.3.6 Image analysis

Three-dimensional B-mode ultrasound images were used to segment the lymph node volume of each mouse, creating a lymph node mask. Photoacoustic images were filtered using a 3D median filter followed by a 3D averaging window. A low threshold was applied to remove pixels under the noise floor. Then, adaptive thresholding⁸⁵ was performed using a moving window 1/8 the size of the image, to avoid overestimation of the threshold in cases where strong skin signals or other artifacts were present. The lymph node mask was applied to the thresholded images. The ratio of bright pixels over the total pixels in the mask corresponds to the percent volume of the lymph node occupied by nanoparticle-loaded cells.

2.3.7 Statistical analysis

A one-way analysis of variance (ANOVA) test was performed for the healthy, non-metastatic, and metastatic study groups. A post-hoc Tukey's honest significant difference (HSD) test was performed to determine the statistically significant differences among study group means.

2.4 Results and discussion

GC-AuNPs exhibited high contrast enhancement in animal studies upon cell endocytosis. Images before and 24 hours after injection demonstrate a 10-fold increase of PA signal at 700 nm in the lymph node (Figure 4). This increase enables single-wavelength

imaging of GC-AuNPs, therefore simplifying image acquisition and analysis. If much lower doses of gold were required, GC-AuNPs could still be localized using multiwavelength imaging at the expense of a more time-consuming approach.

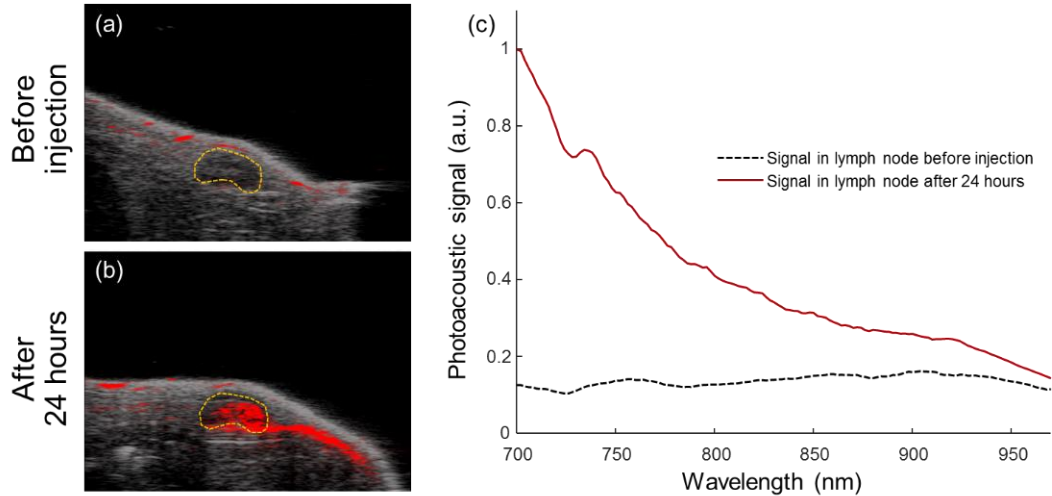


Figure 4 – Ultrasound/Photoacoustic images of a non-metastatic sentinel lymph node (a) before and (b) 24 hours after injection of GC-AuNP. (c) After 24 hours, the photoacoustic signal spectrum shows a 10-fold increase in absorption at 700 nm

When metastatic and non-metastatic study groups were compared, US/PA imaging showed that distribution of GC-AuNP-loaded cells in the SLN was disrupted due to metastasis (Figure 5). Single-wavelength 700 nm PA images effectively demonstrated this effect. No significant changes in imaging contrast were observed between 24 h and 48 h drainage. As metastases further invade the lymph node, the effect could become even more pronounced to the point where no PA contrast would be seen inside the node.

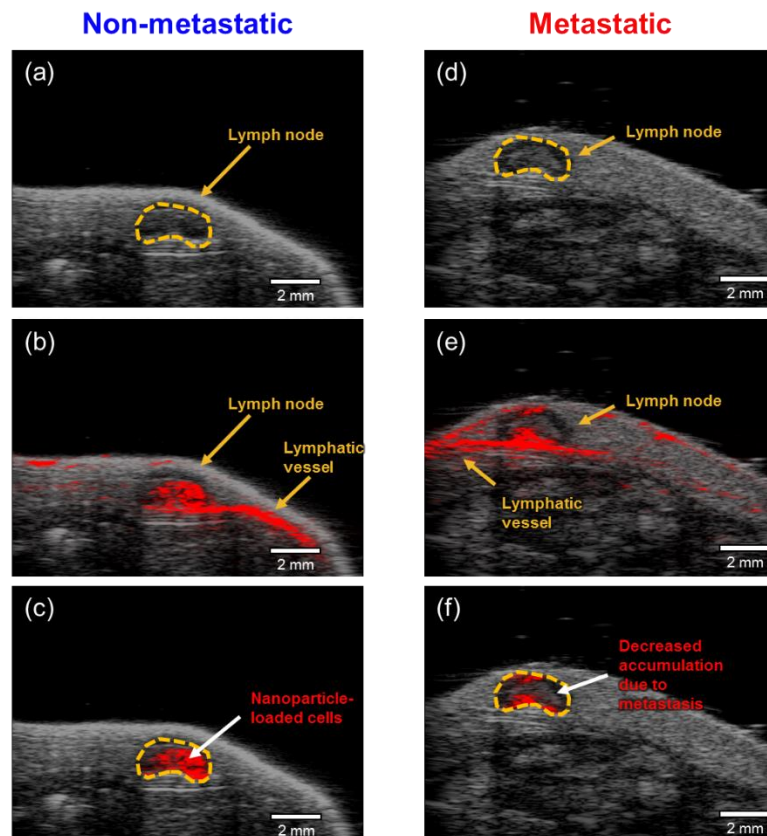


Figure 5 – Two-dimensional US/PA immunofunctional imaging 24 hours after injection. (a, d) B-mode ultrasound was used to localize the lymph nodes. (b, e) Overlaid photoacoustic imaging shows GC-AuNP-loaded cells in the lymph node and afferent lymphatic vessel. (c, f) Ultrasound-masked photoacoustic images show the effect of metastasis in nanoparticle-loaded-cell accumulation.

The behavior was further confirmed on three-dimensional images acquired using a translational motor. In the metastatic study group, the percent volume of the SLN containing GC-AuNP-loaded cells showed a statistically significant reduction of more than 2-fold compared with non-metastatic controls. Naïve mice did not show any statistically significant difference from non-metastatic tumor bearing mice (Figure 6).

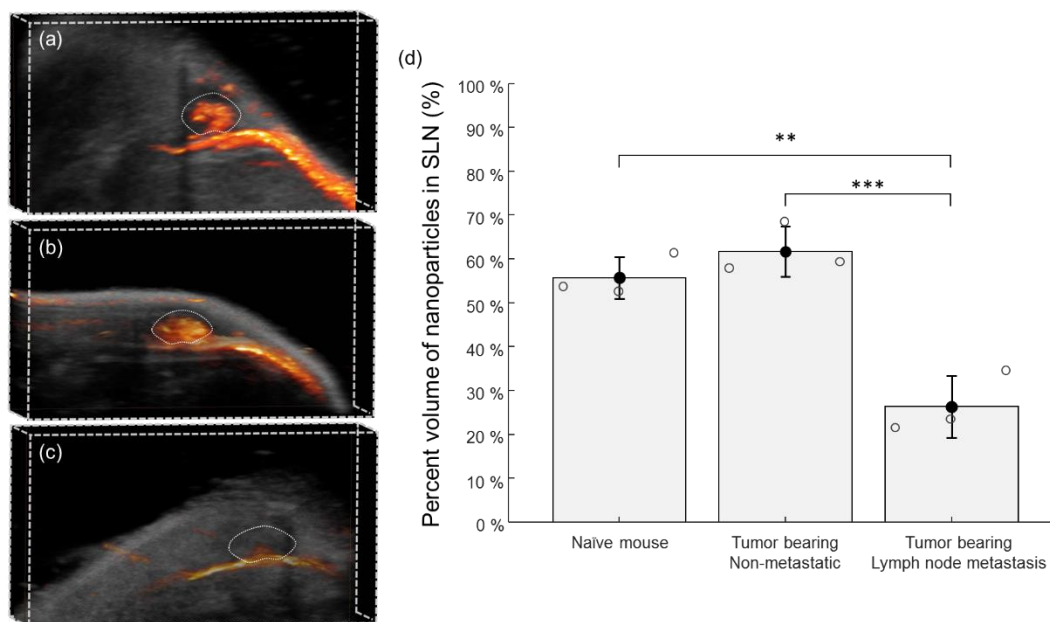


Figure 6 – 3D-rendered US/PA images of the sentinel lymph node 24 hours after injection in (a) naïve mouse, (b) tumor bearing mouse without metastasis, (c) tumor bearing mouse with metastasis. (d) The bar graph shows an over 2-fold decrease in the percent lymph node volume occupied by nanoparticle-loaded cells. Data are shown as means \pm SD (n = 3). **p = 0.002 ; *p = 0.001**

PEGylated gold nanoparticles (PEG-AuNPs) were injected in naïve mice as an additional control to confirm the immunogenicity of GC-AuNPs. Upon injection, and 24 hours after, no significant changes in PA signal were seen due to PEG-AuNPs. PEGylation prevents opsonization and thus phagocytosis by immune cells⁸⁶. Because of this, PEG-AuNPs did not show significant NIR absorption compared with GC-AuNPs (Figure 7).

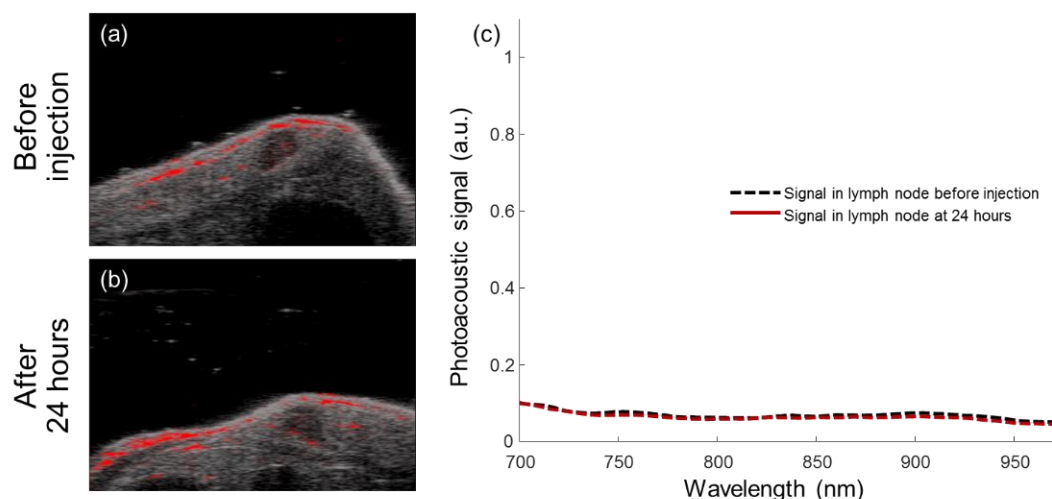


Figure 7 – Ultrasound/Photoacoustic images of a healthy sentinel lymph node in a naïve mouse (a) before and (b) 24 hours after injection of PEG-AuNPs. (c) After 24 hours, there are no significant changes in the the photoacoustic signal spectrum.

Histology results (Figure 8) were consistent with the proposed hypothesis. These results confirmed that metastatic cells inside the SLN disturb the distribution of GC-AuNP-loaded immune cells, as identified by US/PA imaging. Additionally, the nanoparticles did not coincide with cancer cells when both images were overlaid, as expected from previously described *in vitro* uptake experiments⁷³. The cited studies also showed that in non-metastatic controls, GC-AuNP were found in subcapsular sinuses across the SLN.

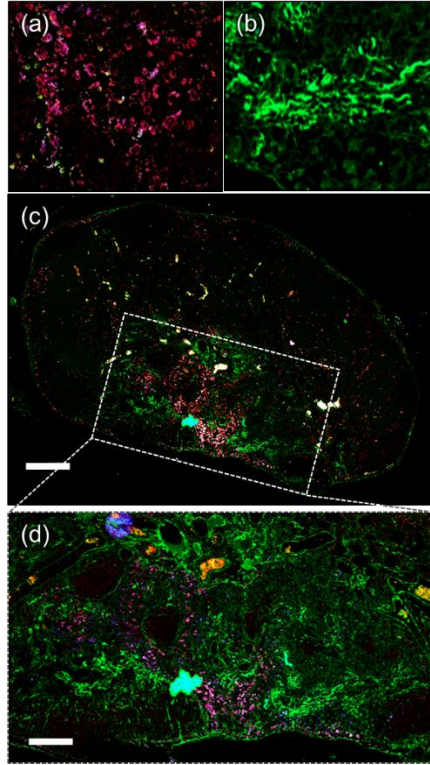


Figure 8 – Histological analysis shows (a) GC-AuNPs using dark-field microscopy and (b) cancer cells using GFP fluorescence. (c, d) The merged images show that GC-AuNPs and cancer cells do not spatially coincide. Scale bars are (c) 150 μm , and (d) 300 μm .

Results lead to presume that the metastatic foci lodged in the afferent region of the node affect the natural inflow and accumulation of nanoparticles and nanoparticle-loaded cells. Additionally, it is known that metastatic and pre-metastatic tumors induce morphological and functional remodeling in sentinel lymph nodes, including changes in the lymphatic sinuses and immune cell trafficking, as well as modulation of immune cells and immune suppression^{69, 87-88}. This may also explain why naïve mice showed slightly lower accumulation than pre-metastatic nodes. However, the differences were not statistically significant, so this is up for further investigation.

It is also noted that the lymphatic drainage and cellular uptake mechanisms of GC-AuNPs should be further studied. While a portion of the GC-AuNPs may be phagocytosed and transported to the sentinel lymph node, it is possible that some nanoparticles passively flow to the SLN where they are uptaken by lymph node resident immune cells. Some of these free-flowing particles may even be endocytosed by endothelial cells on the lymphatic vessel walls, contributing to their intense PA signal. Albeit the specific aspects and proportion of each mechanism are of interest, they are out of the scope of this study.

The *immunofunctional imaging* approach is not exempt of limitations; however, they can likely be overcome to maintain the method's utility. One of its strengths is that the statistically-significant reduction is based on the volume of the SLN containing GC-AuNP signal, as calculated via US/PA, but it is independent of the average signal intensity. Thus, the method is unaffected by changes in laser fluence or differences in skin absorption. Although a fully-invaded SLN is expected to show no PA signal, i.e., negative contrast, the advantage is that GC-AuNPs, being aggregated inside of cells, can be visualized at the lymphatic vessels on their way to the lymph node (Figure 5e), thus indicating that the drainage occurred, even if the SLN is fully invaded.

Because the nanoparticles are not in tumor cells, the method presented is independent of the molecular characteristics of the tumor and, as such, does not require expensive antibodies or sophisticated surface modifications on the contrast agent. This can be particularly useful with triple-negative tumors, such as the model used in this study.

However, potential sources of non-specificity could be caused by other lymphatic ailments, such as slow lymph flow or infections. A way to solve this issue would be to perform further molecular imaging, such as that shown by Luke, et al.²⁴ or the studies presented in CHAPTER 3 below, in the cases where *immunofunctional imaging* is inconclusive but indicates possibility of metastasis. Thus, the method is expected to be highly sensitive, with high but limited specificity in patients with ongoing lymphatic ailments. Nevertheless, many other alternative diagnostic approaches would likely be affected by such ailments as well.

The minimum number of metastatic cells to cause a distinguishable signal distribution difference is yet to be determined. In the oncology field, it is up to debate whether lesions smaller than 2 mm warrant treatment strategies any different than those in patients with no nodal involvement⁸⁹⁻⁹⁴. In this study, the diameter of the whole organ was close to 2 mm, demonstrating that the resolution of US/PA would be sufficient to identify changes in submillimeter scales. The changes seen were consistent with others shown in literature using intravenous iron oxide contrast agents¹⁰⁻¹¹. These patterns can be characterized in future trials with larger sample numbers, to create tables such as those shown using MRI and iron oxide contrast agents to identify the degree of nodal involvement⁹⁵. The proposed technique, however, would add versatility and cost-effectiveness, enhanced by a superior imaging sensitivity and resolution.

Last, the GC-AuNPs used in this study were 20 nm and, as such, do not readily clear via renal excretion. However, as a proof of concept the study was successful in identifying changes caused by SLN metastasis. The same approach may be applied using

different types of contrast agents, such as smaller ($< 5\text{nm}$) or biodegradable nanoparticles that promote renal clearance.

2.5 Conclusion

The proposed *immunofunctional imaging* approach localized immune cells with endocytosed GC-AuNPs, allowing for evaluation of their spatio-temporal distribution in the SLN. This technique goes beyond merely detecting SLN location and provides functional information that can be correlated to the presence of metastasis. The results are consistent with previous literature and in vitro studies. Additionally, this method is cost-effective because it does not require expensive imaging modalities, antibodies or sophisticated molecular targets. From a research perspective, the developed US/PA imaging tool could also advance research in basic science and areas such as immunology or immunotherapy. From a clinical perspective, the tool can aid physicians in detection of sentinel lymph node metastasis thus guiding and potentially avoiding unnecessary SLN biopsy.

CHAPTER 3. MOLECULAR PHOTOACOUSTIC IMAGING OF LYMPH NODE METASTASIS USING CLEARABLE GOLD NANOPARTICLES²

Functional imaging offers a cost-effective, “one-size-fits-all” approach that can point suspicious lymph nodes to clinicians. Upon detection, a robust diagnostic platform could also confirm the size and location of the metastatic lesions, based on molecular characteristics. Previously, Luke, et al.²⁴ introduced molecularly activated plasmonic nanosensors (MAPS) to detect lymph node micrometastasis. The MAPS consisted of 40-nm gold nanospheres targeted to the epidermal growth factor receptor (EGFR). However, it has been shown that gold nanoparticles larger than 5 nm accumulate indefinitely in the spleen and liver of mice⁹⁶. Beyond biocompatibility and long-term exposure effects, other concerns exist when nanoparticles are not cleared, such as their effect or interference with other diagnostic tests⁹⁷.

In this chapter the molecular imaging approach is further improved by investigating the use of 5-nm gold nanospheres targeted to EGFR to detect micrometastasis. Nanoparticles smaller than 5 nm in size rapidly undergo renal clearance upon intravenous administration⁹⁷. As such, they represent an excellent option towards future clinical translation of this technique.

² This chapter includes work performed in collaboration with Sangheon Han and Dr. Konstantin Sokolov from The University of Texas MD Anderson Cancer Center.

3.1 Materials and Methods

3.1.1 Gold nanoparticles

Gold nanospheres, 5 nm, were synthesized by citrate reduction method as previously described⁹⁸. Briefly, 100 ml of deionized ultrapure water was heated to 97 °C. Then, 1 ml of 10 mg/ml HAuCl₄ solution was added under stirring, followed by 1 ml of 10 mg/ml sodium citrate solution after one minute. A 1 ml solution of 0.75 mg/ml NaBH₄ in 1% sodium citrate was added to the solution one minute later. The solution was stirred for 5 minutes and transferred to an ice bath to cool down to room temperature. EGFR-targeting was performed according to previously reported methods⁹⁹.

3.1.2 Animal model

All animal procedures were approved by the Institutional Animal Care and Use Committee (IACUC) at the Georgia Institute of Technology. Five-week old female nude mice (Nu/Nu, Charles River) were inoculated submucosally in the tongue with 2×10^5 luciferase-expressing human oral squamous cell carcinoma cells¹⁰⁰ (generously provided by the lab of Dr. Jeffrey Myers, MD Anderson Cancer Center) in 30 μ l of cell media. Tumors were allowed to grow up to a 5 mm diameter prior to imaging studies. At this point, likelihood of metastasis to one or more cervical lymph nodes was high¹⁰¹.

3.1.3 Bioluminescence

Before US/PA imaging procedures, bioluminescent imaging was performed using an IVIS Spectrum CT imaging system (PerkinElmer). Mice were anesthetized and injected intraperitoneally with 150 μ l of RediJect D-Luciferin substrate (Perkin Elmer). Then, the

animal was placed inside the imaging chamber for bioluminescence imaging. Repeated scans were acquired continuously for approximately 15 minutes to achieve maximum bioluminescence emission.

After US/PA studies, the bioluminescent imaging procedure was repeated under terminal anesthesia. After luciferin injection, the tongue was resected to remove the tumor from the field of view, thus acquiring bioluminescence signals from metastatic cells only.

3.1.4 Ultrasound and photoacoustic imaging

Mice were anesthetized and injected peritumorally in the tongue with 30 μ l of EGFR-targeted gold nanoparticles, corresponding to approximately 50 μ g of gold. Combined ultrasound and multiwavelength photoacoustic imaging of the cervical lymph nodes was performed immediately after, using a Vevo LAZR with 40 MHz LZ-550 transducer. The wavelength acquisition range was from 680 nm to 970 nm, in steps of 2 nm. The lymph nodes were imaged continuously for 3 hours. Mice were allowed to wake up and underwent US/PA imaging under anesthesia 24 hours after, following the same protocol as day 1.

3.1.5 Multiwavelength spectroscopic analysis

Spectroscopic analysis was performed following a previously-reported method³⁸ based on a linear least squares (LLS) algorithm. In vivo PA imaging data were used as input to the unmixing algorithm. The absorption spectra of oxygenated hemoglobin, deoxygenated hemoglobin, and plasmon-coupled nanoparticle spectra were used as parameters.

The output consisted of three image matrices, corresponding to concentrations of oxygenated hemoglobin (HbO₂), deoxygenated hemoglobin (Hb), and nanoparticles (AuNP) in arbitrary units. All resulting images were overlaid on the raw ultrasound image using different colormaps.

To avoid skin signals, ultrasound-based segmentation was applied. Ultrasound signals above 20 dB were used as input to an edge detection algorithm¹⁰². Then, the skin edge was dilated in the z (depth) direction assuming a skin thickness of approximately 400 μm , based on literature reports of mouse skin thickness¹⁰³.

3.2 Results and discussion

Bioluminescence imaging confirmed presence of metastatic cells prior to US/PA imaging (Figure 9). The proximity of the primary tumor and the cervical sentinel lymph node, together with the poor spatial resolution inherent to bioluminescence imaging at this depth, did not allow to evaluate metastasis with certainty. After terminal tongue resection (removal of the primary tumor) it was clear that the sentinel node was invaded, due to the strong bioluminescence signal detected.

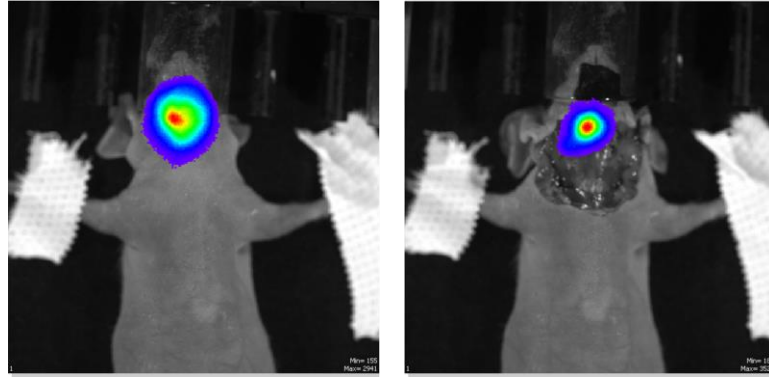


Figure 9 – Bioluminescence image of lymph node metastasis prior (left) and after (right) tongue tumor removal.

In ultrasound and photoacoustics, skin can be a source of unwanted signals. This can be due to skin pigmentation or accumulation of impurities on the skin that cause optical absorption hot spots, or small air bubbles causing hyperechoic regions and artifacts. Particularly, for detection of small cancer cell foci in the lymph node, the photoacoustic signal intensity may not be high enough to be distinguished from blood, skin, or image artifacts. Multiwavelength PA allows to detect and isolate signals with spectra corresponding to gold nanoparticles. However, skin artifacts can have unpredictable spectra that may be incorrectly detected as nanoparticles by spectral unmixing algorithms. Because of this, a skin segmentation algorithm was applied prior to spectral unmixing, based on ultrasound intensity and assuming a skin thickness of approximately 400 μm (Figure 10), and signals from this region were rejected.

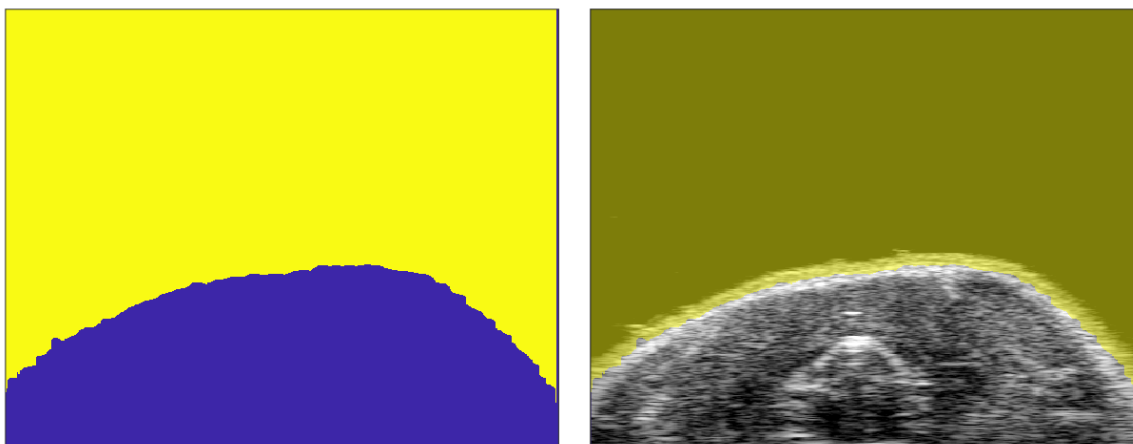


Figure 10 – Ultrasound-based skin segmentation images. A mask (left) was created by detecting the edge of the skin and assuming a 400 μm thickness. Only the blue area is preserved. The mask is overlaid (right) with the b-mode ultrasound to show the rejected skin area.

Upon injection of EGFR-targeted AuNPs, multiwavelength US/PA imaging was performed. After 20 minutes, a localized aggregation of nanoparticles became noticeable on the right cervical lymph node (sentinel node). The aggregation was confirmed and isolated from blood signals using spectroscopic analysis (Figure 11). This localized signal indicated presence of metastasis and persisted over the course of the imaging session, which lasted 3 hours. After 24 hours, no noticeable nanoparticle signals were detected, suggesting a decrease in aggregation and plasmon coupling due to nanoparticle dynamics such as being exocytosed by the cancer cells.

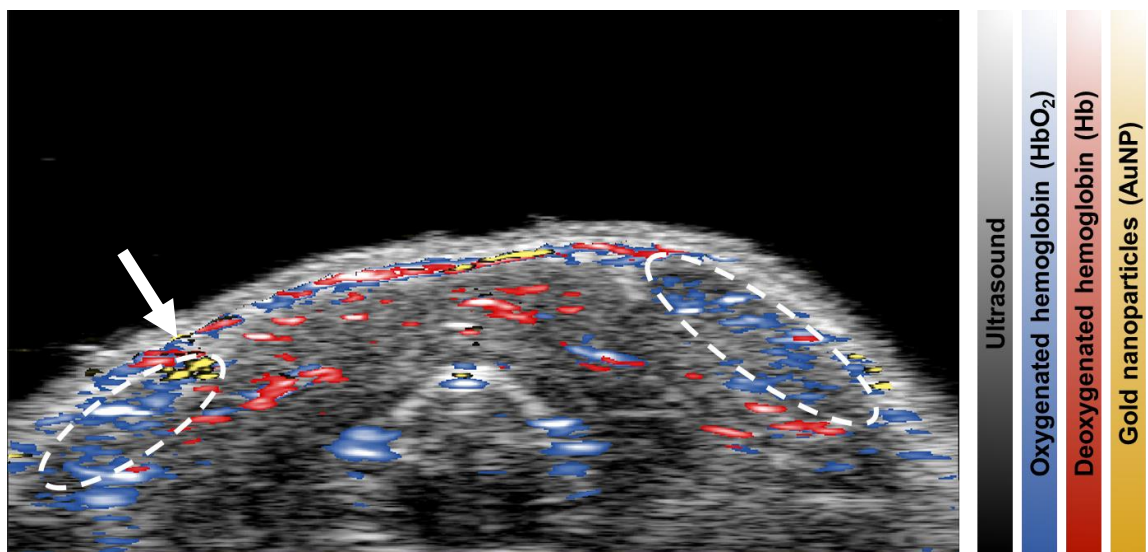


Figure 11 – Ultrasound and spectroscopic photoacoustic image of a murine neck axial cross section showing the cervical lymph nodes (whited dashed contours), 2 hours after injection of EGFR-targeted AuNPs. The colormaps show oxygenated hemoglobin (blue), deoxygenated hemoglobin (red), and aggregated gold nanoparticles (yellow). Metastasis is indicated by localized aggregation of gold nanoparticles (white arrow).

The results are promising regarding the feasibility of clearable gold nanoparticles for molecular imaging of lymph node metastasis. It is important to note, however, that further studies are needed to fully evaluate the sensitivity and specificity when small nanoparticles are used compared to previous literature using 40-nm gold spheres.

In part, the results differ from those shown by Luke, et al.²⁴ in the sense that those studies using 40-nm nanoparticles showed a more progressive aggregation of nanoparticles over the course of 125 minutes, with little to no nanoparticle signal in the first 25 minutes. In contrast, when using 5-nm nanoparticles the signal appeared within the first 20 minutes and remained relatively steady during the imaging session. It is possible that larger 40-nm nanoparticles have slower drainage dynamics than the smaller 5-nm ones used herein. If

so, this would be an additional advantage of using 5-nm gold particles, which would provide faster results and reduce procedure times.

Because nanoparticles were not detected during the second imaging session, results suggest that the nanoparticles may start to clear the area after 24 hours. More studies are needed to confirm this hypothesis. For instance, harvesting the lymph node at different time points after injection and drainage would allow to perform histological analysis to assess colocalization of nanoparticles and cancer cells, and confirm successful clearance. Immunohistochemistry for EGFR expression and silver staining would be viable methods to evaluate colocalization and clearance. Biodistribution studies are also necessary to confirm renal excretion and study any remaining gold in organs such as spleen and liver.

Additional experimental groups are also needed to fully evaluate the accuracy of this technique. For instance, a larger number of cancerous mice would help assess the sensitivity of the method, while the use of non-cancerous controls or non-specific antibodies could assess the specificity of the technique.

The low imaging sensitivity of this technique is a limitation and requires spectroscopic analysis to determine the location of metastasis. Increasing the injected agent concentration could increase contrast, but it may imply additional cost and dosage concerns. The use of multimodal contrast agents may solve this weakness by improving imaging sensitivity and will be discussed in subsequent chapters of this document.

3.3 Conclusion

Using US/PA and targeted nanoparticles, it was possible to precisely detect lymph node metastasis non-invasively. Because the contrast agent is expected to clear via renal excretion, the presented results constitute a step towards potential clinical translation. More studies are needed for statistical analysis to obtain the sensitivity and specificity of this method in comparison with previous literature. Additionally, renal clearance must be confirmed and characterized with more thorough biodistribution studies. Gold nanospheres offer the advantage of acting as sensors, thus differentiating between free nanoparticles (invisible) and uptaken nanoparticles. Access to alternative multimodal contrast agents that can act as sensors and provide higher sensitivity could further augment the diagnostic value and could increase the range of possibilities for clinical trials, in case additional safety concerns persisted for gold nanoparticles.

CHAPTER 4. ENHANCED SENSITIVITY WITH A DUAL MODE NANOSENSOR FOR MOLECULAR IMAGING³

Numerous biomarkers play a significant role in medical imaging for oncology, cardiology, immunology, among other areas. Identifying the presence of different types of molecules and cells, together with environmental cues, such as pH and oxygenation, can be critical for diagnosis, therapy and monitoring of disease.

Contrast agents are commonly used to enable and enhance biomarker visualization^{27, 104-109}. In many cases, imaging applications can further benefit from responsive contrast agents that are able to interact and change with the environment, elucidating the status of one or more biomarkers. Examples include imaging of cancer cells^{24, 110}, immune cells¹¹¹⁻¹¹², pH¹¹³⁻¹¹⁴ or enzyme activity¹¹⁵⁻¹¹⁶. Particularly, CHAPTER 3 introduced the use of gold nanoparticles to target cellular receptors in cancer cells. While the approach is promising, it could be further enhanced in aspects such as sensitivity and ease of clinical translation.

The choice of imaging modality is dependent on the desired sensitivity, spatial and temporal resolution, cost, safety, and the ability to provide structural, functional or molecular information. Unfortunately, no single modality excels in all these attributes¹¹⁷⁻¹¹⁸. Particularly, technologies such as PET and fluorescence imaging exhibit high sensitivity but suffer from poor spatial resolution. Conversely, others such as MRI,

³ Part of this chapter is adapted from a proceeding manuscript titled ‘Co-registered photoacoustic and fluorescent imaging of a switchable nanoprobe based on J-aggregates of indocyanine green’ (Dumani, et al 2018). Diego Dumani is the primary author of this manuscript.

ultrasound, and photoacoustic imaging allow superior resolution at the expense of limited sensitivity due to lower signal-to-background ratio. By using multimodal imaging approaches, high resolution images may be achieved while synergistically boosting detection sensitivity¹¹⁹⁻¹²⁰.

Previously, the use of liposome-encapsulated J-aggregates of indocyanine green (ICG) (Figure 12A), named PAtrace, was introduced as an environment responsive agent for photoacoustic imaging (PA)¹²¹⁻¹²². This contrast agent has an optical absorption peak at 890 nm that blue-shifts to 780 nm upon interaction with cells or environment (Figure 12B). This shift is caused by the rupture of the liposome, which releases the ICG J-aggregate, subsequently breaking down into free ICG molecules. Besides the absorption spectrum shift, detectable via photoacoustic imaging, the process also enables fluorescence emission detected above 800 nm, a long-known characteristic of ICG¹²³⁻¹²⁵.

In this chapter, the multimodality of PAtrace is exploited by using a platform integrating a 3D photoacoustic/fluorescence tomography (PAFT) instrument. The system simultaneously acquires both imaging components using the same laser pulse as excitation, thus allowing co-registration. First, phantom results are shown to validate the photoacoustic detection prior to activation, and multimodal detection after activation. Last, in vivo results of particle drainage and activation are shown in a murine inguinal lymph node.

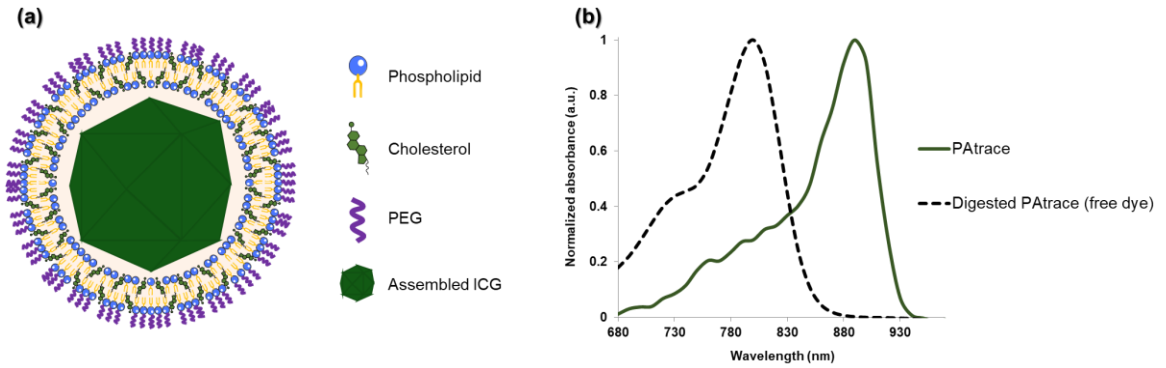


Figure 12 – (a) Schematic of PAttrace shows an ICG J-aggregate encapsulated by a phospholipid and cholesterol shell. (b) Absorption spectra of intact and digested PAttrace. Before interaction, a sharp peak at 890 nm is obtained. After interaction with cells or environment, free ICG absorption spectrum is recovered.

4.1 Materials and methods

4.1.1 Photoacoustic/Fluorescence imaging setup

Tomographic photoacoustic and fluorescence imaging was simultaneously performed using a PAFT system, as described by Brecht *et al*¹²⁶. Briefly, the sample holder is vertically inserted in a water tank where laser excitation is delivered by four orthogonal fiberoptic illuminators, using a Phocus Mobile tunable laser (Opotek Inc). The laser can be tuned between 690 nm and 970 nm, with a 10 Hz repetition rate, and 5 ns pulse duration. Fluence at the phantom or skin surface was kept below the American National Standard Institute (ANSI) safety limits. Photoacoustic images are acquired with a 96-element array transducer, 6 MHz center frequency. Fluorescence is acquired with a scientific CMOS camera Dhyana 400D (Tucsen Photonics) equipped with a fluorescence emission filter matching the emission spectrum of ICG. During the scan, the sample rotates at $10^{\circ} \cdot s^{-1}$ while tomographic slices are registered for full-volume offline reconstruction using standard filtered backprojection.

4.1.2 Phantom imaging

A phantom was designed containing five ultrathin wall polytetrafluoroethylene (PTFE) tubes, 0.9 mm diameter (Zeus, Inc.). Each tube was filled with a different contrast agent as represented in Figure 13A. Optical densities of the agents were matched to $OD = 5 \text{ cm}^{-1}$ at their respective absorption peak. The phantom included PAtrace in DI water, PAtrace in Triton X-100, free ICG solution, and cupric sulfate (CuSO_4) solution. Triton X-100 is a surfactant that breaks down liposomes and monomerizes the ICG, simulating the activation and environment interaction that particles would undergo in vivo. The CuSO_4 solution was used as a reference to normalize wavelength-dependent laser fluence variations.

The tube ends were sealed with glue to prevent leakage, and one hour was allowed for the glue to dry. Then, the phantom was placed vertically in the sample holder and inserted into the water tank (temperature = 25°C). Images were acquired using 780 nm (multimodal) and 890 nm (PA only) laser excitation.

4.1.3 In vivo imaging

A naïve mouse (Nu/Nu, Charles River Laboratories) was used as part of a protocol approved by the Institutional Animal Care and Use Committee (IACUC) at the Georgia Institute of Technology. The animal was injected with $40 \mu\text{l}$ of PEGylated PAtrace ($OD = 80 \text{ cm}^{-1}$) in the right caudal mammary fat pad. The particles were allowed to drain to the inguinal lymph node for 24 hours. The mouse was then anesthetized and positioned in a restrainer with a free-breathing anesthesia delivery system (Figure 14). The restrainer was vertically placed in the sample holder and inserted into the water tank. Water temperature

was kept at 37 °C. Images were then acquired with PAFT system using 780 nm (multimodal) and 890 nm (PA only) wavelengths.

Two-dimensional spectroscopic PA images were subsequently acquired using a Vevo LAZR system as previously described in section 2.3.2.

4.2 Results and discussion

The results of the PAFT phantom imaging showed successful detection of PAtrace activation, both photoacoustically and fluorescently. Upon activation, PAtrace is expected to lose 890-nm absorption, and gain 780-nm absorption, together with reinstated fluorescence. The free ICG solution displayed a similar behavior to that of digested PAtrace, as expected.

A front view of the phantom (Figure 13B) shows no fluorescence for intact PAtrace, and high fluorescence emission for digested PAtrace, as well as free ICG. While all tubes are in the field of view, only tubes 2 and 3 are visible. Tube 1, and support rods are slightly discernible, due to a small leakage of excitation light. At 890 nm, only intact PAtrace was detected via PA imaging (Figure 13C). PA images at 780 nm show high contrast for activated PAtrace and free ICG, but low signal when PAtrace is intact (Figure 13D).

The tube containing CuSO₄ showed no fluorescence. It was photoacoustically detected both at 890 nm and 780 nm. Due to its known absorption spectrum, it was used to normalize PA intensities and account for wavelength-dependent laser fluence variations. The tube with DI water was not visible with either modality, showing that the PTFE tubes had no contribution to background signal.

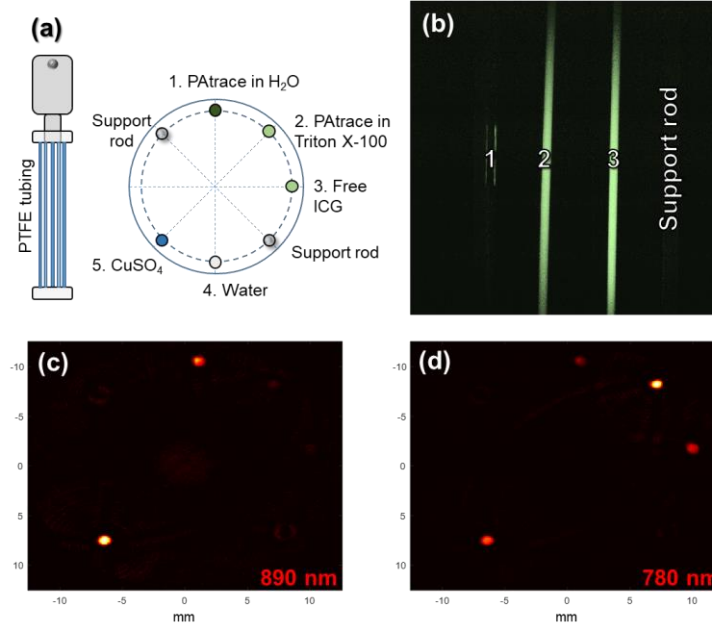


Figure 13 – (a) Schematic of PAFT phantom design. On the left is the phantom, on the right is a horizontal slice view. (b) Fluorescence image showing tubes 1, 2, and 3, using 780 nm excitation. Tubes 4, 5, and support rods are not visible. (c) Horizontal slice view of PA at 890 nm. (d) Horizontal slice view of PA at 780 nm. The tubes' positions are matched in (a), (c), and (d) horizontal slices

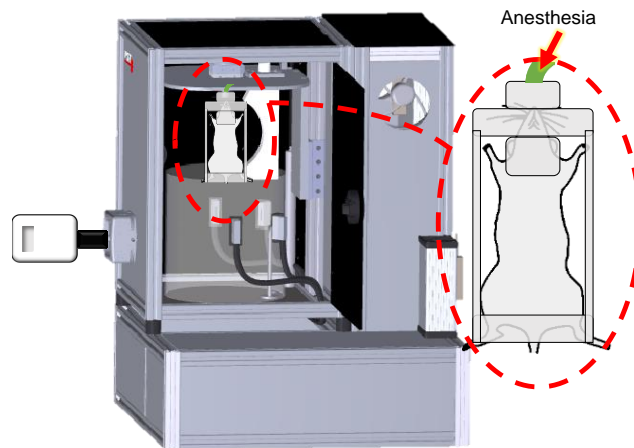


Figure 14 – Schematic of mouse restrainer and its position in PAFT system.

In vivo results showed feasibility of this platform for use in preclinical studies. The injection site and draining lymph node were clearly identified in PA images at 780 nm

(Figure 15). Endogenous absorption, coming predominantly from deoxygenated blood, was also visible. On the other hand, fluorescent images showed high emission at the lymph node but very low background signals. High PA contrast and fluorescence at 780 nm excitation indicate activation of PAttrace, most likely due to cellular uptake. This suggests that the contrast agent may have been endocytosed at the injection site and then trafficked to the lymph node via immune cells. Another possibility is that the particles were also digested by lymph node resident cells after passive drainage to the lymph node occurred.

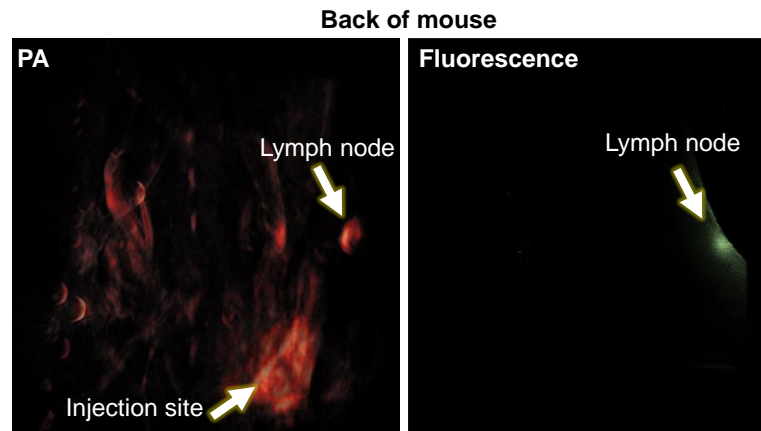


Figure 15 – Photoacoustic (PA) 2D projection and fluorescence images of a mouse (dorsal view) using 780 nm laser excitation

Additionally, Vevo LAZR was used to confirm the spectral shift by performing multiwavelength PA imaging (Figure 16). While the injection site shows a peak absorption at 890 nm, the lymph node shows the highest absorption between 780 nm and 800 nm. This implies that the particles were digested in this region or digested at the injection site and transported to the node. In this study, the PEGylated PAttrace particles were not targeted to any specific biomarker. Because of this, a solution with a high optical density was injected to maximize non-specific cellular uptake and particle activation. The mechanism may be

due to several reasons such as immune cell uptake before or after drainage to the node, in addition to environment and interstitial pressure differences. In the future, the phospholipid shell of PAtrace could be functionalized to interact with specific cell types, molecules, or environmental cues. Then, a much lower amount of contrast agent would be needed, given the potentially higher uptake activity, together with the sensitivity boost that fluorescence provides. Additionally, smaller timeframes could be used, such as the molecular imaging paradigm for sentinel lymph node metastasis introduced in CHAPTER 3.

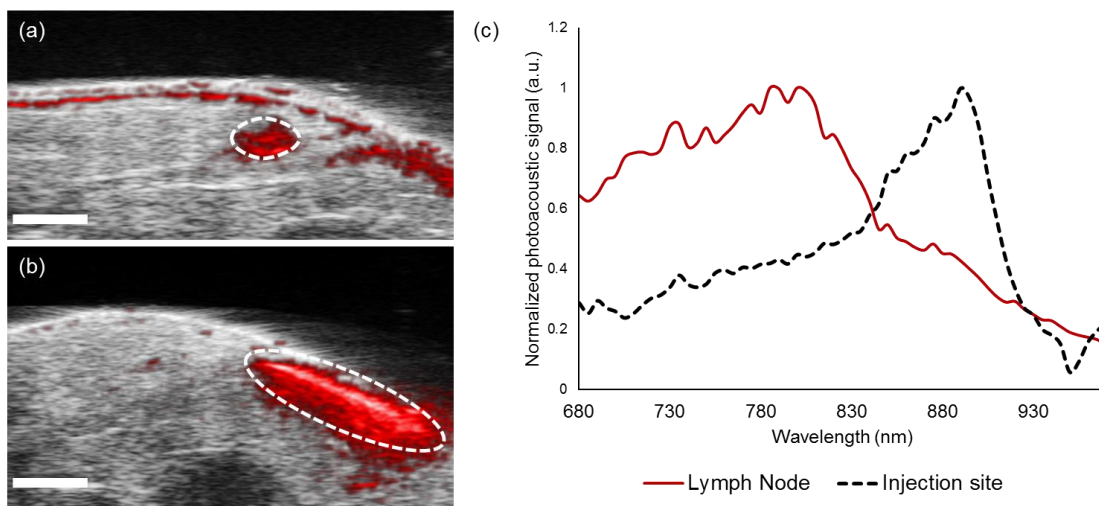


Figure 16 – US/PA images 24 hours after injection. The dashed white lines indicate the location of (a) the inguinal lymph node and (b) subcutaneous injection site. (c) The graph shows the spectral shift due to digestion of the liposomes.

By using a responsive multimodal agent, there is no requirement for complex image registration between reference and detection scans. Additionally, PA imaging of endogenous absorbers could also be used to complement the obtained molecular information with functional parameters such as blood oxygenation. As such, this contrast agent could further enhance molecular imaging of lymph node metastasis.

4.3 Conclusions

An environment responsive contrast agent (PAtrace) was investigated using a combined photoacoustic/fluorescence tomography (PAFT) imaging system. The synergy of photoacoustic and fluorescent imaging modalities can be exploited to enhance sensitivity and resolution of the system. Studies showed successful activation and detection of PAtrace in a phantom and in vivo. These preliminary studies suggest the feasibility of this agent for sentinel lymph node imaging. The introduced approach can be used in various applications including oncology, cardiology, immunology, and many others. Future studies will include surface functionalization of the contrast agent for applications in lymph node metastasis detection, but the agent could also be applied to evaluate primary tumors, as well as for other diseases such as atherosclerotic plaque characterization.

CHAPTER 5. A GOLD-SILICA JANUS NANOSENSOR TO ENHANCE DIAGNOSTIC AND THERAPEUTIC POTENTIAL⁴

In Chapters 1 and 2, gold nanoparticles (AuNPs) were exploited to elucidate functional and molecular characteristics of sentinel lymph nodes. Gold nanoparticles have been particularly attractive for use as exogenous contrast agents because their characteristic local surface plasmon resonance (LSPR) efficiently converts light energy into heat, providing high contrast in PA imaging³¹. Moreover, the optical properties of AuNPs can be altered by varying their size, morphology, or surface coating to modulate the frequency of the LSPR that determines the optical wavelength¹²⁷. The biocompatibility of AuNPs and the ease of surface modification are also attractive for applications in targeted delivery¹²⁸. To enhance imaging performance and stability, AuNPs have been coated with silica shells, which are also biocompatible and easily modified by well-defined silane chemistry¹²⁹. Silica shells can significantly enhance the colloidal stability and photostability of gold nanostructures, and improve the PA conversion efficiency by reducing the interfacial thermal resistance between gold and the surrounding medium¹³⁰. Once the AuNPs are fully coated with silica, however, it is difficult to modulate their optical properties¹³¹, thus they would not act as sensors of cellular uptake. In this chapter, it is hypothesized that a partial silica coating on AuNPs can retain some exposed gold surfaces to facilitate the modulation of the optical properties, while simultaneously enhancing colloidal stability, with weaker inter-particle van der Waals interactions due to the lower Hamaker constant of silica than

⁴ Part of this chapter is adapted from a manuscript titled ‘Tunable aggregation of gold-silica janus nanoparticles to enable contrast-enhanced multiwavelength photoacoustic imaging in vivo’ (Park, Dumani, Arsiwala, Emelianov, Kane, 2018). Diego Dumani is equally-contributing primary author of this manuscript.

that of gold ($A_{\text{silica}} = 1 \times 10^{-20}$ J and $A_{\text{Au}} = 4 \times 10^{-19}$ J), in response to local environment changes and laser radiation¹³².

In this chapter, the synthesis of AuNPs coated with anisotropic silica shells is demonstrated and their colloidal behaviors in cell culture media (CCM) are investigated. A controlled aggregation of AuNPs with anisotropic silica shells was found in CCM, enabling an amplification of PA signals in the NIR region. The PA properties of the resulting nanostructures were investigated using phantoms simulating biologically relevant environments, such as tissue-mimicking phantoms containing breast cancer cells. Additionally, the use of the contrast agent in vivo was demonstrated using a naïve murine model. The ability to modulate AuNP aggregation in response to a range of stimuli in combination with high resolution and deep penetration of NIR PA imaging are very attractive for a broad range of biomedical imaging and therapeutic applications.

5.1 Janus nanoparticle design

To achieve the synthesis of AuNPs with anisotropic silica shells, it is first necessary to have monodispersed AuNPs. AuNPs with a diameter of 30 nm were chosen as the core material. The synthesis of citrated AuNPs was performed based on a seed-mediated growing method¹³³. AuNPs have been anisotropically coated by various methods including polymer-guided self-assembly¹³⁴ and chemical deposition¹³⁵. The self-assembly of polyacrylic acid (PAA, Mw: 250,000 Da) and 4-mercaptobenzoic acid (4-MBA) was used to synthesize AuNPs coated with anisotropic silica shells. Both PAA and 4-MBA have strong affinity for the surface of AuNPs. While the carboxylic acid moieties mediate the binding of PAA to AuNPs¹³⁶, the thiol-gold interaction is dominant for interactions of

4-MBA with AuNPs¹³⁷. Due to the different anchoring motif of PAA and 4-MBA, tuning the ratio of PAA and 4-MBA results in AuNPs with part of the surface coated with PAA and the remaining part coated with 4-MBA¹³⁸. 4-MBA-coated AuNPs promote silicification under specific conditions (basic pH, alcohol-water cosolvent system, using hydrolysable silane precursors) because the high interfacial energy of the gold-ligand-solution interface promotes the initiation of heterogeneous nucleation for silicification. On the other hand, PAA-coated AuNPs do not promote silicification¹³⁴. AuNPs with PAA and 4-MBA were prepared in a 2-propanol/water co-solvent, and then anisotropic silica shells were generated in situ by the addition of silica precursor – tetraethyl orthosilicate (TEOS) – in the presence of ammonia. The resulting AuNPs with anisotropic silica shells are hereinafter referred to as gold-silica janus nanoparticles (GSJNPs).

5.2 Materials and methods

Unless otherwise specified, reagents were used as received without further purification. Gold(III) chloride trihydrate ($\text{HAuCl}_4 \cdot 3\text{H}_2\text{O}$ $\geq 99.9\%$), sodium citrate tribasic dehydrate ($\geq 99\%$), 2-propanol (ACS reagent $\geq 99.5\%$), ethyl alcohol (ACS reagent $\geq 99.5\%$), ammonium hydroxide solution (ACS reagent 28.0-30% NH_3 basis), tetraethyl orthosilicate (TEOS, 99.999%), 4-mercaptobenzoic acid (4-MBA, 99%), poly(acrylic acid) solution (PAA, Mw: 250,000, 35 wt% in H_2O), Dulbecco's Phosphate Buffered Saline (DPBS, 10 \times , modified), gelatin from porcine skin (gel strength 300, Type A), and silica gel (pore size 60 Å, 230-400 mesh particle size, 40-60 mm particle size) were purchased from Sigma-Aldrich. Dulbecco's Modified Eagle Medium with 10% Fetal Bovine Serum (DMEM with 10% FBS, no phenol red) was purchased from Thermo Fisher Scientific.

MTT cell viability assay kit was purchased from Biotium. Deionized water (DI water) was purified using a Millipore Milli-Q system (18 M Ω).

5.2.1 Nanoparticle characterizations

Dynamic light scattering data were measured with a Zetasizer Nano ZS (Malvern, UK). Transmission electron microscopy (TEM) was performed using a Tecnai F30 (FEI Company, USA) equipped with energy dispersive X-ray spectroscopy (EDS, Oxford Instruments) for element analysis and a HT-7700 (Hitachi, Japan) for general imaging purpose. UV-Vis spectra and optical density were taken with an Evolution 220 spectrometer (Thermo Fischer Scientific). Cell cytotoxicity of GSJNPs was analyzed by a plate reader (SpectraMax i3x, Molecular Devices). Ultrasound/photoacoustic (US/PA) images were acquired using an integrated ultrasound-photoacoustic imaging system (Vevo LAZR, FUJIFILM VisualSonics, Inc.) with ultrasound transducers LZ-250 and LZ-550.

5.2.2 Synthesis of citrate-stabilized AuNPs

Synthesis of citrate-stabilized AuNPs was performed as described elsewhere¹³³. Briefly, an aqueous citrate solution (2.2 mM, 150 mL) was refluxed by heating in oil-bath. After 10 min, 1 mL of an aqueous solution of HAuCl₄ (25 mM) was added to the reaction vessel. The color of the solution turned to blue and then to red. After 20 min of reflux, the temperature of reaction mixture was cooled down until it reached 90 °C. To this solution, 1 mL of an aqueous solution of HAuCl₄ (25 mM) and 1 mL of aqueous citrate solution (60 mM) were added sequentially (time gap: 2 min) to achieve a seeded growth of AuNPs. After 30 min of incubation, sequential injections were repeated until the size of AuNPs reached up to 30 nm in diameter.

5.2.3 *Synthesis of GSJNP and GSCSNP*

To synthesize GSJNP with 30 nm of AuNP, the protocol was modified based on a previous report¹³⁹. PAA and 4-MBA solutions were prepared in DI water (0.042 mM) and ethanol (5 mM) respectively. A 2-propanol/water co-solvent system was prepared with 38 mL of 2-propanol and 12 mL of DI water. To this solution, 400 μ l of both PAA and 4-MBA solutions were added and stirred for 10 min. In parallel, 10 mL of as-prepared citrate-stabilized AuNPs were washed with the same amount of DI water. The resulting AuNP solution was added dropwise to the reaction mixture of PAA and 4-MBA in 2-propanol/water co-solvent. After 30 min, 1.8 mL of aqueous ammonium hydroxide solution (28-30%) was added to maintain the basic pH, and then 12 mL of TEOS solution in 2-propanol (8.96 mM) was added to form the anisotropic silica coating. The reaction mixture was gently stirred for 12 hours. After the reaction, the products were washed with a 1:1 mixture of 2-propanol and DI water, and filtered using a syringe filter equipped with 0.2 μ m pores to remove unwanted aggregates. For GSCSNP, the synthesis was proceeded following the same protocol for GSJNP except the addition of PAA.

5.2.4 *Photoacoustic imaging with PTFE tube phantoms*

Aqueous solutions of GSJNP and GSCSNP in DI water were concentrated by centrifugation, and the resulting pellets were re-dispersed in DMEM with 10% FBS (final optical density (OD) = 2 cm^{-1}). Two polytetrafluoroethylene (PTFE) tubes 0.89 mm in diameter (Sub-Lite-Wall®, Zeus Inc.) were filled with 50 μ L of GSJNP and GSCSNP solutions, and the resulting tubes were placed horizontally in a water chamber filled with DI water for US/PA imaging characterization. US/PA images of both tubes were acquired

simultaneously using an integrated ultrasound-photoacoustic imaging system (Vevo LAZR), with a 20 MHz LZ-250 transducer. Light was delivered via integrated optical fiber, using a nanosecond pulsed laser with 20 Hz repetition rate and an optical parametric oscillator (OPO) emitting from 680 nm to 970 nm. For single wavelength images, 100 frames were acquired at 700 nm excitation and then averaged for signal comparison.

5.2.5 Preparation of GSJNP-Loaded Cells

Two cell lines were chosen to prepare GSJNP-loaded cell samples. Macrophages (J774A.1 cell line) and human breast cancer cells (MDA-MB-231 cell line) were grown in DMEM with 10% FBS to confluency. Upon confluency, a small volume of concentrated GSJNP solution was added into the cell culture medium to fix the final OD of GSJNP at 2.0. The cells were incubated with GSJNP for 48 h at 37 °C and then the GSJNP-loaded cells were collected by centrifugation. The cells were fixed using 10% buffered formalin, and re-dispersed in PBS. The resulting solution of GSJNP-loaded cells was used to create inclusions as part of a gelatin tissue-mimicking phantom.

5.2.6 Photoacoustic imaging with tissue-mimicking gelatin phantom

A tissue-mimicking phantom was made with aqueous solutions of gelatin and silica gel particles in DI water. The final concentrations of gelatin and silica gel particles were fixed at 6 wt% and 0.2 wt%, respectively, to simulate optical and ultrasound scattering of biological tissues. The solution mixture was heated over 45 °C while mechanical stirring until the solution became homogeneous, and then placed in a vacuum chamber for 5 min for a degassing process. The solution (300 ml) was then poured into a plastic mold and refrigerated overnight to be solidified. The resulting gelatin block was used for the basal

structure to support the gelatin inclusions containing GSJNP-loaded cells to be analyzed. The gelatin inclusions were prepared by mixing an aqueous solution containing gelatin (12 wt%) and silica gel particles (0.4 wt%) with an aqueous solution of GSJNP-loaded cells at 1:1 volume ratio. A 15 μ L drop of the resulting solution was placed onto the previously made gelatin block to create dome-shaped gelatin inclusions. The resulting phantoms were refrigerated for 4 hours before the US/PA imaging analysis. US/PA images were acquired and analyzed with Vevo LAZR following the same protocol described above, using a 40 MHz LZ-550 transducer.

5.2.7 Characterization of cytotoxicity of GSJNP

Human embryonic kidney cells 293T (HEK 293T) were seeded in a U-bottom 96-well plate at a density of 10,000 cells/well and cultured in DMEM with 10% FBS at 37 °C in 8% CO₂ for 24 h. After aspirating the supernatant of each well, the cells were treated with varying amounts of GSJNP in a total volume of 100 μ L of DMEM with 10% FBS for 24 h. 10 μ L of MTT solution was added to 100 μ L of medium in each well and further incubated at 37 °C in 8% CO₂ for 4 h. 200 μ L of DMSO was added to solubilize the mixture and dissolve the formazan salt. The absorbance at 560 nm (signal from blue formazan) was measured with a plate reader and background absorbance at 630 nm was subtracted from the signal absorbance to obtain normalized absorbance values. All experiments were performed in triplicate. The relative cell viability was normalized relative to the untreated control cells.

5.2.8 *Ultrasound and photoacoustic imaging in vivo*

All animal procedures were approved by the Institutional Animal Care and Use Committee (IACUC) at the Georgia Institute of Technology. Naïve nude mice were anesthetized and injected subcutaneously in the mammary fat pad area with 60 μ l of GSJNP or GSCSNP, at an optical density of 4.6 cm^{-1} . Combined ultrasound and multiwavelength photoacoustic imaging was performed at the injection site immediately after, using a Vevo LAZR with 40 MHz LZ-550 transducer. The wavelength acquisition range was from 700 nm to 970 nm, in steps of 2 nm. The particles were allowed to drain for 24 hours to the nearest inguinal lymph node, which was then imaged under anesthesia following the same protocol as day 1. Following imaging experiments the mice were euthanized by CO₂ asphyxiation.

5.2.9 *Multiwavelength spectroscopic analysis*

Spectroscopic analysis was performed following a previously-reported method³⁸ based on a linear least squares (LLS) algorithm. In vivo PA imaging data were used as input to the unmixing algorithm. The absorption spectra of oxygenated hemoglobin, deoxygenated hemoglobin, together with nanoparticle spectra obtained in vitro, were used as parameters.

The output consisted of three image matrices per mouse, corresponding to concentrations of oxygenated hemoglobin (HbO₂), deoxygenated hemoglobin (Hb), and nanoparticles (AuNP) in arbitrary units. All resulting images were overlaid on the raw ultrasound image using different colormaps.

5.3 Results and discussion

The morphologies of GSJNPs were characterized by transmission electron microscopy (TEM) (Figure 17) and their atomic composition using high-resolution TEM in combination with energy-dispersive X-ray spectroscopy (EDXS). The point analysis of atomic composition indicated the presence of silicon and gold atoms and confirmed the presence of a silica shell and AuNP core (Figure 18). Averaging data from a hundred GSJNPs, the size of GSJNPs was calculated to be 45.9 ± 5.9 nm and the thickness of the silica shells 16.6 ± 2.7 nm. Additionally, AuNPs coated with isotropic silica shells – gold-silica core-shell nanoparticles (GSCSNPs) – were synthesized by using 4-MBA as the sole ligand (without any PAA) and characterized by TEM. The thickness of silica shells for GSCSNPs was calculated to be 25.0 ± 2.3 nm.

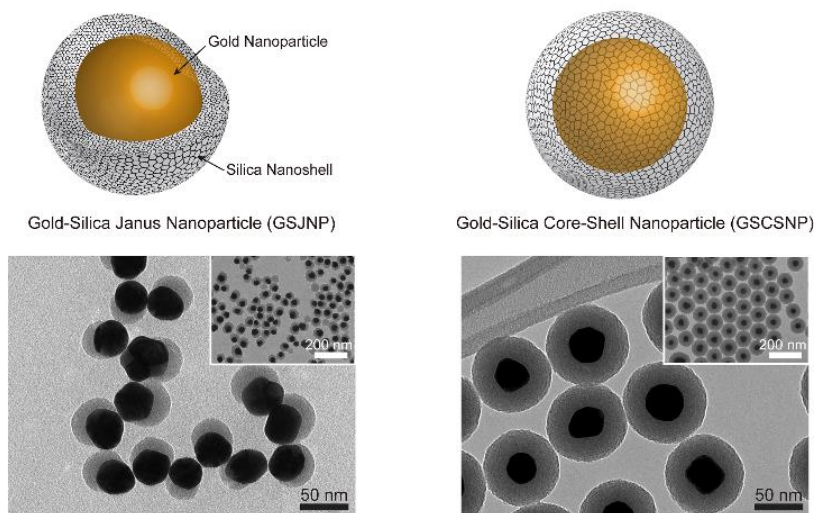


Figure 17 – TEM images of gold-silica janus nanoparticles and gold-silica core-shell nanoparticles

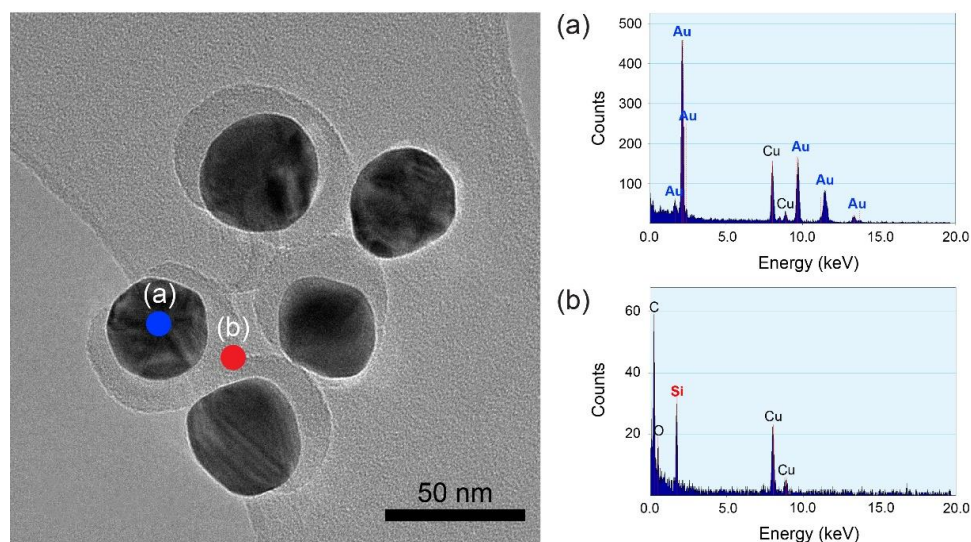


Figure 18 – TEM image of GSJNPs and EDS characterization corresponding to the two spots at (a) gold nanoparticle and (b) silica shell on holey carbon film coated copper grids.

UV-Vis spectroscopy and dynamic light scattering (DLS) was used to characterize the colloidal behavior of GSJNPs in DI water and in Dulbecco's Modified Eagle's Medium (DMEM) with 10% (v/v) of fetal bovine serum (FBS), a commonly used CCM. The absorption spectra of citrated AuNPs, GSJNPs, and GSCSNPs in DI water show the maximum peaks of each sample at 524, 526, and 532 nm respectively (Figure 19a). The slight red-shift in plasmon resonance may be attributed to the increase in the local refractive index around gold nanoparticles resulting from the formation of silica shells¹⁴⁰. The corresponding mean hydrodynamic sizes were 55, 126, and 65 nm for citrated AuNPs, GSCSNPs, and GSJNPs, respectively (Figure 19b and Figure 20).

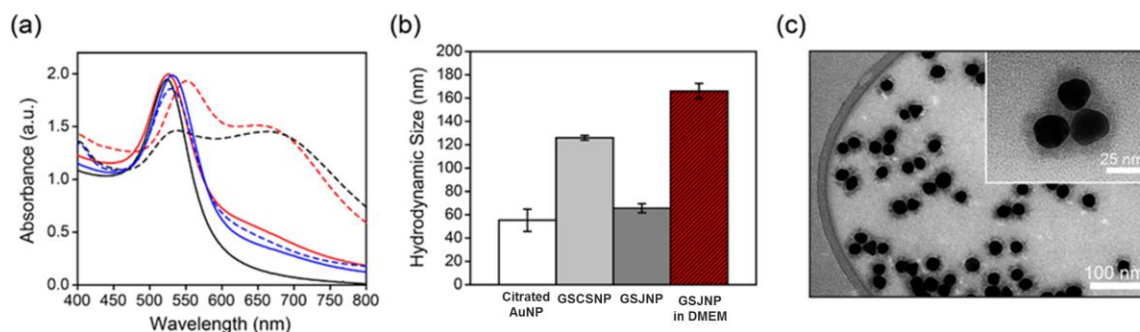


Figure 19 – (a) UV-Vis absorption spectra of citrated AuNPs (black line), GSCSNPs (blue line), GSJNPs (red line) in DI water (solid lines) and in DMEM with 10% FBS (dotted lines). (b) Hydrodynamic sizes of citrated AuNPs, GSCSNPs, GSJNPs in DI water, and GSJNP in DMEM with 10% FBS. (c) TEM micrograph of GSJNP in DMEM with 10% FBS.

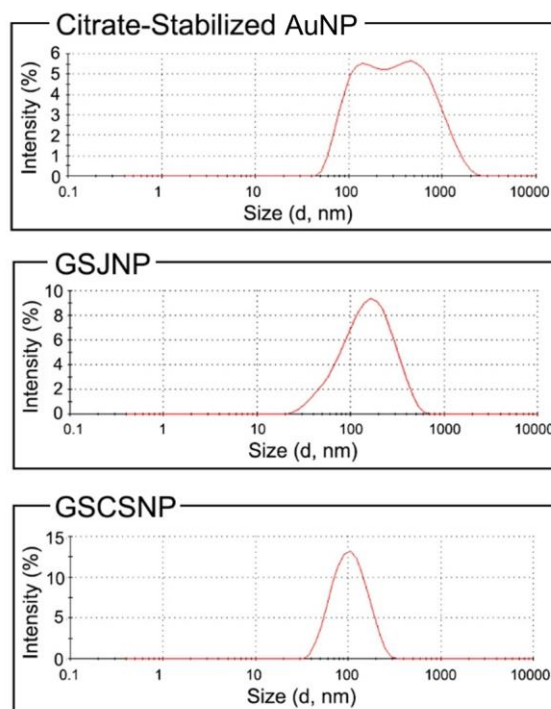


Figure 20 – DLS size distribution curves of citrate-stabilized AuNPs, GSJNPs, and GSCSNPs in DMEM with 10% FBS.

When the surrounding medium was changed from DI water to DMEM with 10% FBS, the color of aqueous GSCSNP solution was maintained in DMEM with 10% FBS,

and the resulting UV-Vis absorption spectrum had a single peak at 530 nm, which is similar to the one in DI water (Figure 19a). In contrast, the color of GSJNP and citrated AuNP solutions were rapidly changed from red to violet, indicating the formation of aggregates. AuNPs formed large aggregates as would be expected given the lack of silica protection. In contrast, the aggregates of GSJNPs were observed to maintain stable colloidal dispersibility (Figure 21) and the hydrodynamic diameter was measured to be 166 nm (*ca.* 2.5-fold larger than that of GSJNPs in DI water, Figure 19b). It was noteworthy that the UV-Vis absorption spectrum of resulting aggregates showed not only the red-shifted profile but also a new absorption band ranging from 600 to 700 nm of wavelength (Figure 19a). TEM observation clearly showed the resulting morphologies of GSJNPs controllably aggregated by the incubation in DMEM with 10% FBS (Figure 19c). The images showed some single GSJNPs, but mainly aggregates in which the gold surfaces of adjacent GSJNPs were in close proximity, confirming that the aggregation process was not random. This result implies that the partial silica shells guide the controlled aggregation of GSJNPs via interactions between the exposed gold surfaces, thereby enhancing their plasmonic coupling. Silica shells maintain their inertness and sufficient negative surface charge even if their surrounding medium is changed from DI water to DMEM with 10% FBS¹⁴¹. Overall, results suggest that GSJNPs spontaneously undergo a controlled aggregation in DMEM with 10% FBS, protected by the partial silica shells from unwanted further aggregation.

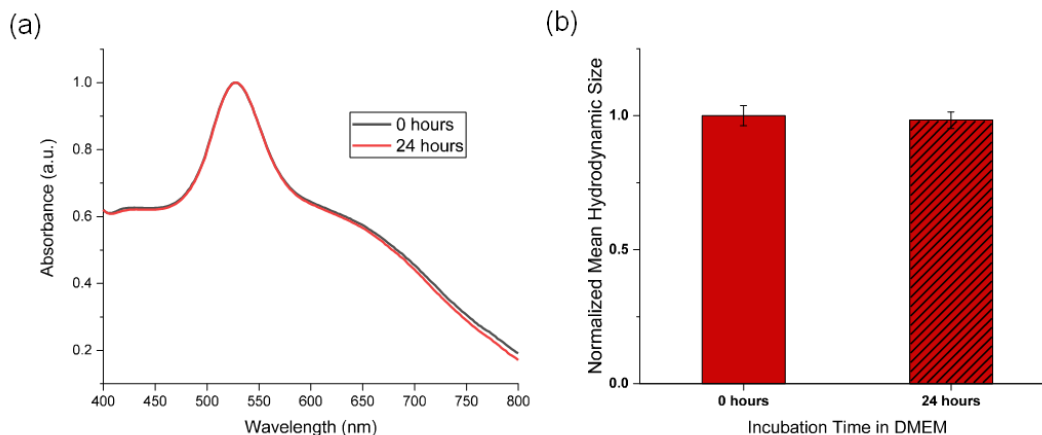


Figure 21 – Stability of GSJNP aggregates in DMEM characterized using (a) UV-Vis and (b) DLS.

To demonstrate the feasibility of PA imaging with GSJNPs, phantom experiments were performed with polytetrafluoroethylene (PTFE) tubes mimicking the blood or lymph vessels. GSJNPs were dispersed in DMEM with 10% FBS at an $OD = 4 \text{ cm}^{-1}$. GSCSNPs were also prepared under the same conditions as a control. PA images were acquired using an integrated ultrasound-photoacoustic imaging system (Vevo LAZR) operating with a 20 MHz ultrasound transducer (LZ-250) and 700 nm laser irradiation. As depicted in Figure 22a, the PA intensity of GSJNPs was significantly stronger than that of GSCSNPs at 700 nm excitation. The PA intensities, averaged over 100 frames, were measured to be 2.13 ± 0.06 for GSJNPs and 0.28 ± 0.02 for GSCSNPs, which was an almost eight-fold increase of PA intensity for GSJNPs (Figure 22a). Aggregation and plasmon coupling of GSJNPs, which were not present in GSCSNPs due to the isotropic silica shells, enabled the strong NIR absorption and caused the increase in PA intensity. Furthermore, multiwavelength PA imaging was performed to investigate the spectral variation of PA intensities in NIR region. This spectral pattern analysis is widely used in various applications, including the differentiation of atherosclerotic plaques, and selective detection of cancer¹⁴²⁻¹⁴⁴. PA

images were obtained to generate PA intensity spectra from 700 nm to 970 nm. GSJNPs maintained a high PA intensity from 700 nm to 790 nm, gradually decreasing for higher wavelengths. In contrast, GSCSNPs had a low PA intensity throughout the NIR region (Figure 22b).

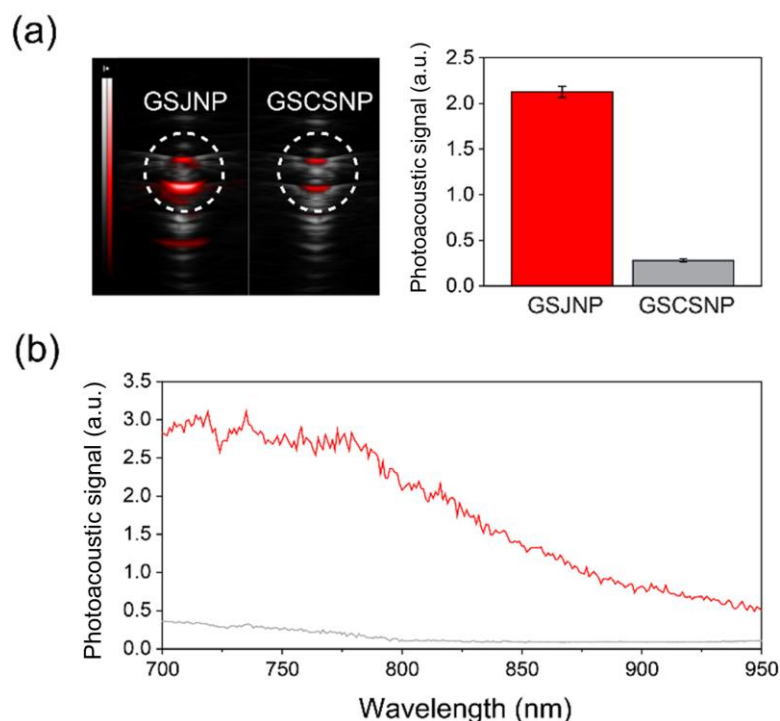


Figure 22 – Photoacoustic signal measurement using PTFE tubes for GSJNPs and GSCSNPs in DMEM with 10% FBS. (a) Combined PA images with ultrasound images (left) and averaged PA intensity at 700 nm excitation (right). (b) Multiwavelength PA signal measurements of GSJNP (red line) and GSCSNP (gray line).

To validate in vitro NIR imaging capabilities of GSJNPs, mouse monocytes-macrophages (J774A.1 macrophage cell line) and human breast cancer cells (MDA-MB-231 human breast adenocarcinoma cell line) were used as model cell lines. A tissue-mimicking phantom was created with dome-shaped gelatin inclusions containing GSJNP-loaded cells. To simulate optical and ultrasound scattering of biological tissues, the

gelatin inclusions were made by a mixture of gelatin (6 wt%) and silica gel particles (0.2 wt%) in DI water as described in a previous report¹³¹. Based upon PA imaging analysis of the gelatin inclusions, both cell lines exhibited very high PA intensities at 700 nm excitation, as shown in the PA images of each cell line (Figure 23) and the GSJNPs in cells generated a constant PA signal over more than 400 laser pulses, confirming photothermal stability under laser irradiation (Figure 24). Multiwavelength PA measurements also indicated strong NIR absorption (Figure 25). These results demonstrate the potential role of GSJNPs as a PA contrast agent for in vitro and in vivo biomedical applications, such as cancer diagnosis, therapy and immunology. In biomedical applications, distinguishing contrast agents' cellular and environment interactions is often a challenge. Heterogeneous self-assembly of commonly used AuNPs implies an uncertainty in the resulting absorption spectra upon these interactions. In many cases, a non-distinctive spectrum may be confused with that of endogenous absorbers such as blood or melanin. This hinders analytical spectral analysis methods and requires sophisticated, time-consuming imaging procedures. The controlled aggregation of GSJNPs provides a characteristic spectrum that could be resolved using the multiwavelength PA imaging, allowing simpler approaches with potential for more accurate diagnostic and therapeutic techniques.

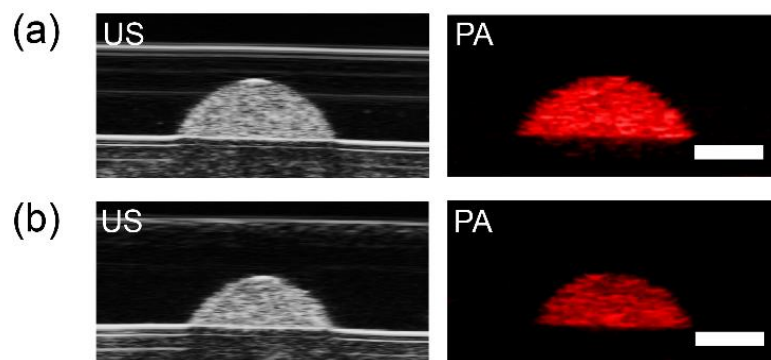


Figure 23 – Ultrasound and photoacoustic images (scale bar = 2 mm) of gelatin inclusions containing (a) macrophages and (b) human breast cancer cells incubated with GSJNPs.

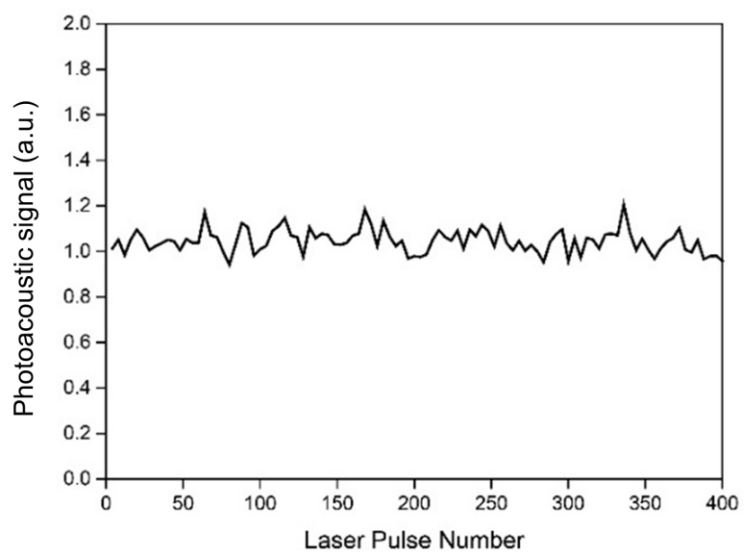


Figure 24 – Stability of PA signal for GSJNPs in macrophages under laser irradiation.

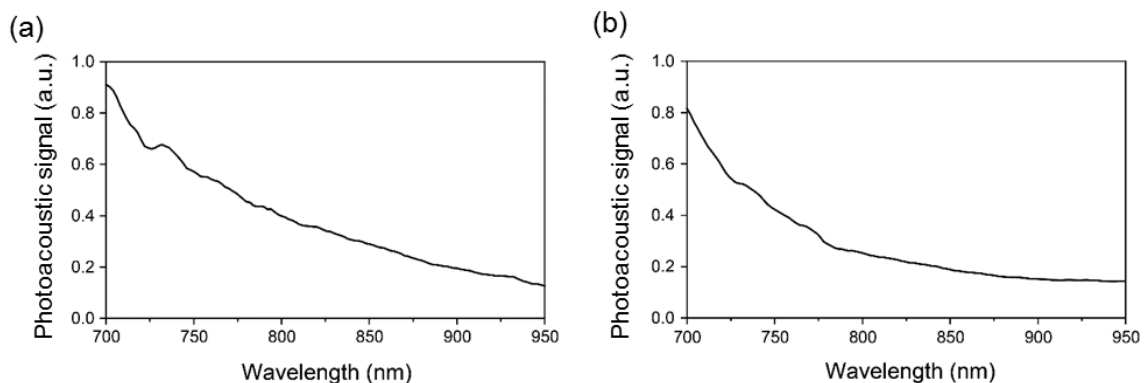


Figure 25 – Multiwavelength PA signal measurements of gelatin inclusions containing (a) macrophages and (b) human breast cancer cells incubated with GSJNPs.

Lack of cytotoxicity is an important factor for contrast agents to be used in vivo. The viability of human embryonic kidney cells 293T (HEK293T) was tested after incubation with GSJNPs for 24 hours using an MTT assay. As the concentration of GSJNPs was changed from 0.0625 to 2.0 of OD, the cell viability remained high, confirming their cytocompatibility (Figure 26).

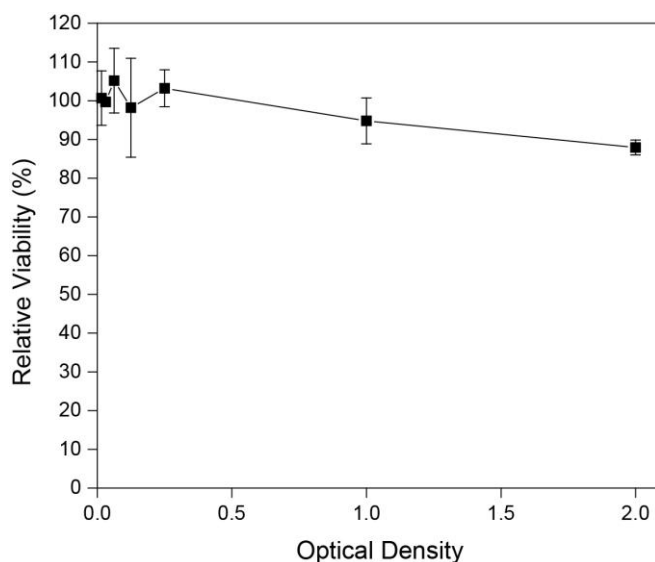


Figure 26 – Cytotoxicity analysis of GSJNPs with HEK 293T cells by MTT assay (y axis: relative % viability calculated by comparing cells treated with GSJNPs with untreated cells, x axis: final OD of GSJNPs at 532 nm).

The imaging capabilities of GSJNPs *in vivo* were characterized next. Upon subcutaneous injection into the mammary fat pad of healthy mice, GSJNPs immediately aggregated displaying a strong NIR photoacoustic signal. Conversely, GSCSNPs did not plasmon couple, but exhibited weak NIR signal due to their expected non-zero optical absorption (Figure 27a). This result is consistent with phantom studies and confirms the ability for contrast enhancement *in vivo*. Due to their inherent surface differences, particle drainage dynamics to regional lymph nodes may vary immediately after injection. However, after 24 hours, both particle types are expected to arrive to the inguinal lymph node, either via passive drainage or active cell transport¹⁴⁵⁻¹⁴⁷. However, due to plasmon coupling, the mouse injected with GSJNPs showed high PA contrast in the lymph node, while the mouse with GSCSNPs did not (region inside white dashed line, Figure 27b). Multiwavelength PA further confirmed the detection of GSJNPs. By using spectral unmixing methods³⁸, together with previously-obtained *in vitro* spectra, it was possible to separate the PA signals coming from oxygenated hemoglobin (HbO₂), deoxygenated hemoglobin (Hb), and GSJNP (Figure 27c). Additionally, it was further confirmed that the average PA spectrum in the lymph node area matched the absorption spectrum *in vitro* (Figure 27d). The spectrum from the lymph node with GSCSNPs predominantly showed characteristics of oxygenated and deoxygenated hemoglobin. The ability of GSJNPs to controllably aggregate and plasmon-couple enables NIR PA imaging at relevant depths. Furthermore, the likelihood of morphological deformation by laser irradiation may be lower for GSJNPs in contrast to other NIR-absorbing AuNPs such as gold nanorods¹⁴⁸, ensuring reproducible PA imaging. With additional surface modifications, GSJNP

aggregation could be triggered by different environmental cues, facilitating molecular imaging and tumor-targeted theranostic applications.

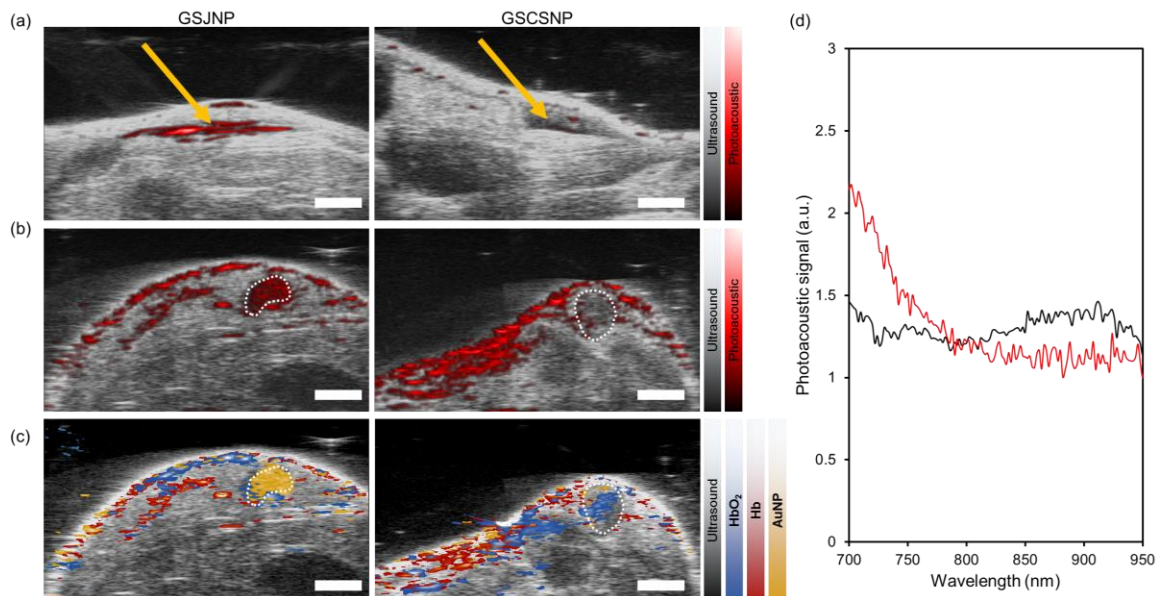


Figure 27 – Combined ultrasound and photoacoustic in vivo images ($\lambda = 700$ nm, scale bar = 2 mm) of mice injected with GSJNPs or GSCSNPs (left and right column, respectively) at (a) mammary fat pad subcutaneous injection site (yellow arrow) and (b) draining inguinal lymph node (white dashed line). (c) Multiwavelength PA imaging enables spectral unmixing of oxygenated hemoglobin (HbO₂, blue), deoxygenated hemoglobin (Hb, red), and nanoparticles (AuNP, yellow). (d) Multiwavelength PA spectra in the lymph node of each mouse, injected with GSJNPs (red line) and GSCSNPs (black line).

5.4 Conclusions

This chapter demonstrated the controlled aggregation of GSJNPs and its use as a contrast agent for photoacoustic imaging in vitro and in vivo. The interactions between the exposed gold surfaces of GSJNPs generated plasmon-coupled nanostructures with high PA intensity in the NIR. While other nanostructures are also capable of absorbing in the NIR region, a major advantage of GSJNPs is their responsiveness to environmental conditions.

For instance, it is feasible to design functionalized GSJNPs that would aggregate specifically in a tumor environment or a metastatic lymph node. Additionally, GSJNPs offer potential for orthogonal modifications of the gold and silica surfaces, and the loading of drugs and dyes in the anisotropic silica shell. The ability to control the aggregation of GSJNPs and their cytocompatibility will facilitate in vivo applications of various imaging techniques using photoacoustic imaging. The controlled aggregation of GSJNPs demonstrated herein thus represents a valuable addition to the chemical tool box to advance the development of theranostic agents that can potentially be applied to the assessment and treatment of sentinel lymph node metastasis.

CHAPTER 6. PRUSSIAN BLUE NANOCUBES – TOWARDS FULL-BODY MULTIFUNCTIONALITY

Across this dissertation, it is notable that the choice of contrast agent has important implications in the success of US/PA diagnostic techniques. Sometimes, versatility or safety are compromised in favor of diagnostic accuracy. Nevertheless, developing contrast agents and introducing new imaging modalities to clinic is already an arduous and long process. Nanomaterials have become increasingly used to augment diagnostic and therapeutic capabilities in numerous biomedical and clinically-relevant applications^{104, 149-152}. While extensive research has been performed to explore biocompatible nanostructures having optical and magnetic properties that are suitable for current diagnostic and therapeutic modalities, to date, designing multifunctional theranostic agents of appropriate size, shape, and surface characteristics remains a constant challenge. While no single agent is ideal for all applications and stages of patient care, access to safe, versatile nanomaterials could give clinicians the flexibility needed to design more comprehensive theranostic schemes. A contrast agent that is safe, economic, and versatile to be useful in various diagnostic and therapeutic procedures (i.e., multifunctional) may find an easier path into clinic than other less-versatile, less-safe agents.

Among many solid nanoparticles, Prussian blue is of particular interest due in part to its excellent biocompatibility. Prussian blue is approved by the U.S. Food and Drug Administration (FDA), under the brand name Radiogardase®, for the treatment of patients with known or suspected contamination of cesium and/or thallium. However, this clinical indication has nothing to do with Prussian blue's most defining characteristic.

Prussian blue's vibrant blue appearance stems from a very strong optical absorption of red light. Because photon absorption occurs in the tissue optical window (650 – 1300 nm)²⁹, several preclinical investigations have been performed to assess the feasibility of Prussian blue nanoparticles (PBNPs) as a contrast agent in photoacoustic imaging¹⁵³⁻¹⁵⁷ and to enhance heating in photothermal therapy¹⁵⁸⁻¹⁶⁰. In addition to its visible appearance, Prussian blue is more than 45% iron by mass, endowing it with magnetic properties that have been studied in MRI^{158, 160-161}. The intrinsic optical and magnetic properties of Prussian blue have also progressed to explorations in multimodal theranostics^{154-155, 158, 160}. However, PBNPs have not been developed and studied to their full potential. Particularly, conventional synthesis methods are prone to variability, resulting in PBNPs of different sizes and properties.

Nanoparticle size can be crucial for specific applications. For instance, size is an important factor to predict localization of intravenously-injected nanoparticles. Nanoparticles smaller than 5 nm in size rapidly undergo renal clearance upon intravenous administration⁹⁷. Nanoparticles between 50 – 100 nm are retained in the liver due to spacing of vascular fenestrations and endothelial gaps¹⁶². Nanoparticles between 200 – 500 nm are retained in the spleen according to the size of the interendothelial cell slits¹⁶². Large particles in the 2 – 5 μ m range have been shown to accumulate in the lungs¹⁶². Tumors can exhibit a range of fenestrations from 380 – 780 nm¹⁶³, which leads to their enhanced permeability and retention, and nanoparticles in the range of 30 – 100 nm in diameter have exhibited good penetration in a study involving a highly permeable tumor. However, in a poorly permeable human pancreatic adenocarcinoma, only nanoparticles smaller than 50 nm in diameter showed accumulation¹⁶². Based on these examples, smaller

particles can be useful when rapid clearance and enhanced permeation are required. However other applications, such as magnetic delivery of nanoparticle-labeled cells, may require larger constructs that exhibit a stronger response to external fields. Being able to tune the size of PBNPs enables a variety of applications and allows researchers to tune their nanoparticles to meet the particular needs of specific diagnostic and therapeutic schemes.

This chapter presents a facile seed-mediated growth method for the synthesis of Prussian blue nanoparticles. Unlike previous Prussian blue synthesis methods which involve the reduction of iron salts or iron complexes^{154, 158, 161, 164-165}, this method uses previously synthesized Fe₃O₄ nanoparticles as the iron source. The Fe₃O₄ nanoparticles supply magnetic iron species to ferrocyanide molecules, which assemble into Prussian blue nanocubes (PBNCs). Since this reaction occurs very quickly, the resulting PBNC size is directly related to the size of the Fe₃O₄ nanoparticle. Additionally, the potential of the developed PBNCs as multimodal, multifunctional agents is shown. The magnetic and optical properties of PBNCs proved useful for applications including MRI, photoacoustic imaging, and magnetic manipulation of PBNC-labeled cells.

6.1 Materials and Methods

6.1.1 Synthesis of SPION precursors

Dextran-coated SPIONs, 5 nm and 10 nm diameter, were purchased from Ocean NanoTech (San Diego, CA). Small SPIONs (3 nm diameter) were synthesized in-house. All chemicals, unless otherwise stated, were purchased from Sigma.

All glassware and stir bars were washed with aqua regia (3 parts hydrochloric acid (HCl): 1 part nitric acid (HNO₃)) prior to synthesis. A three-neck round bottom flask containing an egg-shaped stir bar was suspended in a silicon oil bath placed on a heated stir plate. The temperature of the oil bath was continuously monitored throughout the reaction. One neck was used as a gas inlet, and the second neck was connected to a condenser to keep the reaction under reflux. Prior to adding any reagents, the oil bath was heated to 80 °C for 30 minutes while oxygen was purged with argon or nitrogen gas. After initial heating, 200 ml of triethylene glycol (TEG) and 12.714 g of iron(III) acetylacetonate (Fe(acac)₃) were added to the flask. The solution of Fe(acac)₃ in TEG was heated to 140 °C for one hour under stirring. An additional 200 ml of TEG was added to collect any Fe(acac)₃ remaining on the sides of the flask. Once the reaction stabilized at 140 °C, temperature was increased to 200 °C. After an additional 2 hours, the reaction was cooled to room temperature overnight. Stirring and purging with argon or nitrogen gas continued while cooling. The total volume and milligrams of Fe were determined for PBNC synthesis. Small SPIONs were dextran-coated prior to PBNC synthesis. The SPIONs in TEG were diluted 10x in deionized ultra-filtered water (DIUF), dextran was added (10 mg per 1 mg of Fe) and the reaction was gently stirred overnight to coat

6.1.2 *Synthesis of PBNCs*

Prussian blue nanocubes (PBNCs) were synthesized using a seed-mediated method. Diameter of superparamagnetic iron oxide nanoparticles (SPIONs) precursors was altered to produce PBNCs with different edge lengths. Stock solutions of the reactant and catalyst for PBNC synthesis were prepared in advance. The catalyst was composed of 1.85% HCl in DIUF. The reactant was composed of 5% potassium hexacyanoferrate (II) trihydrate

($\text{K}_4\text{Fe}(\text{CN})_6 \cdot 3\text{H}_2\text{O}$) by mass. Under vigorous stirring, 60 mg of SPIONs were added to 150 ml of DIUF. The solution was briefly stirred before proceeding to ensure SPIONs were dispersed throughout the solution. Then, 7.5 ml of the reactant stock solution was added. The reaction was stirred for 1 minute, and 2.496 ml of the catalyst solution was added. The reaction was stirred for at least 1 hour. The solution became a deep blue color as the PBNCs formed. When necessary to stabilize PBNCs and minimize aggregation, 0.1 mg of citric acid per 0.5 mg of Fe precursor were added during the synthesis. This protocol was tested with SPIONs up to 10nm. Following synthesis, the UV-Vis absorbance spectrum of PBNCs was measured using a Synergy HT Microplate Reader (Biotek).

6.1.3 *Transmission electron microscopy*

Transmission electron microscopy (TEM) (Hitachi HT7700 TEM) was used to characterize the PBNCs, 5 nm diameter SPIONs, and 10 nm diameter SPIONs. Small SPIONs (3 nm) were imaged using a FEI Tecnai G2 F20 X-Twin TEM. Carbon-formvar grids were prepared by drop casting a small volume of particles and drying overnight. Prior to drop casting, samples were centrifuged at 300 RCF for 2 min, preserving the supernatant, to eliminate any overly large particles or aggregates. Then, the samples were centrifuged at 1,000 RCF (large PBNCs) or 12,000 RCF (small and medium PBNCs). The pellet was sonicated and resuspended in a 1:1 acetone/DIUF solution. Samples were washed at least twice and resuspended in water. A small volume was drop cast onto the grid and dried overnight. Size distribution of all particles was analyzed using ImageJ software.

6.1.4 SQUID Magnetometry

The magnetic properties of PBNCs and SPIONS were studied using a superconducting quantum interference device (SQUID) magnetometer (MPMS-5S, Quantum Design). Prior to measurements, samples were concentrated by centrifugation using a 50 kDA Millipore regenerated cellulose membrane filter (Fisher Scientific). The final concentrations were 8.7 mg/ml for PBNCs (20 nm), and 20 mg/ml for SPIONs (3 nm).

Each sample was scanned separately. Briefly, 100 μ l of the concentrated nanoparticle solution was added to a polycarbonate capsule (AGC3, Quantum Design). The capsule was sealed with non-magnetic tape and inserted in a non-magnetic straw to be held inside the magnetometer. SQUID is commonly used to scan solid powdered samples in gelatin capsules; however, polycarbonate capsules were used to prevent dissolution due to our liquid samples. A capsule with DI water was used to confirm no significant background magnetization. The temperature was set to 5 K, and the magnetic field was varied from 5 T to -5 T twice to obtain a hysteresis curve of the magnetic moment.

6.1.5 MRI relaxometry

MRI contrast properties were measured using a 3T MRI scanner (MAGNETOM Skyra 3T MRI, Siemens). A blank tube with DI water, and samples of PBNC at 0.1x, 0.25x, 0.5x and 1x concentrations were scanned to determine PBNC longitudinal and transverse relaxivities. The 1x concentration contained 0.25 mg/ml of PBNCs. Longitudinal relaxivity (R_1) was determined using a standard inversion-recovery-prepared turbo spin-echo (IR-TSE) sequence, and 25 inversion time (TR) values from 0.1 to 7 seconds while measuring the sample signal intensity. Data were fit to the relevant

mono-exponential signal model using a nonlinear least squares (NLS) method to calculate the individual exponential rise constant (i.e., T_1 relaxation time) of each tube. The longitudinal relaxivity R_1 is the inverse of the calculated T_1 relaxation time. Correspondingly, transverse relaxivity (R_2) was measured using a standard Carr-Purcell-Meiboom-Gill sequence (CPMG) with 32 time-to-echo (TE) values from 0.1 to 1.6 seconds. The individual exponential decay constant (i.e., T_2 relaxation time) of each tube was calculated with NLS method as before, and the inverse was taken to obtain the transverse relaxivities (R_2).

6.1.6 Photostability

To test photostability, PBNCs were irradiated using a 5-ns pulsed laser. A 1 mm diameter glass tube served as the sample holder and was filled with either PBNCs, PEGylated gold nanorods (PEG-AuNR), or silica-coated gold nanorods (SiO₂-AuNR), with absorption peaks between 680 and 700 nm. All samples had an optical density $OD = 1 \text{ cm}^{-1}$. The tube was irradiated using a 5-ns pulsed laser (Quanta-Ray Pro, Spectra-Physics K.K.) coupled to an OPO (PremiScan, GWU) tuned to 680 nm. The samples were exposed to 900 laser pulses at various fluences ranging from 5 to 28 mJ/cm^2 , with a 10 Hz pulse repetition frequency. The photoacoustic signal was measured using a 1 mm needle hydrophone with 4 dB bandwidth of 0.2-15 MHz (Precision Acoustics Ltd., Dorchester, UK) and amplified by an ultrasound receiver amplifier (5073PR, Olympus NDT Inc., Waltham, MA, USA) connected to a data acquisition oscilloscope card (CompuScope 12400, Gage Applied Technologies Inc., Lockport, IL, USA). For each fluence, and for each different sample, the tube was irradiated with 900 laser pulses and the PA signal was recorded.

The absorption spectrum stability was further studied by irradiating a 96-well plate containing samples of PBNCs or PEG-AuNR with 900 laser pulses of fluences from 3 to 20 mJ/cm². After the irradiation experiment, UV-Vis measurements were taken to analyze any spectrum variations due to laser exposure. Results were normalized based on absorbance before irradiation

6.1.7 Cell labeling

Macrophages (J774A.1, sourced from the ATCC) were seeded at 5,000 cells/cm² and grown in high-glucose Dulbecco's modified eagle medium (DMEM, ThermoFisher), supplemented with 5% penicillin/streptomycin (Pen-Strep, ThermoFisher) and 10% fetal bovine serum (FBS, ThermoFisher). Cells were labeled with PBNCs once they reached 80% confluency. Human epithelial breast cancer cells (MDA-MB-231) were cultured similarly using in DMEM/F-12 medium (ThermoFisher) with Pen-Strep and FBS. Human adipose-derived mesenchymal stem cells (MSC) (Lonza) were cultured similarly using low-glucose DMEM, Pen-Strep, and FBS (ThermoFisher).

PBNCs were UV-sterilized for 24 hours prior to cell incubation and dispersed in phenol red-free media. The added particle concentration was based on optical density (OD). PBNCs at OD = 2 cm⁻¹ were incubated with cells overnight. Cells were subsequently washed with phosphate buffered saline solution (PBS, ThermoFisher) three times to eliminate free nanoparticles. PBNC-labeled cells were passaged and collected for photoacoustic imaging and magnetic delivery experiments.

6.1.8 Cell phantom preparation and US/PA imaging

Cells were incubated with PBNCs for 24 hours and washed as described above. PBNC-labeled cells were imaged in a tissue-mimicking phantom to verify successful labeling and feasibility of photoacoustic imaging. The phantom base contained 6 w/v % gelatin and 0.2 w/v % silica. To prepare the inclusions, PBNC-labeled cells were suspended in an equal volume of 12 w/v % gelatin heated to 40 °C. A small drop (40 µl) of the cell/gelatin solution was pipetted onto the solidified gelatin background to form the dome-shaped imaging inclusions. US/PA images of the gelatin phantom were acquired for wavelengths between 680 and 970 nm at an imaging frame rate of 5 Hz.

6.1.9 Ultrasound and photoacoustic imaging

A Vevo LAZR (VisualSonics, Canada) imaging system, incorporating ultrasound and photoacoustic (US/PA) modalities was used for US/PA imaging experiments. US/PA images were acquired using 20 and 40 MHz (LZ250 and LZ550) center frequency, 256-element transducers. Laser irradiation was delivered by an optical fiber integrated into the transducer. The laser source was a Q-switched Nd:YAG laser, pulsing at 20 Hz with a 7-ns pulse duration.

6.1.10 Magnetic resonance imaging

A 7T preclinical MRI system (Bruker PharmaScan) was used to acquire in vivo images. The mouse was anesthetized and placed on a cylindrical holder to be inserted in the imaging coil. Variations of a *FLASH* imaging sequence were utilized to identify the PBNCs.

6.1.11 In vivo animal procedures

All animal procedures were approved by the Institutional Animal Care and Use Committee (IACUC) at the Georgia Institute of Technology. A female nude mouse (Nu/Nu, Charles River) was injected subcutaneously in the abdomen with two boli consisting of 50% Matrigel matrix (Corning) and PBS, or 50% Matrigel and 20-nm dextran-coated PBNCs, $OD = 40 \text{ cm}^{-1}$. MRI and US/PA images were acquired subsequently. Following imaging experiments the mice were euthanized by CO_2 asphyxiation.

For the metastatic mouse study, five-week old female nude mice (Nu/Nu, Charles River) were inoculated in the right caudal mammary fat pad with 2×10^6 human breast adenocarcinoma cells in 50% matrigel (MDA-MB231-Red-FLuc-GFP, PerkinElmer). When the tumor reached 10 mm in diameter, two 100- μl subcutaneous injections of 200-nm dextran-coated PBNCs, $OD = 40 \text{ cm}^{-1}$, were performed: one peritumorally (right side) and one on the left caudal mammary fat pad (healthy side). Particles were allowed to drain for 24 hours prior to MRI and US/PA imaging. Following imaging experiments the mice were euthanized by CO_2 asphyxiation.

6.1.12 Magnetic Delivery and US/PA imaging

Magnetic trapping experiments were set up by running a 0.062" inner diameter x 0.095" outer diameter, clear silicone tube (HelixMark®) through a 10×10×10 cm clear plastic box. Two ring neodymium magnets (NR0082-45NM, CMS Magnetics, Garland, TX) were fixed at opposite ends of the box to apply a magnetic field along the tube and initially magnetize the particles. The tube passed through the center of each ring magnet.

Several small neodymium brick magnets (N42, K&J Magnetics, Inc., Pipersville, PA) were fixed below the center of the tube to produce a gradient for trapping. Cells labeled with 20-nm PBNCs, concentrated at 5,000 cells/ml, were circulated through the tube at a flow rate of 0.5 ml/min. US/PA images were collected along the length of the tube using $\lambda = 700$ nm by connecting a 20 MHz (LZ250) transducer to a 3D translation motor.

6.2 Size control

To demonstrate the size control of the synthesized PBNCs, 3, 5, and 10 nm diameter Fe_3O_4 nanoparticles were used as precursors to produce PBNCs measuring 20, 40, and 150 nm edge length, respectively. Indeed, TEM images show that PBNC size varied depending on the SPION precursor size (Figure 28). PBNCs were well dispersed in all cases (Figure 28a-c). Small PBNCs with approximately 20 nm edge length resulted from 3 nm diameter SPION precursors. Medium (40 nm edge length) PBNCs resulted from 5 nm diameter SPION precursors, and large (170 nm edge length) PBNCs resulted from 10 nm SPIONs. Thus, the size of resulting PBNCs was dependent on the diameter of SPION precursors (Figure 28g). All sample sizes approximated a single-population normal distribution (Figure 29). The mean sizes were 3.09 ± 1.04 nm, 6.38 ± 0.941 nm, and $11.02 \text{ nm} \pm 1.19$ nm for the SPION precursors, and 22.61 ± 6.93 nm, 38.48 ± 7.12 nm, and 171.36 ± 36.40 nm for the resulting PBNCs, respectively.

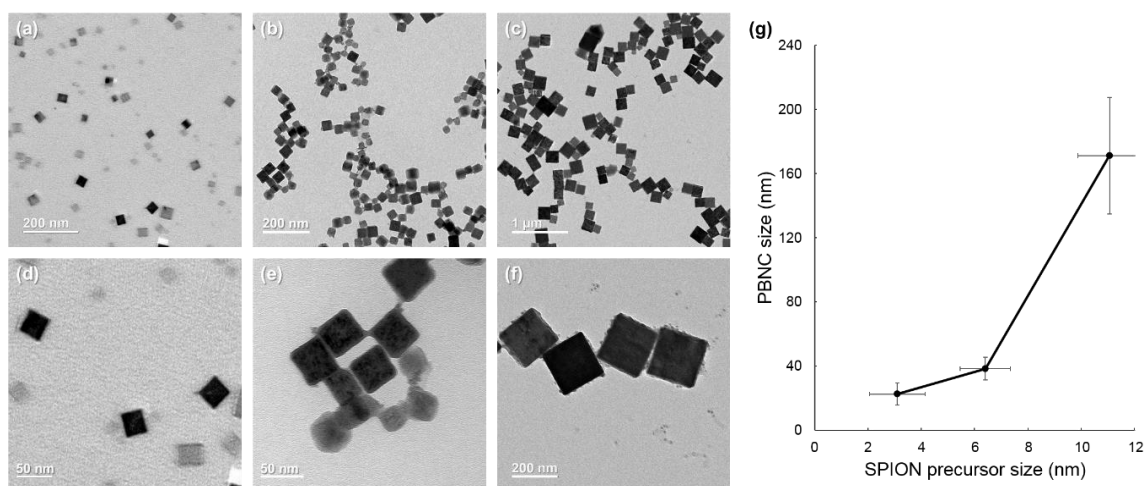


Figure 28 – TEM images of size-controlled PBNCs. (a) 20-nm PBNCs synthesized from 3-nm SPION precursors. (b) 40-nm PBNCs synthesized from 5-nm SPION precursors. (c) 150-nm PBNCs synthesized from 10-nm SPION precursors. (d-f) Images at increased magnification for 20-nm, 40-nm, and 150-nm PBNCs, respectively. (g) Scatter plot showing relationship between SPION precursors and resulting PBNC size.

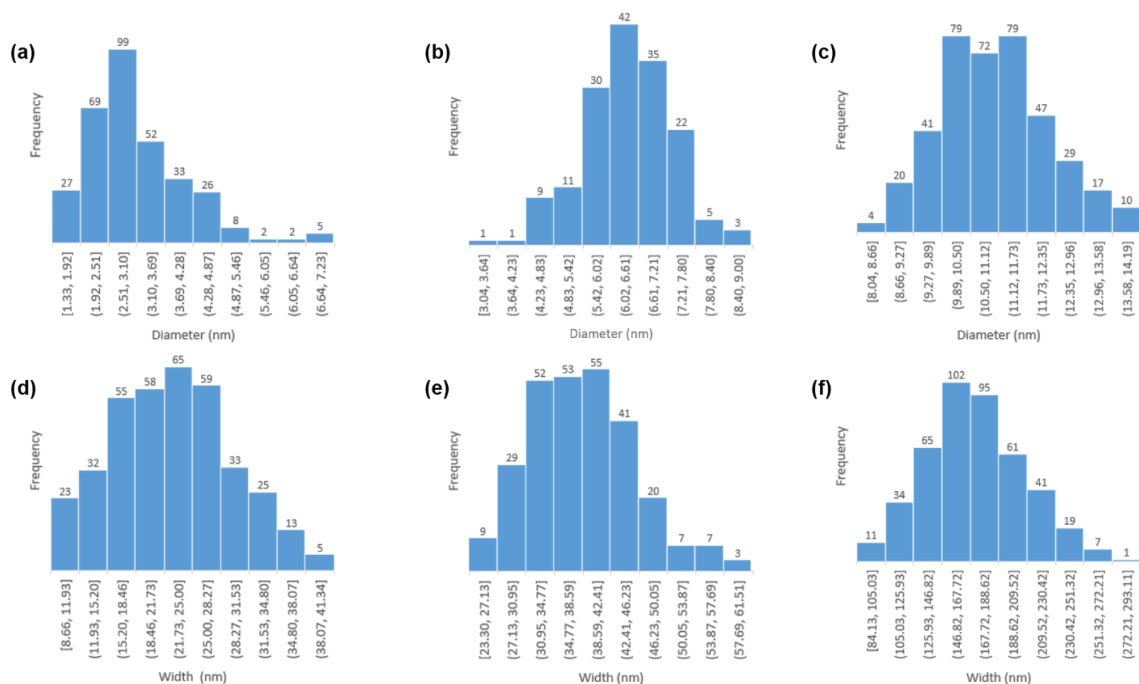


Figure 29 – Analysis of particle size distribution. (a-c) Size distribution of SPIONs with expected diameters of approximately 3 nm, 5 nm, and 10 nm, respectively. (d-f) Size distribution of resulting PBNCs with expected width of approximately 20 nm, 40 nm, and 150 nm, respectively.

The size standard deviation of each population was divided by its respective mean to obtain the particle size coefficient of variation. Results suggest that polydispersity of the precursor had an effect in the size distribution of resulting PBNCs. Due to challenges of size-separating extremely small SPIONs synthesized in house, a wider range of particle diameters was present in the 3-nm SPION sample compared to the 5-nm and 10-nm SPIONs. The 3 nm SPIONs were more polydisperse based on coefficient of variation, and hence led to more polydisperse 20-nm PBNCs (Figure 30). This further demonstrates the ability for size control of PBNCs.

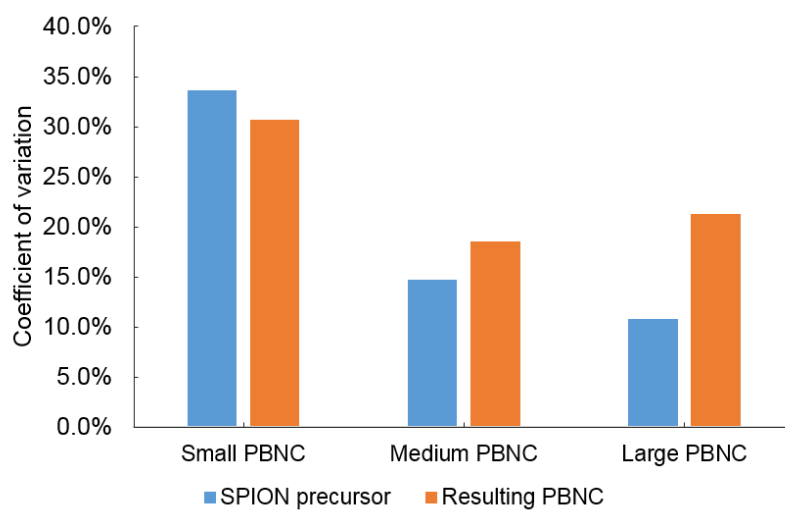


Figure 30 – Analysis of particle size coefficient of variation. A wider size distribution of SPION precursors causes higher deviation in the resulting PBNCs.

Energy-dispersive X-ray spectroscopy (EDXS) images showed an even distribution of iron, oxygen, potassium and nitrogen. Thus, the nanostructure is not a surface coating of SPIONs. At most, the PBNCs may be growing around multiple SPIONs in a structured homogeneous manner, but results suggest that structural ‘holes’ of Prussian blue are filled with SPIONs.

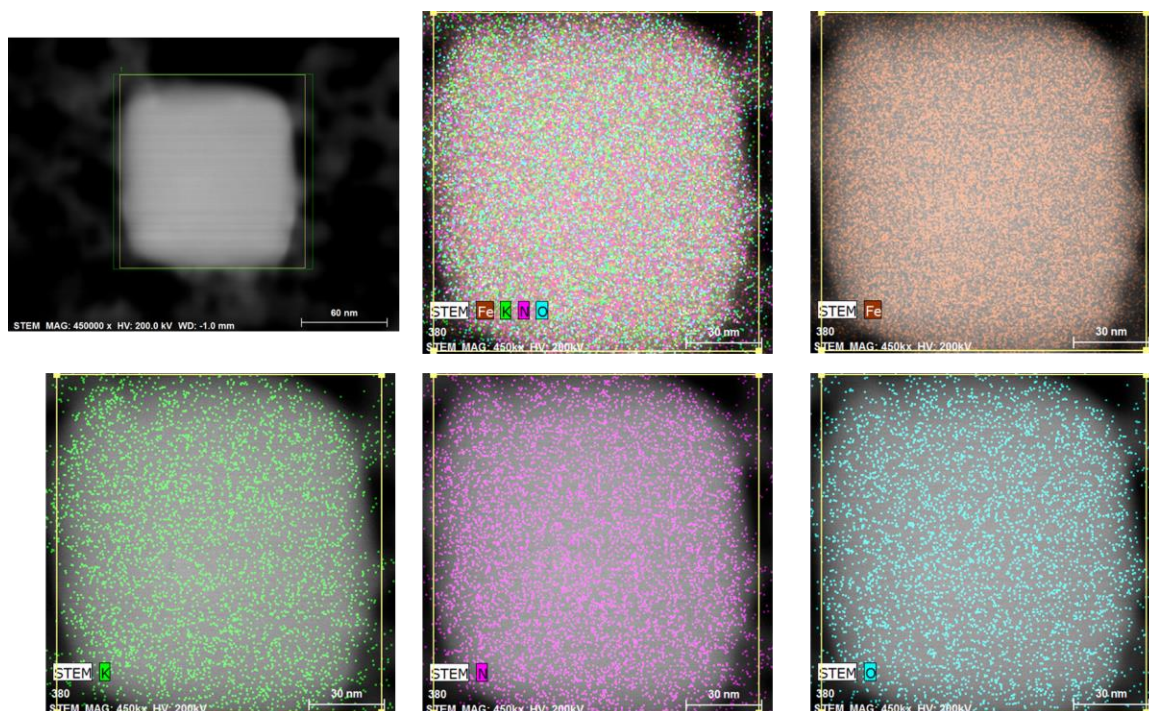


Figure 31 – Energy-dispersive X-ray spectroscopy of a PBNCs shows homogenous distribution of elements across the nanocube.

The magnetic and optical properties of PBNCs were characterized, and various applications were tested. For proof-of-concept, 20-nm PBNCs were used in all sections below.

6.3 Magnetic and optical properties

The magnetism of small 20-nm PBNCs and their 3-nm SPION precursors was analyzed using a superconducting quantum interference device (SQUID) as shown in Figure 32a. PBNCs exhibited superparamagnetism with a magnetic saturation of 104.0 emu/g (nanoparticle mass) or 228.6 emu/g (iron mass). SPIONs exhibited a magnetic saturation of 20.5 emu/g (nanoparticle mass) or 28.3 emu/g (iron mass). This corresponds

to a 5-fold and 8-fold increase in magnetization, when comparing based on nanoparticle mass and iron mass, respectively.

These values also exceed the magnetic saturation of 66 emu/g reported for 20 nm SPIONs¹⁶⁶. More importantly, previous studies showing modification of magnetite nanoparticles usually imply a reduction of their magnetization, compared to pure SPIONs^{158, 167-170}. This further suggests that the presented method is not a surface modification of the SPION precursors, but a rearrangement into a new nanoparticle promoting higher magnetism.

Superparamagnetism of nanomaterials is dependent on their size, shape, and crystal structure.¹⁷¹⁻¹⁷² While magnetization increases with particle size, there is a size limit below which particles remain superparamagnetic (i.e. superparamagnetic limit). For Fe₃O₄, it has been reported that particles exhibit superparamagnetism when below 20 nm.¹⁷²⁻¹⁷⁴ The results presented in this study show that the superparamagnetic limit of PBNCs is at least as high as that of Fe₃O₄ and may be limited by the precursor size rather than PBNC size. This feature can be valuable whenever larger magnetization and/or particle sizes are needed, while preserving superparamagnetic properties.

In addition to having higher magnetic susceptibility than the clinically used SPION counterparts, PBNCs also had a high optical absorption with a peak at 680 nm (Figure 32b), which is within the near-infrared (NIR) optical window where tissue allows deepest light penetration. These two properties pose the developed PBNCs as attractive multimodal, multifunctional agents.

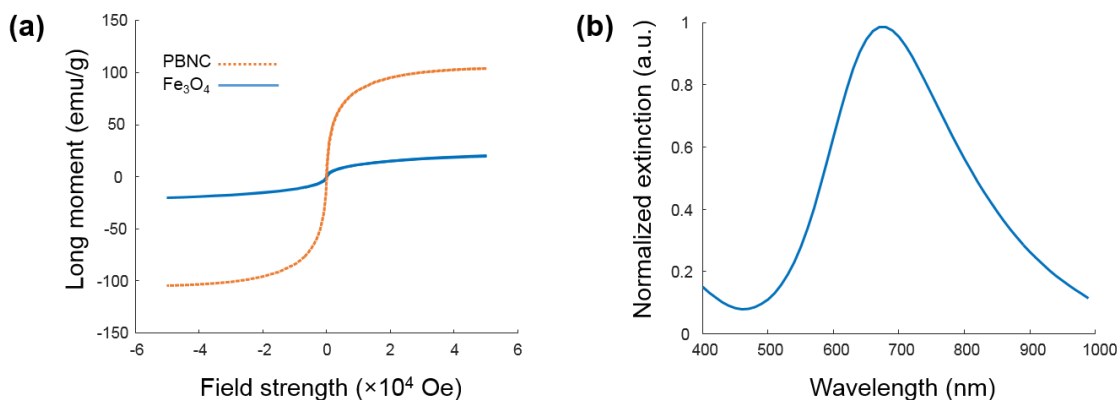


Figure 32 – Magnetic and optical properties of PBNCs. (a) Magnetic moment curves show a 5-fold increase in magnetization for PBNCs compared to Fe_3O_4 based on nanoparticle mass. (b) UV-Vis spectrometry shows PBNCs' NIR absorbance peak at 680 nm.

6.4 Magnetic resonance imaging

Relaxometry studies were performed to test PBNCs' feasibility as MRI contrast agents. Using a 3 T clinical MRI scanner (MAGNETOM Skyra 3T MRI, Siemens), a standard inversion-recovery-prepared turbo spin-echo (IR-TSE) sequence was performed to measure the longitudinal relaxation (T_1) and a standard Carr-Purcell-Meiboom-Gill sequence (CPMG) to measure transverse relaxation (T_2). By plotting the relaxivities versus nanoparticle concentration, and using linear regression, the best fit line was calculated, and the slope was extracted as the molar relaxivity (Figure 33).

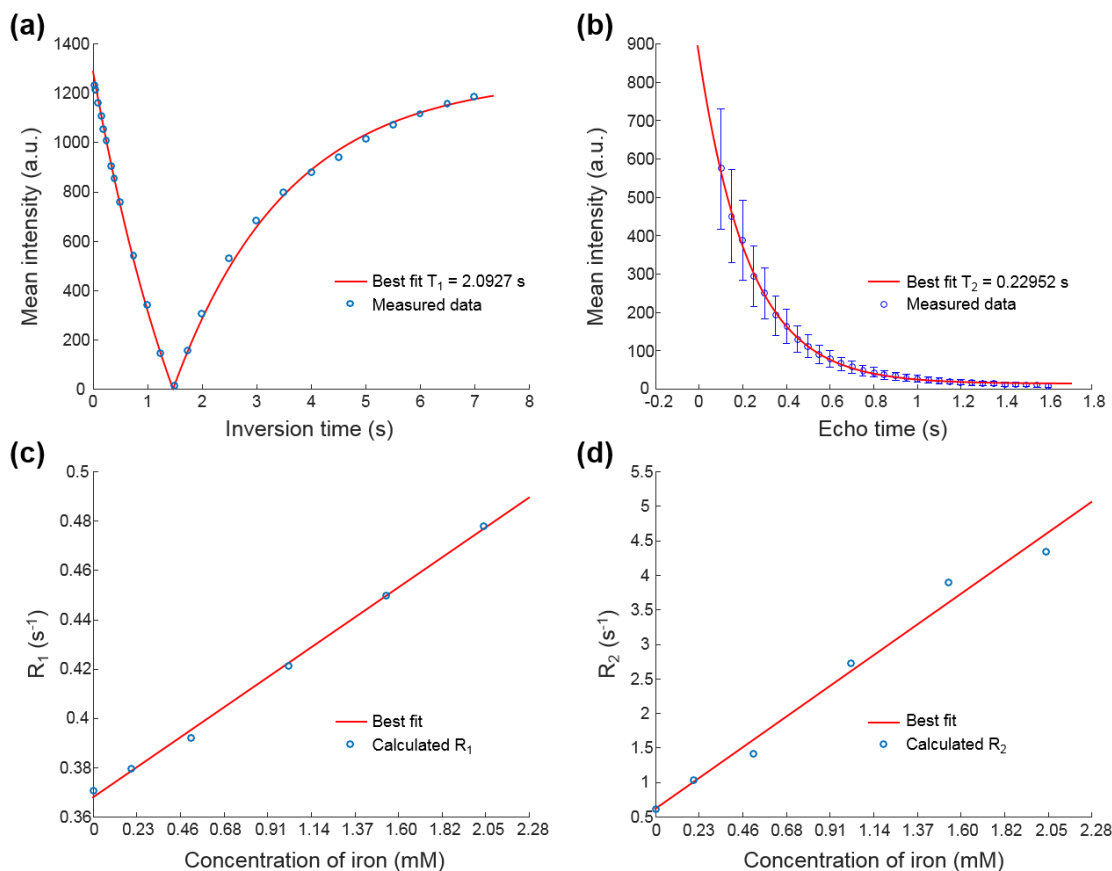


Figure 33 – Relaxometry studies to measure (a) T₁ relaxation and (b) T₂ relaxation of PBNCs at 0.25 mg/ml. Relaxivity plots with respect to different iron concentrations were used to calculate (c) longitudinal and (d) transverse relaxations.

Results of molar relaxivity studies are shown in Table 1. The obtained values exceed those reported using conventional PBNC synthesis methods under 1.5 T and 7 T field strengths¹⁷⁵. In addition to the different field strength, this could be attributed to water exchange-related differences affecting the relaxivity and fluctuations in the local magnetic field, known as inner sphere and outer sphere effects¹⁷⁶⁻¹⁷⁹.

Table 1 – Longitudinal and transverse molar relaxivity of PBNCs

	Longitudinal relaxivity r_1 (mM ⁻¹ s ⁻¹)	Transverse relaxivity r_2 (mM ⁻¹ s ⁻¹)
Per iron mass	0.0535	1.948
Per Prussian blue mass	0.3752	13.656

While other commercial MRI agents offer better molar relaxivity¹⁸⁰⁻¹⁸³, Shokouhimehr et al.¹⁷⁵ have correctly pointed that this can be overcome by using higher doses due to the low toxicity of Prussian blue. Indeed, the recommended daily oral dose for Radiogardase® in adults is 9 grams up to 20 grams, corresponding to 10.5 up to 23.3 mmol, with no overdose described. While a recommended dosage has not been established for IV use of Prussian blue, it could potentially be higher than those of commercial agents, such as gadolinium-based Gadavist® (100 µmol/kg, $r_1 = 5.0$ mM⁻¹s⁻¹, $r_2 = 7.1$ mM⁻¹s⁻¹) and SPION-based Sinerem®/Combidx® (45 µmol Fe/kg, $r_1 = 6.58$ mM⁻¹s⁻¹, $r_2 = 127.8$ mM⁻¹s⁻¹).

6.5 Photoacoustic imaging

While there are various reports on photoacoustic applications of PBNCs, their photothermal stability under pulsed laser irradiation has not been fully characterized. The stability of PBNCs was tested using various pulsed laser energies below and above American National Standards Institute (ANSI) safety limits¹⁸⁴. For each fluence, and for

each different sample, the tube was irradiated with 900 laser pulses. The recorded PA signals during 26 mJ/cm^2 laser irradiation are shown on Figure 34.

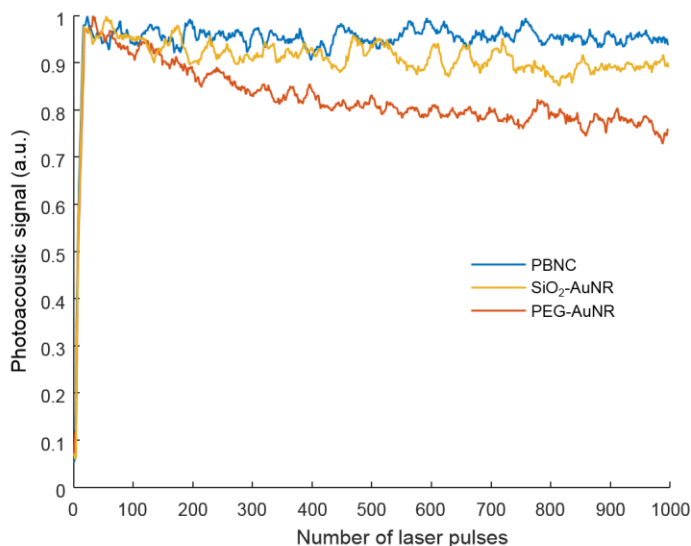


Figure 34 – PA signal during laser irradiation at 26 mJ/cm^2 shows stable signal generation of PBNCs. Progressive degradation after repeated laser pulses was seen for PEG-AuNR and SiO₂-AuNR

Unlike the more commonly used gold nanorods (degraded at $8.5 \text{ mJ}\cdot\text{cm}^{-2}$) and silica-coated gold nanorods (degraded at $13 \text{ mJ}\cdot\text{cm}^{-2}$), no degradation in the PA signal was observed up to $28 \text{ mJ}\cdot\text{cm}^{-2}$ (Figure 35a). Within this range, photoacoustic signal from PBNCs scaled linearly with fluence, demonstrating enhanced robustness as opposed to gold nanorods, which showed substantial photodegradation with all fluences greater than $5 \text{ mJ}\cdot\text{cm}^{-2}$ (Figure 35a,c). Furthermore, the absorbance spectrum of PBNCs also remained stable after irradiation with 900 laser pulses up to $20 \text{ mJ}\cdot\text{cm}^{-2}$ (Figure 35b).

In addition to benefits of magnetism and biocompatibility, the isotropic, non-plasmonic nature of PBNCs means they are less prone to degradation than anisotropic plasmonic particles, such as nanorods. For imaging in the NIR, PBNCs would outperform

many commonly used contrast agents including nanoparticles and dyes. PBNCs remain stable during repeated laser irradiation, enabling longer term imaging and therapeutic applications. This, together with their high molar absorption in the NIR¹⁸⁵, demonstrates PBNCs' suitability as photoacoustic agents.

In vitro PA phantom experiments were performed to further assess whether the synthesis method had any effect compared to previously shown schemes. PBNCs were used to label cancer cells and were imaged in a tissue-mimicking gelatin phantom. Inclusions of 20-nm PBNCs in deionized ultra-filtered water (DIUF) or cell culture media were also included to evaluate differences in PA signal upon cellular uptake.

PBNCs in DIUF did not produce any ultrasound (US) contrast because of their small particle size. The same sample generated a strong PA signal; however, because the particles remained homogeneously distributed in water, the signal was largely confined to the edges of the inclusion (Figure 35d_i). Cell culture media caused local agglomerations of PBNCs, making the particles more visible in ultrasound images compared to the samples in DIUF, because larger particle aggregates produced detectable ultrasound scattering. These localized agglomerations also introduced inhomogeneities that allowed PA signal to be more visible throughout the inclusion rather than limited to the edges (Figure 35d_{ii}).

Cancer cells labeled with 20-nm PBNCs were detectable with both ultrasound and PA imaging (Figure 35d_{iii}). PA signal appeared throughout the inclusion because cell uptake further increased local particle agglomeration. Mesenchymal stem cells were also successfully labeled by PBNCs, generating comparable images (Figure 35d_{iv}). The

photoacoustic spectra of the labeled cells (Figure 35e) matched the expected result based on the UV-vis spectra of PBNCs in DI water.

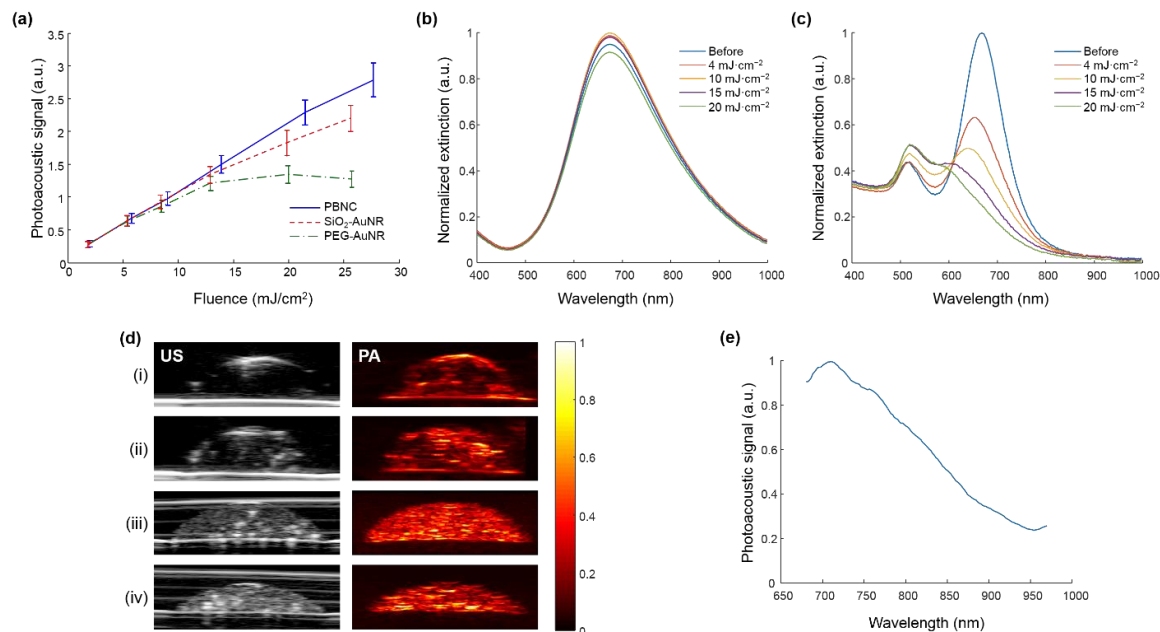


Figure 35 – Photothermal stability and photoacoustic imaging of PBNCs. (a) Photoacoustic signal from PBNCs, PEGylated gold nanorods (PEG-AuNR) and silica-coated gold nanorods (SiO₂-AuNR) at different fluences. PBNCs remained stable and conserve linearity with fluence when exposed to 900 laser pulses beyond 25 mJ·cm⁻². AuNR showed degradation beyond 5 mJ·cm⁻² (b) The absorbance spectrum of PBNCs remained stable after 900 laser pulses up to 20 mJ·cm⁻². (c) Gold nanorods' spectra showed degradation for all energies between 4 and 20 mJ·cm⁻². (d) Ultrasound (US, gray scale) and photoacoustic (PA, color map) imaging of 20-nm PBNCs in (i) DIUF, (ii) cell culture media, (iii) PBNC-labeled cancer cells, and (iv) PBNC-labeled mesenchymal stem cells. (e) Photoacoustic spectrum of cancer cells labeled with 20-nm PBNCs.

Imaging and cell labeling experiments confirmed PBNCs' performance as stable photoacoustic contrast agents when using this synthesis method. In addition, PBNC absorption was not affected by cell uptake, as indicated by the measured PA spectra.

6.6 In vivo imaging⁵

Two in vivo imaging experiments were performed to validate the feasibility of PBNCs. First, a bolus of 20-nm PBNCs in Matrigel was injected subcutaneously in the mouse abdomen. A control bolus was injected containing PBS in Matrigel.

US/PA imaging of the injected area showed high contrast on the PBNC-loaded bolus and low signal on the control bolus (Figure 36a). The absorption spectra confirmed presence of PBNC in bolus 1, and blood in bolus 2. The signal of PBNC bolus at 700 nm was approximately 4.5 times fold higher than the control bolus. Figure 36b shows normalized spectra for ease of visualization. High skin PA signals were also present, indicating the need for multiwavelength spectroscopic analysis to be able to distinguish PBNCs from background contrast.

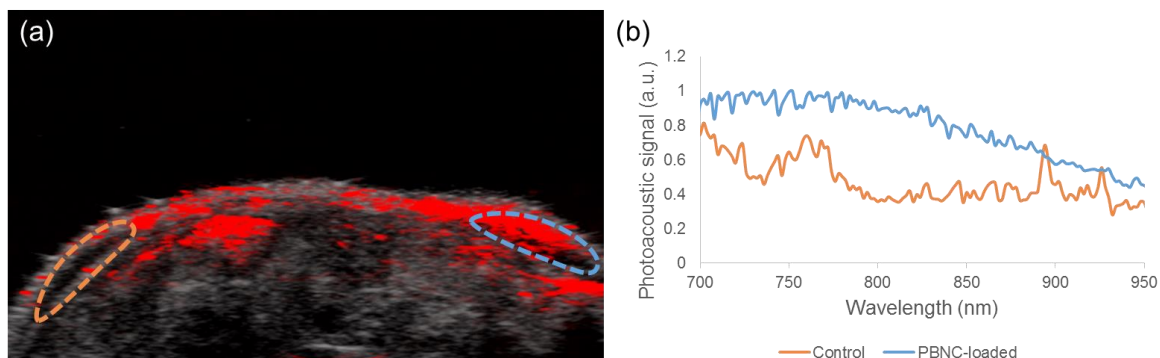


Figure 36 – (a) Photoacoustic images of axial cross section of a mouse abdomen at 700 nm following subcutaneous injection of PBNC in Matrigel (blue contour) and PBS in Matrigel (orange contour). (b) Corresponding normalized absorption spectra on each injection bolus.

⁵ In vivo imaging studies were performed in collaboration with Kelsey Kubelick from the Ultrasound Imaging and Therapeutics Research Laboratory at Georgia Tech.

Following US/PA, MRI was performed. A *Flash* sequence with repetition time $TR = 500$ ms and echo times TE 3.3, 10 and 15 ms was performed to assess variations in relaxation times due to PBNCs. As TE increases, the weight on $T2^*$ contrast increases. While the PBNC bolus gets darker, the PBS (blank) bolus remains clear. In this experiment, any single TE was sufficient to observe contrast from PBNCs due to their effect on $T2^*$ relaxation. In cases with lower agent concentration, or when the tissue is dark, the series of echos would help assess a rate of decay that could indicate presence of PBNC.

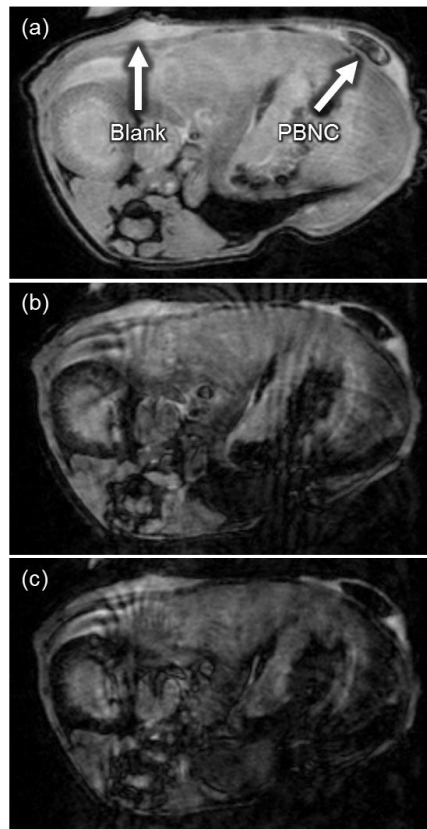


Figure 37 – In vivo MRI imaging of axial cross section of a mouse abdomen injected with 50% matrigel mixed with PBS (Blank) or Prussian blue nanocubes (PBNC) as indicated by the white arrows. A Flash sequence was used with $TR = 500$ ms and TE of (a) 3.3 ms, (b) 10 ms, and (c) 15 ms.

The second in vivo study involved a breast tumor bearing mouse, such as the model used in CHAPTER 2. The mouse had two identical subcutaneous injections in two sites. First, peritumorally for sentinel lymph node imaging, and then on the ‘healthy’ side of the mammary fat pad. Thus, accumulation after drainage to both inguinal lymph nodes could be assessed. In this experiment, 200-nm PBNCs were used to maximize US/PA and MRI contrast. After 24 hours, US/PA showed negligible accumulation in the metastatic sentinel lymph node (Figure 38a). Conversely, the left-side inguinal lymph node showed considerable accumulation of PBNCs (Figure 38b). The absorption spectra confirmed that the signal from the metastatic lymph node was predominantly from blood, while at the healthy node the signal was predominantly PBNCs (Figure 38c). This result resembles those presented in CHAPTER 2, indicating that metastasis affects the way nanoparticles accumulate in the sentinel lymph node.

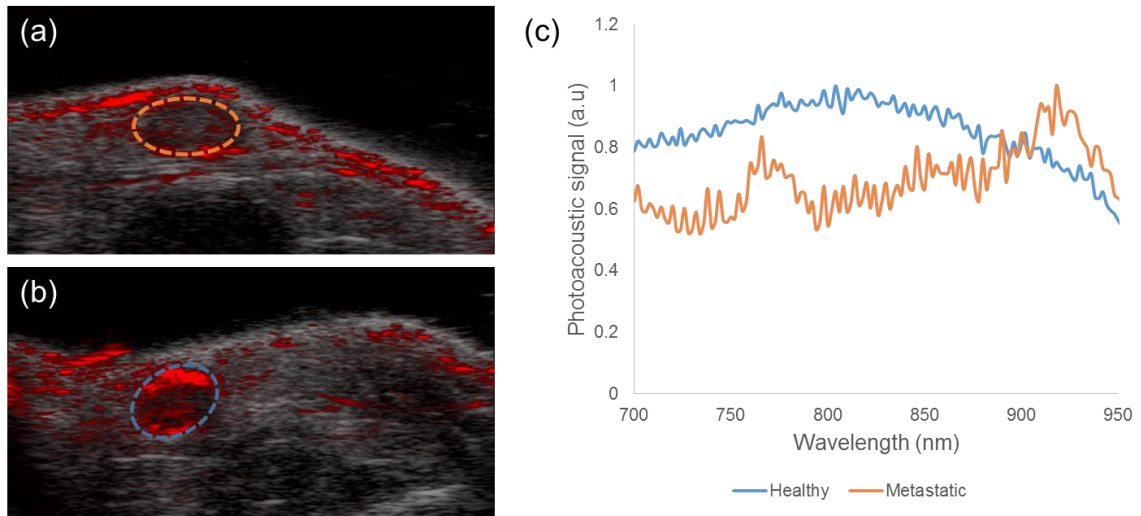


Figure 38 – Photoacoustic images of axial cross section at 700 nm, 24 hours after subcutaneous injections of 200-nm PBNCs. (a) Metastatic sentinel lymph node does not show significant accumulation of PBNCs while (b) the lymph node on the opposite healthy side shows high PBNC signal. (c) Normalized spectra confirm the predominant photoabsorbers are blood for the metastatic lymph node, and PBNC for the healthy lymph node.

The same mouse underwent MRI imaging subsequently. Figure 39 displays a coronal cross section showing both inguinal lymph nodes. The T2* effect of PBNCs is noticed in the healthy lymph node having a darker intensity than the metastatic sentinel node, due to increase accumulation of PBNCs in the healthy node.

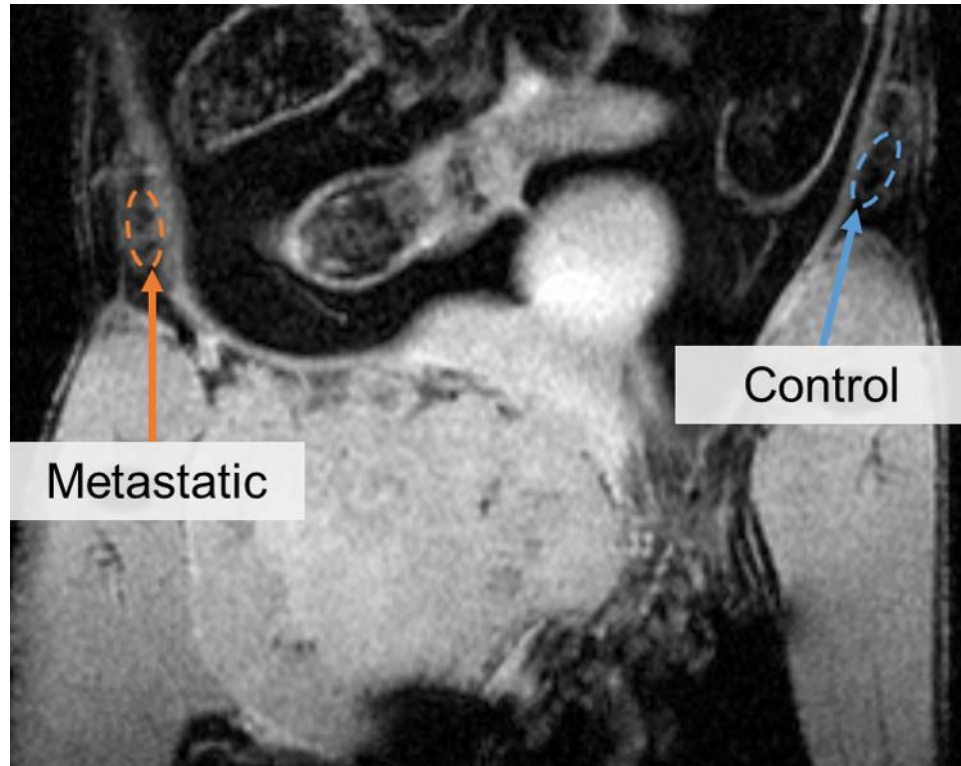


Figure 39 –MRI of coronal cross section of a tumor-bearing mouse 24 hours after subcutaneous injections of 200-nm PBNCs. The metastatic lymph node (orange contour) shows a brighter intensity than the healthy inguinal node (blue contour). A Flash sequence was used with TR = 400 ms, TE 3.9 ms, and flip angle of 30°.

The results suggest that PBNCs could be used in the assessment of sentinel lymph node metastasis. However, these preliminary findings must be taken carefully. First, appropriate number of animals and control groups must be analyzed to determine the feasibility of a US/PA/MRI/PBNC platform for SLN metastasis diagnosis. While spectroscopic PA imaging protocols have been clearly established, MRI sequences are yet

to be optimized for detection of PBNCs. If future studies prove successful, PBNCs could pose an excellent alternative to gold nanoparticles on the route to clinical translation.

6.7 Additional applications in oncology: Image-guided magnetic trapping⁶

Due to the superparamagnetism of PBNCs, PBNC-labeled cells can be manipulated using external magnetic fields (Figure 40a). The multifunctional utility of the PBNCs was demonstrated using a mock cell screening apparatus. Cells labeled with 20-nm PBNCs were circulated through a silicone tube with a magnetic trap. Two ring magnets produced a homogeneous field to initially magnetize the labeled cells, as previously shown⁶⁶. A bar magnet on the side of the tube applied a gradient to trap cells. Ultrasound and photoacoustic images were acquired along the length of the tube and overlaid to show where cells collected (Figure 40b insert). The US/PA signals of the tube were represented by gray scale and red scale, respectively. A spike in the PA signal was confined to the magnet location and corresponded to a 5-fold increase in the PA signal (Figure 40b).

By using an external magnetic field, PBNCs can be directed to a desired location for diagnostic and therapeutic purposes. The potential applications of this feature include circulating tumor cell screening, magnetic targeting, and magnetic delivery/manipulation of therapeutic agents. Controlled nanoparticle movement can also be used for image guidance, such as magnetomotive US/PA imaging. Magnetomotive imaging allows sensitive detection of particles by assessing changes in speckle patterns due to particle movement upon application of a pulsed magnetic field.

⁶ Magnetic trapping experiments were performed in collaboration with Kelsey Kubelick from the Ultrasound Imaging and Therapeutics Research Laboratory at Georgia Tech

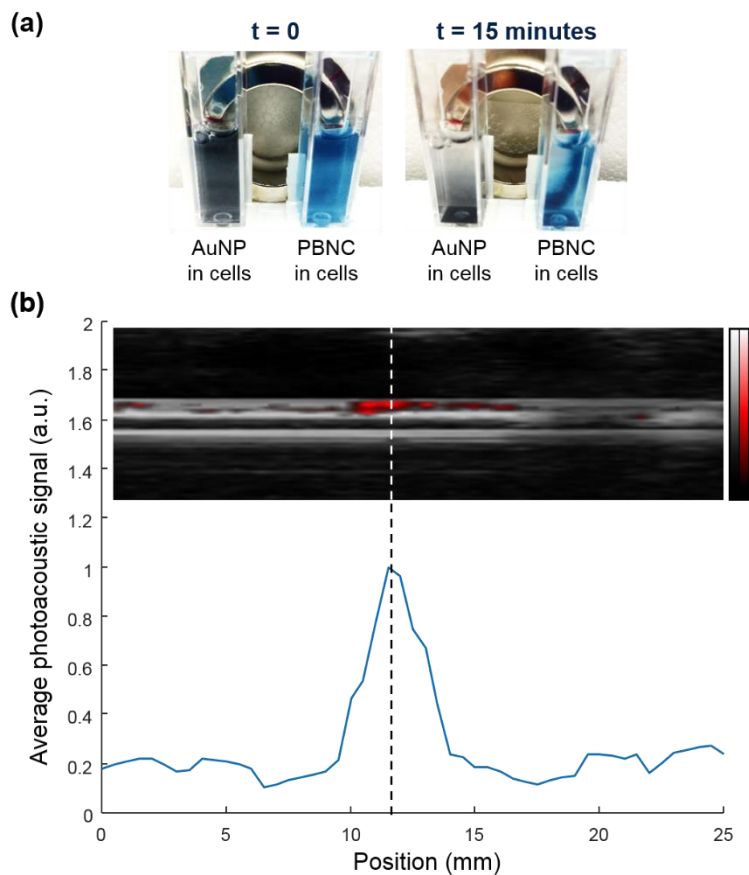


Figure 40 – Image-guided magnetic trapping of cells labeled with 20-nm PBNCs. (a) PBNC-labeled cells can be manipulated using an external magnet, as opposed to the AuNP-labeled cells (control). (b) Insert: ultrasound (gray scale) and photoacoustic (color scale) image of capillary tube with PBNC-labeled cells trapped at the bar magnet, indicated by the dashed line. The integrated PA signal along the tube length shows a 5-fold PA signal increase at the gradient magnet position.

6.8 Discussion

In addition to the results shown, PBNCs possess capabilities for numerous additional applications. Prussian blue's high affinity to heavy metals may be exploited beyond heavy metal poisoning treatment, its current clinical use. This attribute could allow tagging of PBNCs with compounds such as barium sulfate to enable X-ray imaging contrast¹⁸⁶. In addition to magnetic manipulation and magnetomotive imaging

techniques, PBNC's magnetic properties could enhance magnetic hyperthermia using alternating magnetic fields, potentially improving therapeutic penetration depth¹⁸⁷⁻¹⁸⁸, with the possibility to be combined with photothermal therapy to augment heating capability¹⁸⁹.

The ability to consistently vary the size of the PBNCs according to SPION precursors' diameter further adds to imaging and therapeutic possibilities. Studies have shown that particle size can impact the effectiveness of Prussian blue in treatment of heavy metal poisoning¹⁹⁰⁻¹⁹¹. Moreover, it has been shown that the size and shape of single-domain particles can affect their magnetic properties, which may influence their behavior in magnetic manipulation and heating applications.^{166, 192-195}

The reaction scheme presented takes advantage of the decades of previous work to optimize Fe₃O₄ nanoparticles. Currently, there are numerous commercial sources of Fe₃O₄ nanoparticles that provide monodisperse colloidal aqueous solutions with diameters ranging from 5 nm to greater than 50 nm. Furthermore, numerous forms of Fe₃O₄ nanoparticles have been FDA approved for various applications, so rigorous protocols for large batch production and thorough physicochemical characterization have been optimized for the FDA required current Good Manufacturing Practices (cGMP).¹⁹⁶ This reduces the costs and will allow for quicker clinical translation of Prussian blue nanoparticle-based applications.

While SPIONs are ubiquitous in applications involving nanoparticle-magnetic field interactions, such as MRI, magnetically-guided drug delivery, and magnetomotive imaging, the developed PBNCs offer the enhanced benefit of NIR absorption while maintaining strong magnetization properties. The strong optical absorption alone makes

PBNCs a great option for applications including photoacoustic imaging, optical microscopy, and photothermal therapy.

In oncology, PBNCs could be applicable to diagnostic procedures that use MRI, taking advantage of whole-body imaging, but would also enable real-time precise imaging with the versatility of US/PA. Specifically, the agent could be used in the detection of SLN metastasis, as has been already suggested using US/PA and MRI.

6.9 Conclusions

A method for size-controlled synthesis of PBNCs using conventional SPIONs as precursor was presented. The size of the PBNCs can be controlled by the size of the SPIONs. Because highly monodisperse SPIONs are available commercially, this synthesis gives researchers a facile method to produce PBNCs with excellent size control. The resulting PBNCs possess all of the attractive optical and magnetic properties of PBNCs previously shown with conventional syntheses. The utility of PBNCs as imaging agents for MRI and photoacoustic imaging was confirmed. Particularly, PBNCs showed feasibility to be used in immunofunctional imaging of sentinel lymph nodes. Additionally, magnetic properties show potential for novel diagnostic and therapeutic applications such as circulating tumor cell screening and magnetically-guided cell delivery. Overall, the novel synthesis method represents a tool-box for researchers to easily tailor PBNCs by tuning and optimizing the desired nanoparticle size according to the requirements of each application, helping to expand the biomedical uses of PBNCs.

CHAPTER 7. CONCLUSIONS AND FUTURE WORK

7.1 Summary

Photoacoustic imaging is becoming widespread in the medical imaging research field. Ultrasound systems are ubiquitous in healthcare facilities and, because photoacoustic systems share most of the hardware of ultrasound systems, upgrading conventional platforms with a laser source would allow to exploit the benefits of PA imaging without major infrastructure requirements. Contrast agents increase the utility of US/PA significantly; however, novel exogenous materials can also raise safety concerns prior to clinical translation, compared with label-free techniques. This translation can be promoted by showing the usefulness of US/PA in diagnosing and guiding treatment of diseases that have traditionally been difficult to assess with other conventional methods. In this work, the goal was to demonstrate that contrast-enhanced US/PA techniques can help in the early diagnosis of lymph node metastasis, a significant health problem in the U.S. and the world.

Chapter 1 introduced the challenges in diagnosis of sentinel lymph node metastasis. Sentinel lymph node biopsy, the current clinical standard, has a high accuracy, but the procedure still faces disadvantages such as being invasive and requiring multiple specialists. Several attempts to assess sentinel lymph nodes non-invasively have shown promising results, but many have important drawbacks and costs that are not necessarily surpassed by the benefit of non-invasiveness. Various applications of US/PA in oncology were introduced as a motivation for the use of this technology.

In Chapter 2 the ability for functional diagnosis of lymph node metastasis based on nanoparticle-loaded immune cell distribution was investigated. The results showed a statistically significant reduction of the lymph node volume occupied by endocytosed nanoparticles when the node was metastatic. The technique has the advantage of using a nanoparticle with glycol-chitosan as a coating that promotes immune cell uptake, thus not needing specific targeting moieties. As such, it is independent of the tumor's molecular characteristics thus the same contrast agent may be applicable to various types of cancer such as breast, oral, melanoma, and prostate, among others. Nevertheless, to design appropriate treatments, physicians may need to know the molecular characteristics and size of metastasis precisely. In these cases, molecular imaging presented in Chapter 3 would complement the findings of the immunofunctional assessment.

Thus, label-free functional imaging, contrast-enhanced functional imaging, and contrast-enhanced molecular imaging should be perceived as synergistic techniques, and a complement to one another. While this combination can provide greater diagnostic results, it is important to avoid cross-talk between contrast agents. If immunofunctional and molecular imaging needed to be used in conjunction, different contrast agents would have to be used. The photoacoustic/fluorescent agent investigated in Chapter 4 can solve this issue by offering a distinct absorption spectrum that can be responsive to a biomarker of interest and does not overlap with the spectrum of gold nanoparticles. Additionally, the agent's fluorescence response provides high sensitivity which may be critical in the case of small lesions that are otherwise difficult to localize with PA alone.

Chapter 5 presented a gold-silica Janus nanoparticle that could also enhance sensitivity and provide different absorption spectrum signatures. In addition, this nanoparticle can potentially be loaded with drugs to enable therapeutic applications.

When studying contrast agent and drug development, it is important to note that only about 10% of drugs that start Phase I clinical trials make it to FDA approval¹⁹⁷ and this number is reduced to 5% for oncology-related drugs¹⁹⁸. Even when the benefits of particular contrast agents are high, safety concerns may still prevent them from getting approved. It is thus important to study alternative agents and focus on those with greater efficacy and biocompatibility. In Chapter 6, a versatile multifunctional Prussian blue nanoparticle, that is also biocompatible and based on FDA-approved materials, was studied. The nanoparticle size can be tuned to the needs of each application and offers multifunctional capabilities that may be used for assessment and treatment guidance of cancer using US/PA, MRI, and magnetomotive techniques.

Overall, the presented techniques and agents are expected to pave the way for accurate non-invasive evaluation of cancerous tissues. Specifically, in the case of sentinel lymph node metastasis, successful implementation of these tools may augment and potentially replace sentinel lymph node biopsy.

7.2 Future studies with developed contrast agents

There is opportunity for more studies in many applications using the contrast agents included in this text. Particularly, the use of targeting moieties for detection of specific biomarkers would allow a thorough evaluation of the contrast agents' efficacy. Surface modifications of gold and silica using thiols and silane chemistry, respectively, have been

studied extensively. In the case of Prussian blue, various surface modifications have been demonstrated, but a standard technique has not been established¹⁹⁹.

Modifications can also enable therapeutic use. For instance, gold-silica Janus nanoparticles can be loaded with drugs or dyes within the silica shell. Preliminary studies showed the ability to load a fluorescent dye (ICG) in the silica shells (Figure 41). The addition of a fluorescent NIR dye brings two new features: the possibility to track GSJNPs prior to endocytosis by targeted cells, and the enhanced imaging sensitivity with the use of fluorescence imaging. Moreover, this encourages the possibility for loading drugs on the silica half-shell, as has been shown in other studies with silica nanoparticles¹¹⁴, to provide image-guided therapy of lymph node metastasis.

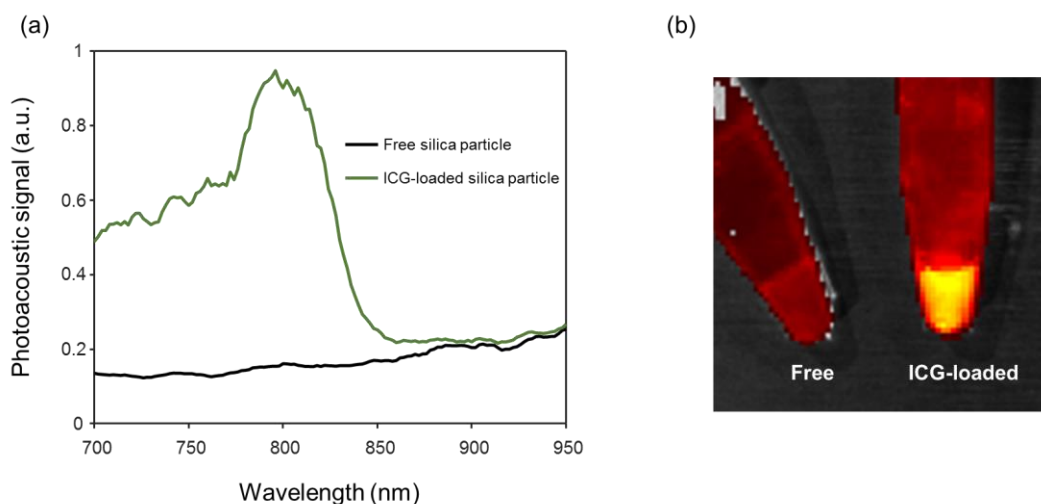


Figure 41 – Comparison of silica nanoparticles vs ICG-loaded silica nanoparticles.

(a) Photoacoustic spectra (b) Fluorescence imaging.

7.3 A theranostic paradigm: towards image-guided therapy and outcome monitoring

Early detection of cancer is paramount to increase survival rates. However, diagnosis would be futile if it did not influence treatment decision. While research towards non-invasive diagnoses intends to decrease patient morbidity, current treatments rather than invasive diagnoses are the main cause of iatrogenic morbidity for cancer patients.

Treatment for cancer is highly dependent on its stage and molecular characteristics. In breast cancer, for instance, early stages are usually treated with local therapy, which includes surgical removal of the primary tumor, followed by radiotherapy. Local therapy is not expected to considerably affect other areas of the body; however, it is not exempt of morbidity and side effects²⁰⁰⁻²⁰¹. When metastasis is found during SLN biopsy, removal of the lymphatic branch via lymphadenectomy is usually performed. This procedure also carries morbidity, particularly the risk of swelling and developing lymphedema²⁰².

Many patients also undergo systemic treatments. Due to heterogeneity of breast cancer, the type of drug(s) administered depends on the tumor characteristics, which must be obtained from biopsy analysis. These analyses will provide information of the hormone (estrogen and progesterone) and growth factor (HER2/neu) receptors present in the tumor²⁰³. Systemic therapies include chemotherapy, hormone therapy and targeted therapy. Chemotherapy is frequently used and causes high morbidity due to side effects such as hair loss, digestive problems, and effects in the bone marrow²⁰⁴⁻²⁰⁵. Certain types of cancer can be treated with hormone therapy, which has milder short-term side effects, but increases the chance of developing endometrial cancer and blood clots²⁰⁶. Targeted therapy is used

in tumors with HER2 receptor overexpression and includes monoclonal antibodies and kinase inhibitors. Tumors can become resistant to some of these drugs, which are often given along with chemotherapy. Heart damage is among the most serious side effects of targeted therapy²⁰⁷.

None of the treatment options for cancer is free of side effects. Thus, a system to design and tune therapeutic plans on a patient-specific basis is needed. Moreover, choosing procedures and drugs with minimal side effects and high success rate would be of extreme benefit during all stages of breast cancer.

Future studies should utilize contrast agents that can serve a diagnostic and therapeutic purpose. For instance, optically-absorbing nanoparticles, such as gold and Prussian blue, can be heated via photothermal effect and used for hyperthermia treatments. This allows for greater thermal gradients, protecting surrounding tissue from undesired damage. Hyperthermia applications can also benefit from accurate real-time information regarding tissue temperature or therapeutic endpoint, thus ultrasound and photoacoustic imaging have been studied as tools to monitor temperature during photothermal therapy²⁰⁸⁻²⁰⁹. Combining diagnostic and therapeutic imaging techniques, a metastatic lesion could be identified and immediately treated under image guidance.

Finally, longitudinal assessment of treated lesions could be performed non-invasively with US/PA. For example, the effect of adjuvant therapy on primary tumors and sentinel lymph nodes could be assessed using contrast enhanced functional/molecular imaging techniques. Prussian blue nanocubes could be used with MRI when whole-body imaging is needed. Then, US/PA could allow precise evaluation of suspicious regions.

7.4 Conclusion

The results presented in this work are promising regarding the use of contrast-enhanced ultrasound and photoacoustic imaging in oncology. While the experiments focused on US/PA as a diagnostic technique for sentinel lymph node metastasis, there is potential for a broader impact in the oncology field as part of multimodal/multifunctional theranostic strategies. A collective effort among the medical imaging community will help find the optimal imaging modalities and contrast agents for each application. Overall, these efforts can aid physicians to enhance and potentially replace current clinical methods for effective diagnosis and treatment of cancer with reduced patient morbidity.

REFERENCES

1. American Cancer Society, Cancer Facts & Figures 2018. *Atlanta: American Cancer Society* **2018**.
2. Hanahan, D.; Weinberg, R. A., Hallmarks of cancer: the next generation. *Cell* **2011**, *144* (5), 646-674.
3. Nathanson, S. D., Insights into the mechanisms of lymph node metastasis. *Cancer* **2003**, *98* (2), 413-423.
4. Mariani, G.; Moresco, L.; Viale, G.; Villa, G.; Bagnasco, M.; Canavese, G.; Buscombe, J.; Strauss, H. W.; Paganelli, G., Radioguided sentinel lymph node biopsy in breast cancer surgery. *Journal of Nuclear Medicine* **2001**, *42* (8), 1198-1215.
5. Moncayo, V. M.; Aarsvold, J. N.; Alazraki, N. P., Lymphoscintigraphy and sentinel nodes. *Journal of Nuclear Medicine* **2015**, *56* (6), 901-907.
6. Saidha, N. K.; Aggarwal, R.; Sen, A., Identification of Sentinel Lymph Nodes Using Contrast-Enhanced Ultrasound in Breast Cancer. *Indian Journal of Surgical Oncology* **2017**, 1-7.
7. Hirche, C.; Murawa, D.; Mohr, Z.; Kneif, S.; Hünerbein, M., ICG fluorescence-guided sentinel node biopsy for axillary nodal staging in breast cancer. *Breast Cancer Research and Treatment* **2010**, *121* (2), 373-378.
8. Pantel, K.; von Knebel Doeberitz, M., Detection and clinical relevance of micrometastatic cancer cells. *Current Opinion in Oncology*, *12*(1) **2000**, 95-101.
9. Sanguinetti, A.; Polistena, A.; Lucchini, R.; Monacelli, M.; Triola, R.; Avenia, S.; ...; Avenia, N., Breast cancer micrometastasis and axillary sentinel lymph nodes frozen section. Our experience and review of literature. *International Journal of Surgery* **2014**.
10. Heesakkers, R. A.; Hövels, A. M.; Jager, G. J.; van den Bosch, H. C.; Witjes, J. A.; Raat, H. P.; Severens, J. L.; Adang, E. M.; van der Kaa, C. H.; Fütterer, J. J., MRI with a lymph-node-specific contrast agent as an alternative to CT scan and lymph-node dissection in patients with prostate cancer: a prospective multicohort study. *The Lancet Oncology* **2008**, *9* (9), 850-856.

11. Harisinghani, M. G.; Barentsz, J.; Hahn, P. F.; Deserno, W. M.; Tabatabaei, S.; van de Kaa, C. H.; de la Rosette, J.; Weissleder, R., Noninvasive detection of clinically occult lymph-node metastases in prostate cancer. *New England Journal of Medicine* **2003**, *348* (25), 2491-2499.
12. Tseng, Y.-C.; Xu, Z.; Guley, K.; Yuan, H.; Huang, L., Lipid–calcium phosphate nanoparticles for delivery to the lymphatic system and SPECT/CT imaging of lymph node metastases. *Biomaterials* **2014**, *35* (16), 4688-4698.
13. Wunderbaldinger, P., Problems and prospects of modern lymph node imaging. *European Journal of Radiology* **2006**, *58* (3), 325-337.
14. Mallidi, S.; Wang, B.; Mehrmohammadi, M.; Qu, M.; Chen, Y.-S.; Joshi, P.; Kim, S.; Homan, K.; Karpouk, A.; Smalling, R. In *Ultrasound-based imaging of nanoparticles: From molecular and cellular imaging to therapy guidance*, Ultrasonics Symposium (IUS), 2009 IEEE International, IEEE: 2009; pp 27-36.
15. Mallidi, S.; Luke, G. P.; Emelianov, S., Photoacoustic imaging in cancer detection, diagnosis, and treatment guidance. *Trends in Biotechnology* **2011**, *29* (5), 213-221.
16. Hannah, A.; Luke, G.; Wilson, K.; Homan, K.; Emelianov, S., Indocyanine green-loaded photoacoustic nanodroplets: dual contrast nanoconstructs for enhanced photoacoustic and ultrasound imaging. *ACS Nano* **2013**, *8* (1), 250-259.
17. Hannah, A. S.; VanderLaan, D.; Chen, Y.-S.; Emelianov, S. Y., Photoacoustic and ultrasound imaging using dual contrast perfluorocarbon nanodroplets triggered by laser pulses at 1064 nm. *Biomedical Optics Express* **2014**, *5* (9), 3042-3052.
18. Erpelding, T. N.; Kim, C.; Pramanik, M.; Jankovic, L.; Maslov, K.; Guo, Z.; Margenthaler, J. A.; Pashley, M. D.; Wang, L. V., Sentinel lymph nodes in the rat: noninvasive photoacoustic and US imaging with a clinical US system. *Radiology* **2010**, *256* (1), 102-110.
19. Kim, C.; Song, K. H.; Gao, F.; Wang, L. V., Sentinel lymph nodes and lymphatic vessels: noninvasive dual-modality in vivo mapping by using indocyanine green in rats—volumetric spectroscopic photoacoustic imaging and planar fluorescence imaging 1. *Radiology* **2010**, *255* (2), 442-450.
20. Pramanik, M.; Song, K. H.; Swierczewska, M.; Green, D.; Sitharaman, B.; Wang, L. V., In vivo carbon nanotube-enhanced non-invasive photoacoustic mapping of the sentinel lymph node. *Physics in Medicine and Biology* **2009**, *54* (11), 3291.
21. Akers, W. J.; Kim, C.; Berezin, M.; Guo, K.; Fuhrhop, R.; Lanza, G. M.; Fischer, G. M.; Daltrozzo, E.; Zumbusch, A.; Cai, X., Noninvasive photoacoustic and fluorescence sentinel lymph node identification using dye-loaded perfluorocarbon nanoparticles. *ACS Nano* **2010**, *5* (1), 173-182.

22. Song, K. H.; Kim, C.; Maslov, K.; Wang, L. V., Noninvasive in vivo spectroscopic nanorod-contrast photoacoustic mapping of sentinel lymph nodes. *European Journal of Radiology* **2009**, *70* (2), 227-231.
23. Hannah, A. S.; Luke, G. P.; Emelianov, S. Y., Blinking Phase-Change Nanocapsules Enable Background-Free Ultrasound Imaging. *Theranostics* **2016**, *6* (11), 1866.
24. Luke, G. P.; Myers, J. N.; Emelianov, S. Y.; Sokolov, K. V., Sentinel lymph node biopsy revisited: ultrasound-guided photoacoustic detection of micrometastases using molecularly targeted plasmonic nanosensors. *Cancer Research* **2014**, *74* (19), 5397-5408.
25. Luke, G. P.; Emelianov, S. Y., Label-free detection of lymph node metastases with US-guided functional photoacoustic imaging. *Radiology* **2015**, *277* (2), 435-442.
26. Kim, C.; Cho, E. C.; Chen, J.; Song, K. H.; Au, L.; Favazza, C.; Zhang, Q.; Cobley, C. M.; Gao, F.; Xia, Y., In vivo molecular photoacoustic tomography of melanomas targeted by bioconjugated gold nanocages. *ACS Nano* **2010**, *4* (8), 4559-4564.
27. Luke, G. P.; Yeager, D.; Emelianov, S. Y., Biomedical applications of photoacoustic imaging with exogenous contrast agents. *Annals of Biomedical Engineering* **2012**, *40* (2), 422-437.
28. Weber, J.; Beard, P. C.; Bohndiek, S. E., Contrast agents for molecular photoacoustic imaging. *Nature Methods* **2016**, *13* (8), 639.
29. Smith, A. M.; Mancini, M. C.; Nie, S., Bioimaging: second window for in vivo imaging. *Nature Nanotechnology* **2009**, *4* (11), 710-711.
30. Zhang, Q.; Iwakuma, N.; Sharma, P.; Moudgil, B.; Wu, C.; McNeill, J.; Jiang, H.; Grobmyer, S., Gold nanoparticles as a contrast agent for in vivo tumor imaging with photoacoustic tomography. *Nanotechnology* **2009**, *20* (39), 395102.
31. Li, W.; Chen, X., Gold nanoparticles for photoacoustic imaging. *Nanomedicine* **2015**, *10* (2), 299-320.
32. Yoon, S. J.; Mallidi, S.; Tam, J. M.; Tam, J. O.; Murthy, A.; Johnston, K. P.; Sokolov, K. V.; Emelianov, S. Y., Utility of biodegradable plasmonic nanoclusters in photoacoustic imaging. *Optics Letters* **2010**, *35* (22), 3751-3753.
33. Rengan, A. K.; Bukhari, A. B.; Pradhan, A.; Malhotra, R.; Banerjee, R.; Srivastava, R.; De, A., In vivo analysis of biodegradable liposome gold nanoparticles as efficient agents for photothermal therapy of cancer. *Nano Letters* **2015**, *15* (2), 842-848.
34. Ku, G.; Zhou, M.; Song, S.; Huang, Q.; Hazle, J.; Li, C., Copper sulfide nanoparticles as a new class of photoacoustic contrast agent for deep tissue imaging at 1064 nm. *ACS Nano* **2012**, *6* (8), 7489-7496.

35. Liu, X.; Atwater, M.; Wang, J.; Huo, Q., Extinction coefficient of gold nanoparticles with different sizes and different capping ligands. *Colloids and Surfaces B: Biointerfaces* **2007**, 58 (1), 3-7.
36. Beziere, N.; Lozano, N.; Nunes, A.; Salichs, J.; Queiros, D.; Kostarelos, K.; Ntziachristos, V., Dynamic imaging of PEGylated indocyanine green (ICG) liposomes within the tumor microenvironment using multi-spectral optoacoustic tomography (MSOT). *Biomaterials* **2015**, 37, 415-424.
37. Cox, B.; Laufer, J. G.; Arridge, S. R.; Beard, P. C., Quantitative spectroscopic photoacoustic imaging: a review. *Journal of Biomedical Optics* **2012**, 17 (6), 0612021-0612022.
38. Kim, S.; Chen, Y.-S.; Luke, G. P.; Emelianov, S. Y., In vivo three-dimensional spectroscopic photoacoustic imaging for monitoring nanoparticle delivery. *Biomedical Optics Express* **2011**, 2 (9), 2540-2550.
39. Li, M.-L.; Oh, J.-T.; Xie, X.; Ku, G.; Wang, W.; Li, C.; Lungu, G.; Stoica, G.; Wang, L. V., Simultaneous molecular and hypoxia imaging of brain tumors in vivo using spectroscopic photoacoustic tomography. *Proceedings of the IEEE* **2008**, 96 (3), 481-489.
40. Fukumura, D.; Jain, R. K., Tumor microenvironment abnormalities: causes, consequences, and strategies to normalize. *Journal of Cellular Biochemistry* **2007**, 101 (4), 937-949.
41. Carmeliet, P.; Jain, R. K., Angiogenesis in cancer and other diseases. *Nature* **2000**, 407 (6801), 249-257.
42. Lungu, G. F.; Li, M.-L.; Xie, X.; Wang, L. V.; Stoica, G., In vivo imaging and characterization of hypoxia-induced neovascularization and tumor invasion. *International Journal of Oncology* **2007**, 30 (1), 45-54.
43. Luke, G. P.; Emelianov, S. Y., Label-free Detection of Lymph Node Metastases with US-guided Functional Photoacoustic Imaging. *Radiology* **2015**, 435-442.
44. Mallidi, S.; Watanabe, K.; Timerman, D.; Schoenfeld, D.; Hasan, T., Prediction of tumor recurrence and therapy monitoring using ultrasound-guided photoacoustic imaging. *Theranostics* **2015**, 5 (3), 289.
45. Luke, G. P.; Nam, S. Y.; Emelianov, S. Y., Optical wavelength selection for improved spectroscopic photoacoustic imaging. *Photoacoustics* **2013**, 1 (2), 36-42.
46. Jaracz, S.; Chen, J.; Kuznetsova, L. V.; Ojima, I., Recent advances in tumor-targeting anticancer drug conjugates. *Bioorganic & Medicinal Chemistry* **2005**, 13 (17), 5043-5054.

47. Byrne, J. D.; Betancourt, T.; Brannon-Peppas, L., Active targeting schemes for nanoparticle systems in cancer therapeutics. *Advanced Drug Delivery Reviews* **2008**, *60* (15), 1615-1626.
48. van Vlerken, L. E.; Vyas, T. K.; Amiji, M. M., Poly (ethylene glycol)-modified nanocarriers for tumor-targeted and intracellular delivery. *Pharmaceutical Research* **2007**, *24* (8), 1405-1414.
49. Pan, D.; Pramanik, M.; Senpan, A.; Allen, J. S.; Zhang, H.; Wickline, S. A.; Wang, L. V.; Lanza, G. M., Molecular photoacoustic imaging of angiogenesis with integrin-targeted gold nanobeacons. *The FASEB Journal* **2011**, *25* (3), 875-882.
50. Li, P.-C.; Wang, C.-R. C.; Shieh, D.-B.; Wei, C.-W.; Liao, C.-K.; Poe, C.; Jhan, S.; Ding, A.-A.; Wu, Y.-N., In vivo photoacoustic molecular imaging with simultaneous multiple selective targeting using antibody-conjugated gold nanorods. *Optics Express* **2008**, *16* (23), 18605-18615.
51. Sokolov, K.; Follen, M.; Aaron, J.; Pavlova, I.; Malpica, A.; Lotan, R.; Richards-Kortum, R., Real-time vital optical imaging of precancer using anti-epidermal growth factor receptor antibodies conjugated to gold nanoparticles. *Cancer Research* **2003**, *63* (9), 1999-2004.
52. Chen, H.; Wang, L.; Yeh, J.; Wu, X.; Cao, Z.; Wang, Y. A.; Zhang, M.; Yang, L.; Mao, H., Reducing non-specific binding and uptake of nanoparticles and improving cell targeting with an antifouling PEO-b-PyMPS copolymer coating. *Biomaterials* **2010**, *31* (20), 5397-5407.
53. Levi, J.; Kothapalli, S. R.; Ma, T.-J.; Hartman, K.; Khuri-Yakub, B. T.; Gambhir, S. S., Design, synthesis, and imaging of an activatable photoacoustic probe. *Journal of the American Chemical Society* **2010**, *132* (32), 11264-11269.
54. Levi, J.; Kothapalli, S.-R.; Bohndiek, S.; Yoon, J.-K.; Dragulescu-Andrasi, A.; Nielsen, C.; Tisma, A.; Bodapati, S.; Gowrishankar, G.; Yan, X., Molecular photoacoustic imaging of follicular thyroid carcinoma. *Clinical Cancer Research* **2013**, *19* (6), 1494-1502.
55. Fukumura, D.; Jain, R. K., Tumor microvasculature and microenvironment: targets for anti-angiogenesis and normalization. *Microvascular Research* **2007**, *74* (2), 72-84.
56. Peer, D.; Karp, J. M.; Hong, S.; Farokhzad, O. C.; Margalit, R.; Langer, R., Nanocarriers as an emerging platform for cancer therapy. *Nature Nanotechnology* **2007**, *2* (12), 751-760.
57. Maeda, H.; Wu, J.; Sawa, T.; Matsumura, Y.; Hori, K., Tumor vascular permeability and the EPR effect in macromolecular therapeutics: a review. *Journal of Controlled Release* **2000**, *65* (1), 271-284.

58. Seungsoo, K.; Yun-sheng, C.; Luke, G. P.; Emelianov, S. Y., In-vivo ultrasound and photoacoustic image- guided photothermal cancer therapy using silica-coated gold nanorods. *Ultrasonics, Ferroelectrics, and Frequency Control, IEEE Transactions on* **2014**, *61* (5), 891-897.
59. Alacam, B.; Yazici, B.; Intes, X.; Nioka, S.; Chance, B., Pharmacokinetic-rate images of indocyanine green for breast tumors using near-infrared optical methods. *Physics in Medicine and Biology* **2008**, *53* (4), 837.
60. Cuccia, D. J.; Bevilacqua, F.; Durkin, A. J.; Merritt, S.; Tromberg, B. J.; Gulsen, G.; Yu, H.; Wang, J.; Nalcioğlu, O., In vivo quantification of optical contrast agent dynamics in rat tumors by use of diffuse optical spectroscopy with magnetic resonance imaging coregistration. *Applied Optics* **2003**, *42* (16), 2940-2950.
61. Sriraman, S. K.; Aryasomayajula, B.; Torchilin, V. P., Barriers to drug delivery in solid tumors. *Tissue Barriers* **2014**, *2* (3), e29528.
62. Prabhakar, U.; Maeda, H.; Jain, R. K.; Sevick-Muraca, E. M.; Zamboni, W.; Farokhzad, O. C.; Barry, S. T.; Gabizon, A.; Grodzinski, P.; Blakey, D. C., Challenges and key considerations of the enhanced permeability and retention effect for nanomedicine drug delivery in oncology. *Cancer Research* **2013**, *73* (8), 2412-2417.
63. Allard, W. J.; Matera, J.; Miller, M. C.; Repollet, M.; Connelly, M. C.; Rao, C.; Tibbe, A. G.; Uhr, J. W.; Terstappen, L. W., Tumor cells circulate in the peripheral blood of all major carcinomas but not in healthy subjects or patients with nonmalignant diseases. *Clinical Cancer Research* **2004**, *10* (20), 6897-6904.
64. Galanzha, E. I.; Shashkov, E. V.; Spring, P. M.; Suen, J. Y.; Zharov, V. P., In vivo, noninvasive, label-free detection and eradication of circulating metastatic melanoma cells using two-color photoacoustic flow cytometry with a diode laser. *Cancer Research* **2009**, *69* (20), 7926-7934.
65. Galanzha, E. I.; Shashkov, E. V.; Kelly, T.; Kim, J.-W.; Yang, L.; Zharov, V. P., In vivo magnetic enrichment and multiplex photoacoustic detection of circulating tumour cells. *Nature Nanotechnology* **2009**, *4* (12), 855-860.
66. Wei, C. w.; Xia, J.; Pelivanov, I.; Jia, C.; Huang, S. W.; Hu, X.; Gao, X.; O'Donnell, M., Magnetomotive photoacoustic imaging: in vitro studies of magnetic trapping with simultaneous photoacoustic detection of rare circulating tumor cells. *Journal of Biophotonics* **2013**, *6* (6-7), 513-522.
67. Karaman, S.; Detmar, M., Mechanisms of lymphatic metastasis. *The Journal of Clinical Investigation* **2014**, *124* (3), 922-928.
68. Pereira, E. R.; Jones, D.; Jung, K.; Padera, T. P., The lymph node microenvironment and its role in the progression of metastatic cancer, *Seminars in Cell & Developmental Biology*, Elsevier: 2015; pp 98-105.

69. Ji, R.-C., Lymph nodes and cancer metastasis: New perspectives on the role of intranodal lymphatic sinuses. *International Journal of Molecular Sciences* **2016**, *18* (1), 51.
70. Cochran, A. J.; Huang, R.-R.; Lee, J.; Itakura, E.; Leong, S. P.; Essner, R., Tumour-induced immune modulation of sentinel lymph nodes. *Nature Reviews Immunology* **2006**, *6* (9), 659.
71. Nam, S. Y.; Ricles, L. M.; Suggs, L. J.; Emelianov, S. Y., Nonlinear photoacoustic signal increase from endocytosis of gold nanoparticles. *Optics Letters* **2012**, *37* (22), 4708-4710.
72. Sun, I.-C.; Na, J. H.; Jeong, S. Y.; Kim, D.-E.; Kwon, I. C.; Choi, K.; Ahn, C.-H.; Kim, K., Biocompatible glycol chitosan-coated gold nanoparticles for tumor-targeting CT imaging. *Pharmaceutical Research* **2014**, *31* (6), 1418-1425.
73. Sun, I.-C.; Dumani, D.; Emelianov, S. Y., Ultrasound-guided photoacoustic imaging of lymph nodes with biocompatible gold nanoparticles as a novel contrast agent (Conference Presentation), *Colloidal Nanoparticles for Biomedical Applications XII*, International Society for Optics and Photonics: 2017; p 100780E.
74. Leleux, J.; Atalis, A.; Roy, K., Engineering immunity: Modulating dendritic cell subsets and lymph node response to direct immune-polarization and vaccine efficacy. *Journal of Controlled Release* **2015**, *219*, 610-621.
75. Li, X.; Min, M.; Du, N.; Gu, Y.; Hode, T.; Naylor, M.; Chen, D.; Nordquist, R. E.; Chen, W. R., Chitin, Chitosan, and Glycated Chitosan Regulate Immune Responses: The Novel Adjuvants for Cancer Vaccine. *Clinical and Developmental Immunology* **2013**, *2013*, 8.
76. Song, S.; Zhou, F.; Nordquist, R. E.; Carubelli, R.; Liu, H.; Chen, W. R., Glycated chitosan as a new non-toxic immunological stimulant. *Immunopharmacology and Immunotoxicology* **2009**, *31* (2), 202-208.
77. Pawar, D.; Jaganathan, K., Mucoadhesive glycol chitosan nanoparticles for intranasal delivery of hepatitis B vaccine: enhancement of mucosal and systemic immune response. *Drug Delivery* **2016**, *23* (1), 185-194.
78. Gogev, S.; de Fays, K.; Versali, M.-F.; Gautier, S.; Thiry, E., Glycol chitosan improves the efficacy of intranasally administrated replication defective human adenovirus type 5 expressing glycoprotein D of bovine herpesvirus 1. *Vaccine* **2004**, *22* (15-16), 1946-1953.
79. Wang, C.; Liu, P.; Zhuang, Y.; Li, P.; Jiang, B.; Pan, H.; Liu, L.; Cai, L.; Ma, Y., Lymphatic-targeted cationic liposomes: a robust vaccine adjuvant for promoting long-term immunological memory. *Vaccine* **2014**, *32* (42), 5475-5483.

80. Zhuang, Y.; Ma, Y.; Wang, C.; Hai, L.; Yan, C.; Zhang, Y.; Liu, F.; Cai, L., PEGylated cationic liposomes robustly augment vaccine-induced immune responses: Role of lymphatic trafficking and biodistribution. *Journal of Controlled Release* **2012**, *159* (1), 135-142.
81. Kwon, Y. J.; Standley, S. M.; Goh, S. L.; Fréchet, J. M., Enhanced antigen presentation and immunostimulation of dendritic cells using acid-degradable cationic nanoparticles. *Journal of Controlled Release* **2005**, *105* (3), 199-212.
82. Grootendorst, D. J.; Fratila, R. M.; Visscher, M.; Haken, B. T.; van Wezel, R. J.; Rottenberg, S.; Steenbergen, W.; Manohar, S.; Ruers, T. J., Intra-operative ex vivo photoacoustic nodal staging in a rat model using a clinical superparamagnetic iron oxide nanoparticle dispersion. *Journal of Biophotonics* **2013**, *6* (6-7), 493-504.
83. Grootendorst, D. J.; Fratila, R. M.; Pouw, J.; Ten Haken, B.; Van Wezel, R. J.; Rottenberg, S.; Steenbergen, W.; Manohar, S.; Ruers, T. J., Photoacoustic staging of nodal metastases using SPIOs: Comparison between in vivo, in toto and ex vivo imaging in a rat model. *Biomedical Spectroscopy and Imaging* **2016**, *5* (1), 71-87.
84. Sun, I. C.; Eun, D. K.; Koo, H.; Ko, C. Y.; Kim, H. S.; Yi, D. K.; Choi, K.; Kwon, I. C.; Kim, K.; Ahn, C. H., Tumor-targeting gold particles for dual computed tomography/optical cancer imaging. *Angewandte Chemie International Edition* **2011**, *50* (40), 9348-9351.
85. Bradley, D.; Roth, G., Adaptive thresholding using the integral image. *Journal of Graphics Tools* **2007**, *12* (2), 13-21.
86. Gref, R.; Lück, M.; Quellec, P.; Marchand, M.; Dellacherie, E.; Harnisch, S.; Blunk, T.; Müller, R., 'Stealth' corona-core nanoparticles surface modified by polyethylene glycol (PEG): influences of the corona (PEG chain length and surface density) and of the core composition on phagocytic uptake and plasma protein adsorption. *Colloids and Surfaces B: Biointerfaces* **2000**, *18* (3-4), 301-313.
87. Mansfield, A. S.; Holtan, S. G.; Grotz, T. E.; Allred, J. B.; Jakub, J. W.; Erickson, L. A.; Markovic, S. N., Regional immunity in melanoma: immunosuppressive changes precede nodal metastasis. *Modern Pathology* **2011**, *24* (4), 487.
88. Takeuchi, H.; Kitajima, M.; Kitagawa, Y., Sentinel lymph node as a target of molecular diagnosis of lymphatic micrometastasis and local immunoresponse to malignant cells. *Cancer Science* **2008**, *99* (3), 441-450.
89. Langer, I.; Marti, W. R.; Guller, U.; Moch, H.; Harder, F.; Oertli, D.; Zuber, M., Axillary recurrence rate in breast cancer patients with negative sentinel lymph node (SLN) or SLN micrometastases: prospective analysis of 150 patients after SLN biopsy. *Annals of Surgery* **2005**, *241* (1), 152.
90. Langer, I.; Guller, U.; Viehl, C. T.; Moch, H.; Wight, E.; Harder, F.; Oertli, D.; Zuber, M., Axillary lymph node dissection for sentinel lymph node micrometastases may

be safely omitted in early-stage breast cancer patients: long-term outcomes of a prospective study. *Annals of Surgical Oncology* **2009**, *16* (12), 3366-3374.

91. Pernas, S.; Gil, M.; Benítez, A.; Bajen, M. T.; Climent, F.; Pla, M. J.; Benito, E.; Gumà, A.; Gutierrez, C.; Pisa, A., Avoiding axillary treatment in sentinel lymph node micrometastases of breast cancer: a prospective analysis of axillary or distant recurrence. *Annals of Surgical Oncology* **2010**, *17* (3), 772-777.

92. Yegiyants, S.; Romero, L. M.; Haigh, P. I.; DiFronzo, L. A., Completion axillary lymph node dissection not required for regional control in patients with breast cancer who have micrometastases in a sentinel node. *Archives of Surgery* **2010**, *145* (6), 564-569.

93. Pepels, M. J.; Vestjens, J. H.; De Boer, M.; Smidt, M.; Van Diest, P. J.; Borm, G. F.; Tjan-Heijnen, V. C., Safety of avoiding routine use of axillary dissection in early stage breast cancer: a systematic review. *Breast Cancer Research and Treatment* **2011**, *125* (2), 301-313.

94. Solá, M.; Alberro, J. A.; Fraile, M.; Santesteban, P.; Ramos, M.; Fabregas, R.; Moral, A.; Ballester, B.; Vidal, S., Complete axillary lymph node dissection versus clinical follow-up in breast cancer patients with sentinel node micrometastasis: final results from the multicenter clinical trial AATRM 048/13/2000. *Annals of Surgical Oncology* **2013**, *20* (1), 120-127.

95. Anzai, Y.; Piccoli, C. W.; Outwater, E. K.; Stanford, W.; Bluemke, D. A.; Nurenberg, P.; Saini, S.; Maravilla, K. R.; Feldman, D. E.; Schmiedl, U. P., Evaluation of neck and body metastases to nodes with ferumoxtran 10-enhanced MR imaging: phase III safety and efficacy study. *Radiology* **2003**, *228* (3), 777-788.

96. Khlebtsov, N.; Dykman, L., Biodistribution and toxicity of engineered gold nanoparticles: a review of in vitro and in vivo studies. *Chemical Society Reviews* **2011**, *40* (3), 1647-1671.

97. Choi, H. S.; Liu, W.; Misra, P.; Tanaka, E.; Zimmer, J. P.; Ipe, B. I.; Bawendi, M. G.; Frangioni, J. V., Renal clearance of quantum dots. *Nature Biotechnology* **2007**, *25* (10), 1165-1170.

98. Tam, J. M.; Tam, J. O.; Murthy, A.; Ingram, D. R.; Ma, L. L.; Travis, K.; Johnston, K. P.; Sokolov, K. V., Controlled assembly of biodegradable plasmonic nanoclusters for near-infrared imaging and therapeutic applications. *ACS Nano* **2010**, *4* (4), 2178-2184.

99. Kumar, S.; Aaron, J.; Sokolov, K., Directional conjugation of antibodies to nanoparticles for synthesis of multiplexed optical contrast agents with both delivery and targeting moieties. *Nature Protocols* **2008**, *3* (2), 314.

100. Myers, J. N.; Holsinger, F. C.; Jasser, S. A.; Bekele, B. N.; Fidler, I. J., An orthotopic nude mouse model of oral tongue squamous cell carcinoma. *Clinical Cancer Research* **2002**, *8* (1), 293-298.

101. Sano, D.; Xie, T.; Ow, T. J.; Zhao, M.; Pickering, C. R.; Zhou, G.; Sandulache, V. C.; Wheeler, D. A.; Gibbs, R. A.; Caulin, C., Disruptive TP53 mutation is associated with aggressive disease characteristics in an orthotopic murine model of oral tongue cancer. *Clinical Cancer Research* **2011**, clincanres. 0046.2011.
102. Canny, J., A computational approach to edge detection. *IEEE Transactions on Pattern Analysis and Machine Intelligence* **1986**, (6), 679-698.
103. Azzi, L.; El-Alfy, M.; Martel, C.; Labrie, F., Gender differences in mouse skin morphology and specific effects of sex steroids and dehydroepiandrosterone. *Journal of Investigative Dermatology* **2005**, 124 (1), 22-27.
104. Santiesteban, D. Y.; Kubelick, K.; Dhada, K. S.; Dumani, D.; Suggs, L.; Emelianov, S., Monitoring/Imaging and Regenerative Agents for Enhancing Tissue Engineering Characterization and Therapies. *Annals of Biomedical Engineering* **2016**, 44 (3), 750-772.
105. Cook, J. R.; Dumani, D. S.; Kubelick, K. P.; Luci, J.; Emelianov, S. Y., Prussian blue nanocubes: multi-functional nanoparticles for multimodal imaging and image-guided therapy (Conference Presentation), *Photons Plus Ultrasound: Imaging and Sensing 2017*, International Society for Optics and Photonics: 2017; p 100641T.
106. Pierce, M. C.; Javier, D. J.; Richards-Kortum, R., Optical contrast agents and imaging systems for detection and diagnosis of cancer. *International Journal of Cancer* **2008**, 123 (9), 1979-1990.
107. Ntziachristos, V.; Bremer, C.; Weissleder, R., Fluorescence imaging with near-infrared light: new technological advances that enable in vivo molecular imaging. *European Radiology* **2003**, 13 (1), 195-208.
108. Bremer, C.; Ntziachristos, V.; Weissleder, R., Optical-based molecular imaging: contrast agents and potential medical applications. *European Radiology* **2003**, 13 (2), 231-243.
109. Bulte, J. W.; Kraitchman, D. L., Iron oxide MR contrast agents for molecular and cellular imaging. *NMR in Biomedicine* **2004**, 17 (7), 484-499.
110. Durr, N. J.; Larson, T.; Smith, D. K.; Korgel, B. A.; Sokolov, K.; Ben-Yakar, A., Two-photon luminescence imaging of cancer cells using molecularly targeted gold nanorods. *Nano Letters* **2007**, 7 (4), 941-945.
111. Dumani, D.; Sun, I.-C.; Emelianov, S., In vivo photoacoustic detection of lymph node metastasis using glycol-chitosan-coated gold nanoparticles, *International Ultrasonics Symposium (IUS)*, 2017 IEEE, Washington, DC, IEEE: Washington, DC, 2017; pp 1-4.
112. Weissleder, R.; Nahrendorf, M.; Pittet, M. J., Imaging macrophages with nanoparticles. *Nature Materials* **2014**, 13 (2), 125.

113. Wang, C.; Cheng, L.; Liu, Y.; Wang, X.; Ma, X.; Deng, Z.; Li, Y.; Liu, Z., Imaging-Guided pH-Sensitive Photodynamic Therapy Using Charge Reversible Upconversion Nanoparticles under Near-Infrared Light. *Advanced Functional Materials* **2013**, 23 (24), 3077-3086.
114. Chen, Y.; Yin, Q.; Ji, X.; Zhang, S.; Chen, H.; Zheng, Y.; Sun, Y.; Qu, H.; Wang, Z.; Li, Y., Manganese oxide-based multifunctionalized mesoporous silica nanoparticles for pH-responsive MRI, ultrasonography and circumvention of MDR in cancer cells. *Biomaterials* **2012**, 33 (29), 7126-7137.
115. Razansky, D.; Harlaar, N. J.; Hillebrands, J. L.; Taruttis, A.; Herzog, E.; Zeebregts, C. J.; van Dam, G. M.; Ntziachristos, V., Multispectral optoacoustic tomography of matrix metalloproteinase activity in vulnerable human carotid plaques. *Molecular Imaging and Biology* **2012**, 14 (3), 277-285.
116. de Vries, B. M. W.; Hillebrands, J.-L.; van Dam, G. M.; Tio, R. A.; de Jong, J. S.; Slart, R. H.; Zeebregts, C. J., Multispectral Near-Infrared Fluorescence Molecular Imaging of Matrix Metalloproteinases in a Human Carotid Plaque Using a Matrix-Degrading Metalloproteinase-Sensitive Activatable Fluorescent Probe. *Circulation* **2009**, 119 (20), e534-e536.
117. Frangioni, J. V., New technologies for human cancer imaging. *Journal of Clinical Oncology* **2008**, 26 (24), 4012-4021.
118. Weissleder, R.; Pittet, M. J., Imaging in the era of molecular oncology. *Nature* **2008**, 452 (7187), 580.
119. Lovell, J. F.; Jin, C. S.; Huynh, E.; Jin, H.; Kim, C.; Rubinstein, J. L.; Chan, W. C.; Cao, W.; Wang, L. V.; Zheng, G., Porphysome nanovesicles generated by porphyrin bilayers for use as multimodal biophotonic contrast agents. *Nature Materials* **2011**, 10 (4), 324.
120. Sun, I.-C.; Dumani, D. S.; Emelianov, S. Y., Multimodal imaging of lymph nodes and tumors using glycol-chitosan-coated gold nanoparticles (Conference Presentation), *Photons Plus Ultrasound: Imaging and Sensing 2017*, International Society for Optics and Photonics: 2017; p 100640Y.
121. Harris, J. T.; Dumani, D. S.; Cook, J. R.; Sokolov, K. V.; Emelianov, S. Y.; Homan, K. A., Assessment of plaque vulnerability in atherosclerosis via intravascular photoacoustic imaging of targeted liposomal ICG J-aggregates (Conference Presentation), *Photons Plus Ultrasound: Imaging and Sensing 2017*, International Society for Optics and Photonics: 2017; p 1006413.
122. Harris, J. T.; Dumani, D. S.; Cook, J. R.; Sokolov, K. V.; Emelianov, S. Y.; Homan, K. A., Identification of M1 Macrophages in Vulnerable Plaques With Folate Receptor Beta Targeted Liposomal Indocyanine Green J-Aggregates, *American Heart Association, Inc.*: 2016; p A19605.

123. Landsman, M.; Kwant, G.; Mook, G.; Zijlstra, W., Light-absorbing properties, stability, and spectral stabilization of indocyanine green. *Journal of Applied Physiology* **1976**, 40 (4), 575-583.
124. Hayashi, K.; Hasegawa, Y.; Tokoro, T., Indocyanine green angiography of central serous chorioretinopathy. *International Ophthalmology* **1986**, 9 (1), 37-41.
125. Benson, R.; Kues, H., Fluorescence properties of indocyanine green as related to angiography. *Physics in Medicine & Biology* **1978**, 23 (1), 159.
126. Brecht, H. P.; Ivanov, V.; Dumani, D. S.; Emelianov, S. Y.; Anastasio, M. A.; Ermilov, S. A., A 3D imaging system integrating photoacoustic and fluorescence orthogonal projections for anatomical, functional and molecular assessment of rodent models, *Photons Plus Ultrasound: Imaging and Sensing 2018*, International Society for Optics and Photonics: 2018.
127. Kelly, K. L.; Coronado, E.; Zhao, L. L.; Schatz, G. C., The optical properties of metal nanoparticles: the influence of size, shape, and dielectric environment. *The Journal of Physical Chemistry B* **2003** 107 (3), 668-677.
128. Nicol, J. R.; Dixon, D.; Coulter, J. A., Gold nanoparticle surface functionalization: a necessary requirement in the development of novel nanotherapeutics. *Nanomedicine* **2015**, 10 (8), 1315-1326.
129. García-Soto, M. J.; González-Ortega, O., Synthesis of silica-core gold nanoshells and some modifications/variations. *Gold Bulletin* **2016**, 49 (3-4), 111-131.
130. Chen, Y.-S.; Frey, W.; Kim, S.; Kruizinga, P.; Homan, K.; Emelianov, S., Silica-coated gold nanorods as photoacoustic signal nanoamplifiers. *Nano Letters* **2011**, 11 (2), 348-354.
131. Bayer, C. L.; Nam, S. Y.; Chen, Y.-S.; Emelianov, S. Y., Photoacoustic signal amplification through plasmonic nanoparticle aggregation. *Journal of Biomedical Optics* **2013**, 18 (1), 016001.
132. Hanske, C.; Sanz-Ortiz, M. N.; Liz-Marzán, L. M., Silica-Coated Plasmonic Metal Nanoparticles in Action. *Advanced Materials* **2018**, 1707003.
133. Bastús, N. G.; Comenge, J.; Puntès, V., Kinetically controlled seeded growth synthesis of citrate-stabilized gold nanoparticles of up to 200 nm: size focusing versus Ostwald ripening. *Langmuir* **2011**, 27 (17), 11098-11105.
134. Chen, T.; Chen, G.; Xing, S.; Wu, T.; Chen, H., Scalable Routes to Janus Au– SiO₂ and Ternary Ag– Au– SiO₂ Nanoparticles. *Chemistry of Materials* **2010**, 22 (13), 3826-3828.
135. Lu, Y.; Xiong, H.; Jiang, X.; Xia, Y.; Prentiss, M.; Whitesides, G. M., Asymmetric dimers can be formed by dewetting half-shells of gold deposited on the surfaces of

spherical oxide colloids. *Journal of the American Chemical Society* **2003**, *125* (42), 12724-12725.

136. Deng, Z. J.; Liang, M.; Toth, I.; Monteiro, M. J.; Minchin, R. F., Molecular interaction of poly (acrylic acid) gold nanoparticles with human fibrinogen. *ACS Nano* **2012**, *6* (10), 8962-8969.

137. Barriet, D.; Yam, C. M.; Shmakova, O. E.; Jamison, A. C.; Lee, T. R., 4-Mercaptophenylboronic acid SAMs on gold: comparison with SAMs derived from thiophenol, 4-mercaptophenol, and 4-mercaptobenzoic acid. *Langmuir* **2007**, *23* (17), 8866-8875.

138. Stewart, A. F.; Lee, A.; Ahmed, A.; Ip, S.; Kumacheva, E.; Walker, G. C., Rational design for the controlled aggregation of gold nanorods via phospholipid encapsulation for enhanced Raman scattering. *ACS Nano* **2014**, *8* (6), 5462-5467.

139. Rodríguez-Fernández, D.; Altantzis, T.; Heidari, H.; Bals, S.; Liz-Marzán, L. M., A protecting group approach toward synthesis of Au–silica Janus nanostars. *Chemical Communications* **2014**, *50* (1), 79-81.

140. Liz-Marzán, L. M.; Giersig, M.; Mulvaney, P., Synthesis of nanosized gold– silica core– shell particles. *Langmuir* **1996**, *12* (18), 4329-4335.

141. Izak-Nau, E.; Voetz, M.; Eiden, S.; Duschl, A.; Puentes, V. F., Altered characteristics of silica nanoparticles in bovine and human serum: the importance of nanomaterial characterization prior to its toxicological evaluation. *Particle and Fibre Toxicology* **2013**, *10* (1), 56.

142. Sethuraman, S.; Amirian, J. H.; Litovsky, S. H.; Smalling, R. W.; Emelianov, S. Y., Spectroscopic intravascular photoacoustic imaging to differentiate atherosclerotic plaques. *Optics Express* **2008**, *16* (5), 3362-3367.

143. Wang, B.; Yantsen, E.; Larson, T.; Karpiouk, A. B.; Sethuraman, S.; Su, J. L.; Sokolov, K.; Emelianov, S. Y., Plasmonic intravascular photoacoustic imaging for detection of macrophages in atherosclerotic plaques. *Nano Letters* **2008**, *9* (6), 2212-2217.

144. Mallidi, S.; Larson, T.; Tam, J.; Joshi, P. P.; Karpiouk, A.; Sokolov, K.; Emelianov, S., Multiwavelength photoacoustic imaging and plasmon resonance coupling of gold nanoparticles for selective detection of cancer. *Nano letters* **2009**, *9* (8), 2825-2831.

145. Choi, J.; Burns, A. A.; Williams, R. M.; Zhou, Z.; Flesken-Nikitin, A.; Zipfel, W. R.; Wiesner, U.; Nikitin, A. Y., Core-shell silica nanoparticles as fluorescent labels for nanomedicine. *Journal of Biomedical Optics* **2007**, *12* (6), 064007.

146. Manolova, V.; Flace, A.; Bauer, M.; Schwarz, K.; Saudan, P.; Bachmann, M. F., Nanoparticles target distinct dendritic cell populations according to their size. *European Journal of Immunology* **2008**, *38* (5), 1404-1413.

147. Jeon, Y. H.; Kim, Y.-H.; Choi, K.; Piao, J. Y.; Quan, B.; Lee, Y.-S.; Jeong, J. M.; Chung, J.-K.; Lee, D. S.; Lee, M. C., In vivo imaging of sentinel nodes using fluorescent silica nanoparticles in living mice. *Molecular Imaging and Biology* **2010**, *12* (2), 155-162.
148. Albrecht, W.; Deng, T.-S.; Goris, B.; van Huis, M. A.; Bals, S.; van Blaaderen, A., Single particle deformation and analysis of silica-coated gold nanorods before and after femtosecond laser pulse excitation. *Nano Letters* **2016**, *16* (3), 1818-1825.
149. Zhang, L.; Gu, F.; Chan, J.; Wang, A.; Langer, R.; Farokhzad, O., Nanoparticles in medicine: therapeutic applications and developments. *Clinical Pharmacology & Therapeutics* **2008**, *83* (5), 761-769.
150. Bobo, D.; Robinson, K. J.; Islam, J.; Thurecht, K. J.; Corrie, S. R., Nanoparticle-based medicines: a review of FDA-approved materials and clinical trials to date. *Pharmaceutical Research* **2016**, *33* (10), 2373-2387.
151. Eifler, A. C.; Thaxton, C. S., Nanoparticle therapeutics: FDA approval, clinical trials, regulatory pathways, and case study. In *Biomedical Nanotechnology*, Springer: 2011; pp 325-338.
152. Stafford, S.; Serrano Garcia, R.; Gun'ko, Y. K., Multimodal Magnetic-Plasmonic Nanoparticles for Biomedical Applications. *Applied Sciences* **2018**, *8* (1), 97.
153. Liang, X.; Deng, Z.; Jing, L.; Li, X.; Dai, Z.; Li, C.; Huang, M., Prussian blue nanoparticles operate as a contrast agent for enhanced photoacoustic imaging. *Chemical Communications* **2013**, *49* (94), 11029-11031.
154. Cheng, L.; Gong, H.; Zhu, W.; Liu, J.; Wang, X.; Liu, G.; Liu, Z., PEGylated Prussian blue nanocubes as a theranostic agent for simultaneous cancer imaging and photothermal therapy. *Biomaterials* **2014**, *35* (37), 9844-9852.
155. Jing, L.; Liang, X.; Deng, Z.; Feng, S.; Li, X.; Huang, M.; Li, C.; Dai, Z., Prussian blue coated gold nanoparticles for simultaneous photoacoustic/CT bimodal imaging and photothermal ablation of cancer. *Biomaterials* **2014**, *35* (22), 5814-5821.
156. Reguera, E.; Marín, E.; Calderón, A.; Rodríguez-Hernández, J., Photo-induced charge transfer in Prussian blue analogues as detected by photoacoustic spectroscopy. *Spectrochimica Acta Part A: Molecular and Biomolecular Spectroscopy* **2007**, *68* (1), 191-197.
157. Ozeki, T.; Matsumoto, K.; Hikime, S., Photoacoustic spectra of prussian blue and photochemical reaction of ferric ferricyanide. *Analytical Chemistry* **1984**, *56* (14), 2819-2822.
158. Fu, G.; Liu, W.; Li, Y.; Jin, Y.; Jiang, L.; Liang, X.; Feng, S.; Dai, Z., Magnetic Prussian blue nanoparticles for targeted photothermal therapy under magnetic resonance imaging guidance. *Bioconjugate Chemistry* **2014**, *25* (9), 1655-1663.

159. Hoffman, H. A.; Chakrabarti, L.; Dumont, M. F.; Sandler, A. D.; Fernandes, R., Prussian blue nanoparticles for laser-induced photothermal therapy of tumors. *RSC Advances* **2014**, *4* (56), 29729-29734.
160. Li, Z.; Zeng, Y.; Zhang, D.; Wu, M.; Wu, L.; Huang, A.; Yang, H.; Liu, X.; Liu, J., Glypican-3 antibody functionalized Prussian blue nanoparticles for targeted MR imaging and photothermal therapy of hepatocellular carcinoma. *Journal of Materials Chemistry B* **2014**, *2* (23), 3686-3696.
161. Shokouhimehr, M.; Soehnlén, E. S.; Khitrin, A.; Basu, S.; Huang, S. D., Biocompatible Prussian blue nanoparticles: Preparation, stability, cytotoxicity, and potential use as an MRI contrast agent. *Inorganic Chemistry Communications* **2010**, *13* (1), 58-61.
162. Blanco, E.; Shen, H.; Ferrari, M., Principles of nanoparticle design for overcoming biological barriers to drug delivery. *Nature Biotechnology* **2015**, *33* (9), 941-951.
163. Hobbs, S. K.; Monsky, W. L.; Yuan, F.; Roberts, W. G.; Griffith, L.; Torchilin, V. P.; Jain, R. K., Regulation of transport pathways in tumor vessels: role of tumor type and microenvironment. *Proceedings of the National Academy of Sciences* **1998**, *95* (8), 4607-4612.
164. Wang, S.-J.; Chen, C.-S.; Chen, L.-C., Prussian blue nanoparticles as nanocargoes for delivering DNA drugs to cancer cells. *Science and Technology of Advanced Materials* **2013**, *14* (4), 044405.
165. Hu, M.; Furukawa, S.; Ohtani, R.; Sukegawa, H.; Nemoto, Y.; Reboul, J.; Kitagawa, S.; Yamauchi, Y., Synthesis of Prussian blue nanoparticles with a hollow interior by controlled chemical etching. *Angewandte Chemie* **2012**, *124* (4), 1008-1012.
166. Sutens, B.; Swusten, T.; Zhong, K.; Jochum, J. K.; Van Bael, M. J.; Van der Eycken, E. V.; Brullot, W.; Bloemen, M.; Verbiest, T., Tunability of size and magnetic moment of iron oxide nanoparticles synthesized by forced hydrolysis. *Materials* **2016**, *9* (7), 554.
167. Alvarez-Paino, M.; Marcelo, G.; Munoz-Bonilla, A.; Rodriguez-Hernandez, J.; Fernandez-Garcia, M., Surface modification of magnetite hybrid particles with carbohydrates and gold nanoparticles via “click” chemistry. *Polymer Chemistry* **2013**, *4* (4), 986-995.
168. Kim, Y. S.; Lee, H. J.; Govindaiah, P.; Son, W.; Koh, W.-G.; Cheong, I. W.; Kim, J. H., Preparation of Fe₃O₄-embedded poly (styrene)/poly (thiophene) core/shell nanoparticles and their hydrogel patterns for sensor applications. *Materials* **2014**, *7* (1), 195-205.
169. Rittikulsittichai, S.; Singhana, B.; Bryan, W. W.; Sarangi, S.; Jamison, A. C.; Brazdeikis, A.; Lee, T. R., Preparation, characterization, and utilization of multi-functional

magnetic-fluorescent composites for bio-imaging and magnetic hyperthermia therapy. *RSC Advances* **2013**, 3 (21), 7838-7849.

170. Zhang, H.; Zhang, Q.; Zhang, B.; Guo, F., Preparation of magnetic composite microspheres by surfactant free controlled radical polymerization: Preparation and characteristics. *Journal of Magnetism and Magnetic Materials* **2009**, 321 (23), 3921-3925.

171. Leslie-Pelecky, D. L.; Rieke, R. D., Magnetic properties of nanostructured materials. *Chemistry of Materials* **1996**, 8 (8), 1770-1783.

172. Li, Q.; Kartikowati, C. W.; Horie, S.; Ogi, T.; Iwaki, T.; Okuyama, K., Correlation between particle size/domain structure and magnetic properties of highly crystalline Fe₃O₄ nanoparticles. *Scientific Reports* **2017**, 7 (1), 9894.

173. Jeun, M.; Lee, S.; Kyeong Kang, J.; Tomitaka, A.; Wook Kang, K.; Il Kim, Y.; Takemura, Y.; Chung, K.-W.; Kwak, J.; Bae, S., Physical limits of pure superparamagnetic Fe₃O₄ nanoparticles for a local hyperthermia agent in nanomedicine. *Applied Physics Letters* **2012**, 100 (9), 092406.

174. Kim, D.; Lee, N.; Park, M.; Kim, B. H.; An, K.; Hyeon, T., Synthesis of uniform ferrimagnetic magnetite nanocubes. *Journal of the American Chemical Society* **2008**, 131 (2), 454-455.

175. Shokouhimehr, M.; Soehnlén, E. S.; Hao, J.; Griswold, M.; Flask, C.; Fan, X.; Basilion, J. P.; Basu, S.; Huang, S. D., Dual purpose Prussian blue nanoparticles for cellular imaging and drug delivery: a new generation of T₁-weighted MRI contrast and small molecule delivery agents. *Journal of Materials Chemistry* **2010**, 20 (25), 5251-5259.

176. Koenig, S. H.; Brown III, R. D., Field-cycling relaxometry of protein solutions and tissue: implications for MRI. *Progress in Nuclear Magnetic Resonance Spectroscopy* **1990**, 22 (6), 487-567.

177. Kowalewski, J.; Nordenskiöld, L.; Benetis, N.; Westlund, P.-O., Theory of nuclear spin relaxation in paramagnetic systems in solution. *Progress in Nuclear Magnetic Resonance Spectroscopy* **1985**, 17, 141-185.

178. Lauffer, R. B., Paramagnetic metal complexes as water proton relaxation agents for NMR imaging: theory and design. *Chemical Reviews* **1987**, 87 (5), 901-927.

179. Gonzalez, G.; Powell, D. H.; Tissieres, V.; Merbach, A. E., Water-exchange, electronic relaxation, and rotational dynamics of the MRI contrast agent [Gd (DTPA-BMA)(H₂O)] in aqueous solution: a variable pressure, temperature, and magnetic field oxygen-17 NMR study. *The Journal of Physical Chemistry* **1994**, 98 (1), 53-59.

180. Rohrer, M.; Bauer, H.; Mintorovitch, J.; Requardt, M.; Weinmann, H.-J., Comparison of magnetic properties of MRI contrast media solutions at different magnetic field strengths. *Investigative Radiology* **2005**, 40 (11), 715-724.

181. León-Rodríguez, D.; Luis, M.; Martins, A. F.; Pinho, M. C.; Rofsky, N. M.; Sherry, A. D., Basic MR relaxation mechanisms and contrast agent design. *Journal of Magnetic Resonance Imaging* **2015**, *42* (3), 545-565.
182. Simon, G. H.; Bauer, J.; Saborovski, O.; Fu, Y.; Corot, C.; Wendland, M. F.; Daldrup-Link, H. E., T1 and T2 relaxivity of intracellular and extracellular USPIO at 1.5 T and 3T clinical MR scanning. *European Radiology* **2006**, *16* (3), 738-745.
183. Jung, C. W.; Jacobs, P., Physical and chemical properties of superparamagnetic iron oxide MR contrast agents: ferumoxides, ferumoxtran, ferumoxsil. *Magnetic Resonance Imaging* **1995**, *13* (5), 661-674.
184. American National Standards Institute. United States of America Standards, I., American national standard for the safe use of lasers. 2014; Vol. ANSI Z136.1 – 2014.
185. Fu, G.; Liu, W.; Feng, S.; Yue, X., Prussian blue nanoparticles operate as a new generation of photothermal ablation agents for cancer therapy. *Chemical Communications* **2012**, *48* (94), 11567-11569.
186. Meagher, M. J.; Leone, B.; Turnbull, T. L.; Ross, R. D.; Zhang, Z.; Roeder, R. K., Dextran-encapsulated barium sulfate nanoparticles prepared for aqueous dispersion as an X-ray contrast agent. *Journal of Nanoparticle Research* **2013**, *15* (12), 2146.
187. Goya, G. F.; Asín, L.; Ibarra, M. R., Cell death induced by AC magnetic fields and magnetic nanoparticles: current state and perspectives. *International Journal of Hyperthermia* **2013**, *29* (8), 810-818.
188. Martinez-Boubeta, C.; Simeonidis, K.; Makridis, A.; Angelakeris, M.; Iglesias, O.; Guardia, P.; Cabot, A.; Yedra, L.; Estradé, S.; Peiró, F., Learning from nature to improve the heat generation of iron-oxide nanoparticles for magnetic hyperthermia applications. *Scientific Reports* **2013**, *3*, 1652.
189. Espinosa, A.; Di Corato, R.; Kolosnjaj-Tabi, J.; Flaud, P.; Pellegrino, T.; Wilhelm, C., Duality of iron oxide nanoparticles in cancer therapy: amplification of heating efficiency by magnetic hyperthermia and photothermal bimodal treatment. *ACS Nano* **2016**, *10* (2), 2436-2446.
190. Kravzov, J.; Rios, C.; Altagracia, M.; Monroy-Noyola, A.; Lopez, F., Relationship between physicochemical properties of Prussian blue and its efficacy as antidote against thallium poisoning. *Journal of Applied Toxicology* **1993**, *13* (3), 213-216.
191. Faustino, P. J.; Yang, Y.; Progar, J. J.; Brownell, C. R.; Sadrieh, N.; May, J. C.; Leutzinger, E.; Place, D. A.; Duffy, E. P.; Houn, F., Quantitative determination of cesium binding to ferric hexacyanoferrate: Prussian blue. *Journal of Pharmaceutical and Biomedical Analysis* **2008**, *47* (1), 114-125.
192. Guardia, P.; Di Corato, R.; Lartigue, L.; Wilhelm, C.; Espinosa, A.; Garcia-Hernandez, M.; Gazeau, F.; Manna, L.; Pellegrino, T., Water-soluble iron oxide nanocubes

with high values of specific absorption rate for cancer cell hyperthermia treatment. *ACS Nano* **2012**, 6 (4), 3080-3091.

193. Fortin, J.-P.; Wilhelm, C.; Servais, J.; Ménager, C.; Bacri, J.-C.; Gazeau, F., Size-sorted anionic iron oxide nanomagnets as colloidal mediators for magnetic hyperthermia. *Journal of the American Chemical Society* **2007**, 129 (9), 2628-2635.

194. Usov, N.; Grebenshchikov, Y. B., Influence of surface anisotropy on magnetization distribution in a single-domain particle. *Journal of Applied Physics* **2008**, 104 (4), 043903.

195. Schäffer, A. F.; Sukhov, A.; Berakdar, J., Size-dependent frequency bands in the ferromagnetic resonance of a Fe-nanocube. *Journal of Magnetism and Magnetic Materials* **2017**, 438, 70-75.

196. FDA, Guidance for Industry and FDA Staff: Current Good Manufacturing Practice Requirements for Combination Products. U.S. Food and Drug Administration: Silver Spring, MD, 2015.

197. Hay, M.; Thomas, D. W.; Craighead, J. L.; Economides, C.; Rosenthal, J., Clinical development success rates for investigational drugs. *Nature Biotechnology* **2014**, 32 (1), 40.

198. Thomas, D. W.; Burns, J.; Audette, J.; Carroll, A.; Dow-Hygelund, C.; Hay, M., Clinical development success rates 2006–2015. *San Diego: Biomedtracker/Washington, DC: BIO/Bend: Amplion* **2016**.

199. Gautam, M.; Poudel, K.; Yong, C. S.; Kim, J. O., Prussian blue nanoparticles: Synthesis, surface modification, and application in cancer treatment. *International Journal of Pharmaceutics* **2018**, 549 (1-2), 31-49.

200. Society, A. C. Breast Cancer Treatment. <https://www.cancer.org/cancer/breast-cancer/treatment.html> (accessed 09/01/2018).

201. Group, E. B. C. T. C., Effects of radiotherapy and of differences in the extent of surgery for early breast cancer on local recurrence and 15-year survival: an overview of the randomised trials. *The Lancet* **2005**, 366 (9503), 2087-2106.

202. Giuliano, A. E.; Hunt, K. K.; Ballman, K. V.; Beitsch, P. D.; Whitworth, P. W.; Blumencranz, P. W.; Leitch, A. M.; Saha, S.; McCall, L. M.; Morrow, M., Axillary dissection vs no axillary dissection in women with invasive breast cancer and sentinel node metastasis: a randomized clinical trial. *JAMA* **2011**, 305 (6), 569-575.

203. Institute, N. C. Breast Cancer Treatment (PDQ®)–Patient Version. <https://www.cancer.gov/types/breast/patient/breast-treatment-pdq> (accessed 09/01/2018).

204. Wolff, A. C.; Blackford, A. L.; Visvanathan, K.; Rugo, H. S.; Moy, B.; Goldstein, L. J.; Stockerl-Goldstein, K.; Neumayer, L.; Langbaum, T. S.; Theriault, R. L., Risk of

marrow neoplasms after adjuvant breast cancer therapy: the national comprehensive cancer network experience. *Journal of Clinical Oncology* **2014**, 33 (4), 340-348.

205. Azim Jr, H.; De Azambuja, E.; Colozza, M.; Bines, J.; Piccart, M., Long-term toxic effects of adjuvant chemotherapy in breast cancer. *Annals of Oncology* **2011**, 22 (9), 1939-1947.

206. Society, A. C. Hormone Therapy for Breast Cancer. <https://www.cancer.org/cancer/breast-cancer/treatment/hormone-therapy-for-breast-cancer.html> (accessed 09/01/2018).

207. De Azambuja, E.; Procter, M. J.; Van Veldhuisen, D. J.; Agbor-Tarh, D.; Metzger-Filho, O.; Steinseifer, J.; Untch, M.; Smith, I. E.; Gianni, L.; Baselga, J., Trastuzumab-associated cardiac events at 8 years of median follow-up in the Herceptin Adjuvant trial (BIG 1-01). *Journal of Clinical Oncology* **2014**, 32 (20), 2159-2165.

208. Shah, J.; Aglyamov, S. R.; Sokolov, K.; Milner, T. E.; Emelianov, S. Y., Ultrasound imaging to monitor photothermal therapy—Feasibility study. *Optics Express* **2008**, 16 (6), 3776-3785.

209. Kim, S.; Chen, Y.-s.; Luke, G.; Emelianov, S., In-vivo ultrasound and photoacoustic image-guided photothermal cancer therapy using silica-coated gold nanorods. *IEEE Transactions on Ultrasonics, Ferroelectrics, and Frequency Control* **2014**, 61 (5), 891-897.